A predictive numerical model of the Atmospheric Boundary Layer based on the Turbulent Energy Equation.

En numerisk prognosmodell för det Atmosfäriska Gränsskiktet grundad på den Turbulenta Energiekvationen.

by Svante Bodin

Nr RMK 13 (1979)

SMHI

Sveriges meteorologiska och hydrologiska institut

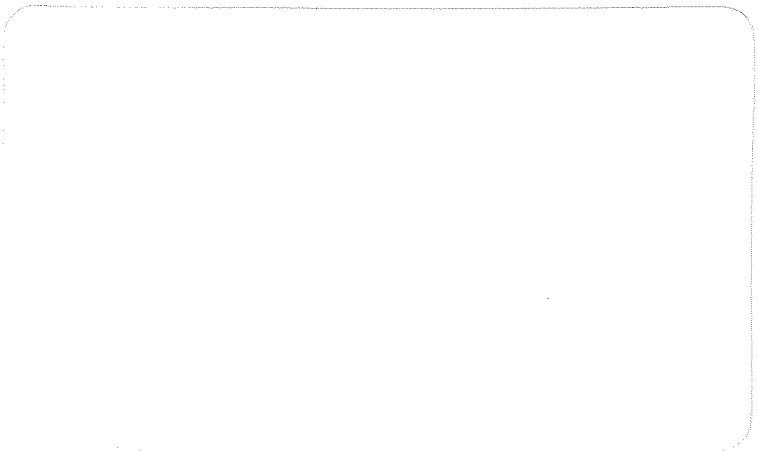

Corrections

page 10, line 9 and 10 should read:

..... shown to occur in the convective boundary layer .....

page 25, eq. (42) should read:

$$K_m = a_4 \cdot b^{1/2} \cdot \ell \qquad (42)$$

page 33, line 2 should be:

by simply .....

page 61, line 16 and following should read:

The basic results are shown in figs. 13, 14 and 17, showing predicted potential temperature profiles during the day, two nocturnal temperature profiles and a time-height cross-section of the u-component of the wind.

page 92, After fifth line from the bottom of page insert:

We assume that the hydrostatic state is moist-adiabatically stratified - in analogy with the dry case - and that it can be approximated by I.1.

page 108, reference 9 should be:

Pandolfo et al .....

page 117, fig. 15:

The label of the x-axis should be ^{o}C.

A predictive numerical model of the Atmospheric Boundary Layer based on the Turbulent Energy Equation.

En numerisk prognosmodell för det Atmosfäriska Gränsskiktet grundad på den Turbulenta Energiekvationen.

by Svante Bodin

Nr RMK 13 (1979)

SMHI Rapporter
METEOROLOGI och KLIMATOLOGI
Nr RMK 13 (1979)
ISSN 0347-2116

SMHI, RMK 13 (1979)

Abstract

The interest in numerical modeling of the atmospheric boundary layer has grown considerably over the last decade. At SMHI and elsewhere boundary layer models find applications in local forecasting, especially at airports, in air pollution diffusion and dispersion studies and in wind energy programmes.

In this report an one-dimensional numerical boundary layer model is derived and numerical simulations of boundary layer data from Australia and Finland are presented and discussed. The model, which is the first step towards a three-dimensional model, is based on the so-called Gutman approach and incorporates the turbulent energy equation for turbulence closure. A scale analysis is performed, that shows that unless a grid distance of 20 km or less can be used in a three-dimensional model it is more profitable to use an one-dimensional one with more sophisticated physical parameterizations.

The model also includes condensation, i e fog and clouds, and complete radiation computations. A predictive equation for surface temperature is used in conjunction with a simple soil moisture model.

The numerical solution employs a variety of the Crank-Nicolson scheme called Laasonen's scheme. The vertical coordinate is transformed log-linearly into a new height coordinate to allow better resolution close to the ground. 35 grid points are used to describe the boundary layer up to 2000 m. A time step of 4 minutes has been used in the simulations.

Two versions of the model, the Gutman version and a usual "Ekman" version, have been tested on day 33 and 34 of the Wangara data. The two versions have been compared and the Ekman version has also been compared with the simulations of Yamada & Mellor (1975).

The results show that the Ekman version is superior when simulating the wind of the Wangara data. The thermal boundary layer development is very well predicted by both versions. Comparisons with Yamada & Mellor speak in favour of the present model.

Conclusions are drawn and some future work is outlined. The model is intended to undergo operational tests at Arlanda airport in the near future.

Sammanfattning

Intresset för gränsskiktsmodeller har vuxit markant under senare år. Vid SMHI planeras tillämpningar av gränsskiktsmodeller inom lokalprognosområdet, speciellt vid flygplatser, i studier av luftföroreningars spridning och inom vindenergiprogrammet.

I denna rapport presenteras en en-dimensionell numerisk gränsskiktsmodell och resultat från simuleringar av australienska och finländska gränsskiktsdata diskuteras relativt ingående. Modellen, som utgör första steget mot en tre-dimensionell modell, bygger på idéer om gränsskiktsmodellering framlagda av Gutman. För att parameterisera turbulensen i gränsskiktet utnyttjas den turbulenta energiekvationen. En enkel skalanalys av rörelseekvationerna visar att ett gridavstånd på mindre än 20 km måste användas i en tre-dimensionell modell för att man ska uppnå fördelar gentemot en en-dimensionell modell, i vilken fullständigare fysikaliska beskrivningar kan inkluderas.

Modellen i denna rapport innehåller också kondensationsprocesser, d v s dimma och moln, och ett komplett paket för strålningsberäkningar. En prognosekvation för marktemperaturen finns härledd och används i samband med en enkel modell för markvatten.

I den numeriska lösningen utnyttjas Laasonens metod, en variant av Crank-Nicolson, för tidsintegrationen. Den vertikala koordinaten har transformerats log-lineärt för att ge bättre upplösning nära marken. 35 gridpunkter används för att upplösa gränsskiktet upp till 2000 m. Ett tidssteg om 4 minuter har använts i de flesta simuleringarna.

Två versioner av modellen, en Gutman-version och en vanlig "Ekman"-version, har testats utifrån dag 33 och 34 av Wangara data. De två första versionerna har jämförts sinsemellan medan Ekman-versionen också har jämförts med Yamada & Mellors (1975) mycket omfattande simuleringar. Resultaten visar att när det gäller vinden är Ekmanversionen överlägsen Gutman-versionen. Temperaturen å andra sidan simuleras mycket bra av båda versionerna. Jämförelsen med Yamada & Mellor utfaller till fördel för den här beskrivna modellen.

Vissa framtida förbättringar diskuteras avslutningsvis. Modellen planeras också att testas operationellt på Arlanda flygplats inom en nära framtid.

TABLE OF CONTENT

TABLE OF CONTENT, continuation

TABLE OF CONTENT, continuation

Nomenclature

ABL	Atmospheric Boundary Layer
α_T	K_h/K_m
α_i	coefficient in linear system of equations
b	turbulent energy
β	4.7 or 2-3 (in soilwater relations)
β_i	as for α_i
c	cloud cover
c_p	specific heat of dry air
c^*	average specific heat of air and soil layer
c_s	specific heat of the soil
c_q	coefficient in thermodynamic equation
D	depth of model soil layer
D_z, $D\ell_i$	$\frac{\partial \xi}{\partial z}$, vertical grid transformation
Δt	time step
Δz	vertical grid distance
δ	solar declination
δ_i	as for α_i
E	evaporation or emissivity
E_p	potential evaporation
E_b E_{bo}	Ekman numbers
e_s	saturation vapor pressure
ε_s	surface emissivity
ε	turbulent energy dissipation or 0.622 in definition of q
f	Coriolis parameter
F	heat flux in general
F_s	soil heat flux or flux of solar radiation
F_a	sum of atmospheric heat fluxes
F_{ts}	turbulent flux of sensible heat
F_ℓ	flux of latent heat
f(w)	Halstead parameter
FC	field capacity
g	gravitational constant
Γ_d	dry adiabatic lapse rate
γ_{cg}	counter gradient heat flux term
γ_i	as for α_i

H	top of ABL-model
h	boundary layer or mixed layer height
h_s	moist static energy
K_m	turbulent exchange coefficient for momentum
K_h	" " " " heat
K_s	thermal diffusivity in the soil
κ	" conductivity in the soil
K_b	scaling turbulent exchange coefficients
K_o	
L	Monin-Obukhov length
L_o	surface Monin-Obukhov length
ℓ	mixing length
ℓ_ε	dissipation length scale
ℓ_N	neutral mixing length
λ	limit of ℓ_N
μ	Crank-Nicolson weight
N	number of grid points
P	precipitation
p	air pressure
p_o	reference pressure = 1000 mb
R	gas constant for dry air
Ro	Rossby number
Ri	Richardson number
Ri_c	critical Richardson number
R_{net}	net radiation at the surface
ρ	density of air
ρ_s	" " soil
q	specific humidity
q_s	saturation specific humidity
q_ℓ	liquid water mixing ratio
Q_q	source term in moisture equation
S	wind shear
ξ	transformed vertical coordinate
σ	Stefan-Boltzman's constant
u	x-component of the wind vector or optical depth
u_g	x-component of the geostrophic wind vector
u_*	friction velocity

v	y-component of wind vector
v_g	" " geostrophic wind vector
$\mathbb{V}$	wind vector
$\mathbb{V}_g$	geostrophic wind vector
w	vertical velocity
w_*	vertical scaling velocity
T	temperature or transmission
T_o	surface temperature = T_{surf}
T_s	soil temperature
t	time
τ	time step number
Θ	potential temperature
x	spatial coordinates
y	
z	
z_o	roughness length
ζ	$= z/L$

1. Introduction

Numerical weather prediction has so far dealt very little with the prediction of local weather. The prediction models have been directed towards forecasting the large scale atmospheric flow - the Rossby waves and the frontal cyclones of the westerlies. The atmospheric boundary layer (ABL) has mainly been of interest to numerical modelers in so far it is affecting the evolution of the large scale flow. For short range prediction models very crude parameterizations based on Ekman theory have been used to incorporate the effect of surface friction. It is obvious, however, that most of the weather processes affecting man and the society are occuring in the ABL but the interpretation of the large scale numerical forecast has by and large been left to the human weather forecaster. In some areas statistical methods have started to come into use, in varying degrees of success. The stronger emphasis on the local forecast problem and the development of our understanding of the physical and dynamical processes in the ABL in recent years have facilitated the development of numerical models of the ABL. At SMHI we have been working for some years with the development of an one-dimensional boundary layer model suitable for local forecasting of meteorological elements like temperature, wind, humidity, turbulence, fog and low clouds and wind shear. The aim has been to supply better guidance for issuing terminal area forecasts (TAF) at, primarily, the international airports at Stockholm, Göteborg, Malmö and Sundsvall.

The need for numerical models is also great in a number of other problem areas like the diffusion and dispersion of air pollution, wind energy studies and urban meteorology. The model developed by the author is formulated in a general way allowing applications in other areas than local forecasting with minor modifications of the code.

The basic problem in boundary layer modeling is the parameterization of the turbulent exchange processes in the ABL but for local forecasting the model must also be able to describe condensation, radiation, long wave and short wave, energy and moisture exchange with the underlying surface and non-stationary aspects of the evolution of the ABL.

In recent years there has been a considerable progress in the physical and numerical modeling of the ABL. Part of this progress is connected with the so-called "higher order modeling", by means of which it has been possible to study in detail the growth and development of unstable, convective, boundary layers. Deardorff (1974a, b) has used a three-dimensional model to generate a multitude of data on the ABL under unstable conditions. Similar, but simplified, numerical simulations of the unstable and stable boundary layer by Wyngaard & Cote (1974), Wyngaard (1975), Mellor & Yamada (1974), Shir (1973) and others based on "second order models" have indicated ways of treating turbulence in simplified ways still capable of realistically simulating most of the important properties of the ABL. One such simplified approach is the use of the Turbulent Energy (TE) equation. This type of closure for turbulence has been used by Bradshaw (1967), Delage (1974), Yu (1976), Lykosov & Gutman (1974), Speranskiye et al (1975) and Clarke (1974). The development and the state of the art in the field of numerical boundary layer modeling has been extensively reviewed by the author in Bodin (1978). In this paper are discussed most of the problems, physical, dynamical and numerical, arising in numerical modeling of the ABL.

In the present model the TE-equation has been used for turbulence closure. It will be shown that by choosing a proper mixing length formulation it is possible to remedy some of the short-comings of simple K-theory, without going into the very extensive calculations required in "higher order models", with very little extra computer time requirements.

Another important feature is the attempt to use an approach to meso-scale problems outlined by Gutman (1969). Since the aim of the present work is to couple the ABL-model to a large-scale, numerical prediction model the Gutman approach is potentially well suited. The equations for the boundary layer do not carry the geostrophic wind which simplifies the upper boundary conditions. Furthermore it can be shown that this approach also filters out a certain class of diffusive-inertial oscillations present in an ABL-model with time-varying geostrophic wind, as discussed in Bodin (1974). In that report are also discussed other effects of non-stationarity in the boundary layer.

A short description of the present model and some preliminary results have been presented in Bodin (1976). The work with the model has now reached a stage, however, when a more comprehensive documentation of the model has become desirable.

2. Derivation of the model equations

2.1 The momentum equations

As the starting point we will take the equations of motion for the mean flow in the Boussinesque approximation (Lumley & Panofsky (1964))

$$\frac{\partial \bar{u}}{\partial t} + \bar{v}\cdot\nabla\bar{u} - f\bar{v} = -\frac{1}{\bar{\rho}}\frac{\partial \bar{p}}{\partial x} - \frac{\partial}{\partial x}\left(\overline{u'^2}\right) - \frac{\partial}{\partial y}\left(\overline{u'v'}\right) - \frac{\partial}{\partial z}\left(\overline{u'w'}\right) \qquad (1)$$

$$\frac{\partial \bar{v}}{\partial t} + \bar{v}\cdot\nabla\bar{v} + f\bar{u} = -\frac{1}{\bar{\rho}}\frac{\partial \bar{p}}{\partial x} - \frac{\partial}{\partial x}\left(\overline{u'v'}\right) - \frac{\partial}{\partial y}\left(\overline{v'^2}\right) - \frac{\partial}{\partial z}\left(\overline{v'w'}\right)$$

where we have neglected molecular diffusion.

The components of the wind, u the westerly, v the southerly component and w the vertical component are divided into two parts

$$\begin{aligned} u &= \bar{u} + u' \\ v &= \bar{v} + v' \\ w &= \bar{w} + w' \end{aligned} \qquad (2)$$

where primes denote turbulent fluctuations and bars time averages.

We have furthermore assumed that the mean state is in hydrostatic equilibrium.

We will further assume that the divergence of the vertical momentum flux is much greater than the horizontal divergence, i e

$$\frac{\partial}{\partial z}\left(\overline{u'w'}\right) \sim \frac{\partial}{\partial z}\left(\overline{v'w'}\right) >> \frac{\partial}{\partial x}\left(\overline{u'^2}\right),$$

$$\frac{\partial}{\partial y}\left(\overline{u'v'}\right), \frac{\partial}{\partial x}\left(\overline{u'v'}\right), \frac{\partial}{\partial y}\left(\overline{v'^2}\right)$$

We will also <u>formally</u> introduce a turbulent diffusion coefficient through

$$-\overline{u'w'} = K_m \frac{\partial \bar{u}}{\partial z} \qquad -\overline{v'w'} = K_m \frac{\partial \bar{v}}{\partial z} \qquad (3)$$

The basic equations of motion then read

$$\begin{aligned} \frac{\partial \bar{u}}{\partial t} + \bar{\mathbf{v}}\cdot\nabla\bar{u} - f\bar{v} &= -\frac{1}{\bar{\rho}}\frac{\partial \bar{p}}{\partial x} + \frac{\partial}{\partial z}\left(K_m \frac{\partial \bar{u}}{\partial z}\right) \\ \frac{\partial \bar{v}}{\partial t} + \bar{\mathbf{v}}\cdot\nabla\bar{v} + f\bar{u} &= -\frac{1}{\bar{\rho}}\frac{\partial \bar{p}}{\partial x} + \frac{\partial}{\partial z}\left(K_m \frac{\partial \bar{v}}{\partial z}\right) \end{aligned} \qquad (4)$$

2.2 The thermodynamic equation

Condensation affects the thermodynamic structure of the boundary layer. There is not any obvious simple way of treating the phase changes of water and the consequent heating or cooling due to release of latent heat or evaporation. However, in studies of shallow convection different linearizations of the moist adiabatic process have been used as approximations. Betts (1973) suggested the use of a liquid-water potential temperature later employed by Deardorff (1976) when modeling stratocumulus clouds at the top of the ABL. Betts (1974) also discussed the conservation of static energy as an approximation to moist-adiabatic processes as suggested by Madden & Robitaille (1970). In the present model the thermodynamic equation and the turbulent energy equation are derived by using the conservation of static energy in turbulent mixing. A conservation of saturation static energy implies that kinetic energy is dissipated locally where it is generated, which for most turbulent regimes, in which condensation occurs, can be regarded as a good approximation.

The moist static energy is defined as

$$h_s = c_p T + L q_s + gz \qquad (5)$$

where c_p is specific heat capacity of (dry) air, q_s is saturation specific humidity, and gz the geopotential. L is the latent heat of condensation.

In eq (5) temperature and not virtual temperature has been used since the model is going to be used at northern latitudes where the moisture contribution to buoyancy during most of the year is negligible.

A volume of air might still be heated or cooled by radiative heat flux divergence.

We will then write the conservation equation as

$$\frac{dh_s}{dt} + \frac{\partial F}{\partial z} = 0 \qquad (6)$$

where F is the total, short wave and long wave, radiative heat flux.

We now introduce a mean static energy and a turbulent fluctuation from the mean

$$h_s = \bar{h}_s + h_s' \qquad (7)$$

Expanding the total derivative and introducing (7) and (2) and assuming the flow to be incompressible, (which is justified when the velocities are much less than the speed of sound).

$$\frac{\partial w'}{\partial z} + \frac{\partial u'}{\partial x} + \frac{\partial v'}{\partial y} = 0 \qquad (8)$$

we get, after averaging, the following equation ($\overline{h_s'} = 0$)

$$\frac{d\bar{h}_s}{dt} + \nabla_h(\overline{v_h' h_s'}) + \frac{\partial}{\partial z}(\overline{w' h_s'}) = -\frac{\partial \bar{F}}{\partial z} \qquad (9)$$

where h refers to horizontal components.

In accordance with the assumption for eqs (4) we neglect the divergence of the horizontal fluxes $\overline{v_H h_s'}$. Furthermore we make use of a flux-gradient assumption

$$\overline{w' h_s'} = -K_h \frac{\partial \bar{h}_s}{\partial z} \qquad (10)$$

By using the definition of h_s we get

$$c_p \frac{d\bar{T}}{dt} + L \frac{d\overline{q_s}}{dt} + g \frac{d\bar{z}}{dt} = \frac{\partial}{\partial z}\left(K_h\left(c_p \frac{\partial T}{\partial z} + L \frac{\partial \overline{q_s}}{\partial z} + g\right)\right) - \frac{\partial \bar{F}}{\partial z}$$

Dividing by c_p and noting that $\Gamma_d = g/c_p$ is the dry-adiabatic lapse rate we get the thermodynamic equation in the form it is going to be used in the model.

$$\frac{\partial \bar{T}}{\partial t} + \bar{V}_H \nabla_H \bar{T} + \bar{w}\left(\frac{\partial \bar{T}}{\partial z} + \Gamma_d\right) + \frac{L}{c_p}\frac{d\bar{q}_s}{dt}$$

$$= \frac{\partial}{\partial z}\left(K_h\left(\frac{\partial \bar{T}}{\partial z} + \frac{L}{c_p}\frac{\partial \bar{q}_s}{\partial z} + \Gamma_d - \gamma_{cg}\right)\right)$$

$$- \frac{1}{c_p}\frac{\partial \bar{F}}{\partial z} \qquad (11)$$

In equation (11) we have also inserted a correction term, γ_{cg} , making it possible to allow for a "counter gradient" heat flux which has been shown to occur at very unstable stratification - the so-called Priestly-Swinbank effect. The extra, γ_{cg} , term will be discussed in section 3.3. The γ_{cg} is zero, however, in neutral and stable conditions. In eq (11) the terms

$$\frac{L}{c_p} \cdot \frac{d\bar{q}_s}{dt} \text{ and } \frac{L}{c_p}\frac{\partial \bar{q}_s}{\partial z} \text{ are included only when}$$

$q > q_s(\bar{T})$, where q is total water content, gaseous and liquid water. In unsaturated conditions potential temperature is conserved in turbulent mixing, which is equivalent with eq (11) when the mentioned terms and radiation are dropped.

2.3 Moisture conservation equation

To predict the content of water in the air we introduce the total specific water content, gaseous and liquid, q

$$q = q_s + q_\ell \text{ kg/kg} \qquad (12)$$

where $q_s = q_s(T,p)$ is saturation specific humidity. This means that $q_\ell < 0$ when air is unsaturated, showing the saturation deficit, and $q_\ell > 0$ when saturated conditions occur. It is assumed that q is conserved except for sources and sinks in the ABL.

The moisture equation will be used in the form

$$\frac{d\bar{q}}{dt} = \frac{\partial}{\partial z}\left(K_h \frac{\partial \bar{q}}{\partial z}\right) + \bar{Q}_q \qquad (13)$$

which is derived in a similar way as eq (11).

$\bar{Q}_q$ is a source term which makes it possible to make provisions for chiefly two effects:

Evaporation from raindrops falling through the ABL;
Drizzle or settlement of fog droplets.

Eq (13) implies that water vapor and liquid water are diffused in the same way with the same K_h as in eq (10).

2.4 The splitting up of the equations and Gutman's approach

In Gutman (1969) and in Gutman & Perov (1970) is discussed a way of treating the equations of motion suitable for meso-scale and boundary layer problems. The main idea is to split up the equations into two parts - one describing the large scale synoptic flow, e g a set of primitive equations, the other describing the particular flow problem under consideration. This technique is in fact not different from the one generally employed when solving partial differential equations where it is common to split up the solution into different parts satisfying different boundary conditions. Since this part of the model has been subject to misunderstandings in the past we will include a fairly complete discussion of the derivation of the equations used in the model. To illuminate some points concerning one-dimensional and three-dimensional models a simple scale-analysis will also be carried out.

The equations for the total flow will be the ones defined by eqs (4), (11) and (13).

In addition we must have the continuity equation

$$\frac{d\bar{\rho}}{dt} + \bar{\rho}\nabla\cdot\bar{\mathbf{v}} = 0 \qquad (14)$$

the hydrostatic equation

$$\frac{\partial\bar{p}}{\partial z} = -g\bar{\rho} \qquad (15)$$

and the equation of state

$$\bar{p} = \bar{\rho}R\bar{T} \qquad (16)$$

all valid for the mean, total, flow. Since we already have introduced the assumption for the non-resolved turbulent motion by means of eqs (3) and (10) we will now drop the bars for denoting the mean motion.

Instead we will introduce this notation when splitting up the variables according to Gutman. To avoid future confusion we contend that here after

* a bar over <u>one</u> variable means "background" flow in the sense defined below

* a prime over <u>one</u> variable refers to boundary layer flow i e the mean boundary layer flow

* a bar over a product of <u>two</u> primed quantities will still have the meaning of a second moment, e q $\overline{w'\Theta'}$ etc.

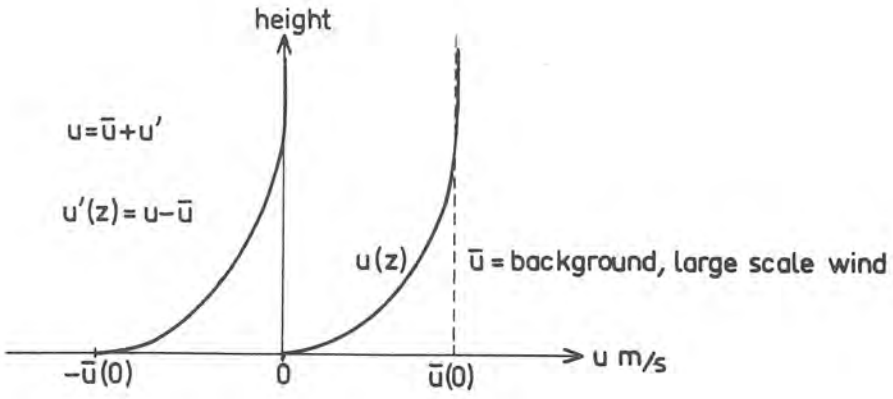

Fig 1
An example of the definition of $\bar{u}$ and u' for the case when the "background" wind is constant in the ABL. We can regard $\bar{u}$ as given from a numerical model with boundary conditions w(0) = 0.

We now split up the variables, noting the orders of magnitude of primed and barred quantities

$$
\begin{aligned}
u &= \bar{u} + u' & u' &\sim \bar{u} \\
v &= \bar{v} + v' & v' &\sim \bar{v} \\
T &= \bar{T} + T' & T' &\ll \bar{T} \\
\theta &= \bar{\theta} + \theta' & \theta' &\ll \bar{\theta} \\
q &= \bar{q} + q' & q' &\sim \bar{q} \\
p &= \bar{p} + p' & p' &\ll \bar{p} \\
\rho &= \bar{\rho} + \rho' & \rho' &\ll \bar{\rho} \\
w &= \bar{w} + w' & w' &\sim \bar{w} \\
K_i &= \bar{K}_i + K_i' & K_i' &> \bar{K}_i \qquad i = m,h
\end{aligned}
\tag{17}
$$

The next step is to define a set of equations for the large scale, background, flow, which can be taken as the equations for a primitive equation model. We then formally define

$$\frac{\partial \bar{u}}{\partial t} + \bar{\mathbf{v}}\cdot\nabla\bar{u} - f(\bar{v} - \bar{v}_g) = \frac{\partial}{\partial z}\left(\bar{K}_m \frac{\partial \bar{u}}{\partial z}\right) \qquad (18)$$

$$\frac{\partial \bar{v}}{\partial t} + \bar{\mathbf{v}}\cdot\nabla\bar{v} + f(\bar{u} - \bar{u}_g) = \frac{\partial}{\partial z}\left(\bar{K}_m \frac{\partial \bar{v}}{\partial z}\right) \qquad (19)$$

$$\frac{\partial \bar{T}}{\partial t} + \bar{\mathbf{v}}_H\cdot\nabla_H\bar{T} + \bar{w}\left(\frac{\partial \bar{T}}{\partial z} + \Gamma_d\right) =$$

$$= \frac{\partial}{\partial z}\left(\bar{K}_h\left(\frac{\partial \bar{T}}{\partial z} + \Gamma_d - \gamma_{cg}\right)\right) -$$

$$- \frac{1}{c_p}\cdot\frac{\partial \bar{F}}{\partial z} \qquad (20)$$

$$\frac{d\bar{q}}{dt} = \frac{\partial}{\partial z}\left(\bar{K}_h \frac{\partial \bar{q}}{\partial z}\right) + \bar{Q}_q \qquad (21)$$

$$0 = -\frac{1}{\bar{\rho}}\frac{\partial \bar{p}}{\partial z} - g \qquad (22)$$

$$\frac{d\bar{\rho}}{dt} + \bar{\rho}\,\mathrm{Div}\,\bar{\mathbf{v}} = 0 \qquad (23)$$

In eq (20) it is assumed that there is no condensation in the boundary layer in the large scale model.

$$\bar{p} = R\,\bar{T}\,\bar{\rho} \qquad (24)$$

and

$$\frac{d}{dt} = \bar{u}\frac{\partial}{\partial x} + \bar{v}\frac{\partial}{\partial y} + \bar{w}\frac{\partial}{\partial z} \qquad (23)$$

and $\bar{u}_g$ and $\bar{v}_g$ are large scale geostrophic winds.

We now insert the relations (17) into the eqs (4), (11), (13), (14), (15) and (16) and then subtract eqs (18)-(23) after expansion.

The result will then formally be

$$\frac{\partial u'}{\partial t} + (\bar{u}+u')\frac{\partial u'}{\partial x} + u'\frac{\partial \bar{u}}{\partial x} + (\bar{v}+v')\frac{\partial u'}{\partial y} +$$

$$+ v'\frac{\partial \bar{u}}{\partial y} + (\bar{w}+w')\frac{\partial u'}{\partial z} + w'\frac{\partial \bar{u}}{\partial z} - fv' =$$

$$= -\frac{1}{\bar{\rho}}\frac{\partial p'}{\partial x} + \frac{\partial}{\partial z}\left(K'_m\frac{\partial u}{\partial z}\right) + \frac{\partial}{\partial z}\left(\bar{K}_m\frac{\partial u'}{\partial z}\right) \quad (24)$$

· Similar for v'

$$\frac{\partial T'}{\partial t} + (\bar{\mathbb{V}}_H + \mathbb{V}'_H)\nabla_H T' + \mathbb{V}'_H\nabla\bar{T} + (\bar{w}+w')\frac{\partial T'}{\partial z} +$$

$$+ w'\left(\frac{\partial \bar{T}}{\partial z} + \Gamma_d\right) + \frac{L}{c_p}\frac{dq_s}{dt} =$$

$$= \frac{\partial}{\partial z}\left(K'_h\left\{\frac{\partial T}{\partial z} + \Gamma_d + \frac{L}{c_p}\frac{\partial q_s}{\partial z} - \gamma_{cg}\right\} + \right. \quad (25)$$

$$\left. + \bar{K}_h\left\{\frac{\partial T'}{\partial z} + \frac{L}{c_p}\frac{\partial q_s}{\partial z}\right\}\right) - \frac{1}{c_p}\frac{\partial F'}{\partial z}$$

$$\frac{\partial q'}{\partial t} + \mathbb{V}'_H\cdot\nabla_H\bar{q} + (\bar{\mathbb{V}}+\mathbb{V}')\cdot\nabla q' + w'\frac{\partial \bar{q}}{\partial z} + (\bar{w}+w')\frac{\partial q'}{\partial z} =$$

$$= \frac{\partial}{\partial z}\left(K'_h\frac{\partial q}{\partial z} + \bar{K}_h\frac{\partial q'}{\partial z}\right) + Q'_q \quad (26)$$

$$0 = -\frac{\partial p'}{\partial z} - g\rho' \quad (27)$$

$$\frac{\partial \rho'}{\partial t} + \mathbb{V}'\nabla_H\rho + \bar{\mathbb{V}}\nabla_H\rho' + \bar{\rho}\,\mathrm{Div}\,\mathbb{V}' + \bar{\rho}\frac{\partial w'}{\partial z} +$$

$$+ (\bar{w}+w')\frac{\partial \rho'}{\partial z} + w'\frac{\partial \bar{\rho}}{\partial z} = 0 \quad (28)$$

$$(p' \simeq (\bar{\rho}T' + \bar{T}\rho')R)$$

The system of equations (24) through (28) has so far not resulted in any simplifications but is a purely formal result. We are now instead going to study this system from a scale-analysis point of view.

2.5 Scale-analysis of the equations of motion

We are not going to carry out the complete scale analysis but satisfy ourselves with eq (24). The analysis for the other equations can be carried out in a similar way.

Let us start with defining the following scaling variables and the orders of magnitude for the boundary layer variables (subscript b) and large scale variables (subscript o)

Variable x_i	Boundary layer scaling x_{ib}	Large scale flow scaling x_{io}
u,v	$u_b \sim 10$ m/s	$u_o \sim 10$ m/s
w	$w_b \sim 10^{-2}$ m/s	$w_o \sim 10^{-2}$ m/s
x,y	$L_b \sim 10^{\times}$ m	$L_o \sim 10^{6}$ m
Δp	$\Delta p_b \sim 10^{2}$ N/m^2	$\Delta p_o \sim 10^{3}$ N/m^2
ρ	$\rho_b \sim 10^{-3}$ kg/m^3	$\rho_o \sim 1$ kg/m^3

The vertical scale ζ and the exchange coefficient K are very dependent on the stability regime. They have therefore been scaled for the two cases stable and unstable boundary layers

	Stable	Unstable	
ζ_b	10^2	10^3	m
ζ_o	10^4	10^4	m
K_b	1	10^2	m^2/s
K_o	0.1	10	m^2/s

Next we introduce non-dimensional variables $\hat{x}_i$ by means of:

$$\hat{x}_i = \frac{x_i}{x_{ib}} \text{ or } \frac{x_i}{x_{io}}$$

where $\hat{x}_i$ is a non-dimensional variable corresponding to one of the variables in the left column, x_i, scaled by the scaling factor x_{ib} or x_{io} in the two right columns. Introducing the x_i:s into eq (24) and after dropping the hats we get

$$\frac{\partial u'}{\partial t} + Ro_b(\bar{\nabla}+\nabla')\nabla u' + Ro_L \nabla'\nabla\bar{u} + Ro_{bv}(\bar{w}+w')\frac{\partial u'}{\partial z} + Ro_{Lv} w' \frac{\partial \bar{u}}{\partial z} - v' = -\frac{\Delta P_b}{\rho_o L_b f u_o}\frac{1}{\bar{\rho}}\frac{\partial p'}{\partial x} + E_b \frac{\partial}{\partial z}(K'\frac{\partial u}{\partial z}) + E_{bo}\frac{\partial}{\partial z}(\bar{K}\frac{\partial u'}{\partial z}) \quad (29)$$

where the coefficients are defined as

1. $Ro_L = \frac{u_o}{fL_o} \sim 10^{-1}$ — Large scale Rossby number

2. $Ro_b = \frac{u_o}{fL_b} \sim 10^5 \cdot 10^{-x}$ — Boundary layer Rossby number depending on the resolvable horizontal scale $10^x = L_b$

3. $Ro_{bv} = \frac{w_o}{\zeta_b f} \sim 10^0 - 10^{-1}$ — "Vertical" Rossby number in the ABL

4. $Ro_{Lv} = \frac{w_o}{\zeta_o f} \sim 10^{-2}$ — Large scale "vertical" Rossby number

5. $\frac{\Delta p_b}{\rho_o L_b f u_o} \sim 10^5 \cdot 10^{-x}$ — Boundary layer pressure gradient term also depending on L_b

6. $E_b = \frac{K_b}{\zeta_b^2 f} \sim 10^0$ — Ekman number for the ABL

7. $E_{bo} = \frac{K_o}{\zeta_b^2 f} \sim 10^{-1}$ — Turbulent interaction between the large scale flow and the ABL

8. Coriolisterm $\sim 10^0$

The time derivative is scaled by f in eq (29) and in the non-stationary case considered here this term must balance the other terms.

In the table the terms 3, 6 and 7 are estimated in the two stability cases. Terms 6 and 7 have the same value in both cases while 3 varies between 10^{0} in stable conditions to 10^{-1} in unstable conditions.

However, we see that the dominating term is 6, i e the turbulent exchange term (and 8 the Coriolisterm). The terms 1 and 4 are one to two orders of magnitude less than 6 and might be neglected in the first approximation. Term 3 is estimated on the assumption that organized convection is disregarded but can still be of importance. This is especially true in the termodynamic equation and in the moisture equation. Vertical advection is needed to describe the dynamics of an elevated inversion or stable layer above an unstable ABL correctly. The term 7 is of the same magnitude as 1.

For the terms 2 and 5 we have left the question open as to the magnitude of these terms. We can be quite sure that if we go down to let us say scales of the order of a couple of kilometers which is the typical scale of variation of topographical elements like hills and fields, woods, grooves and orchards these terms get similar in magnitude as term 6. If we instead look upon the problem from a modeling point of view the question is: What scale can we actually resolve by a chosen grid-distance? If we assume that we need at least 4 grid points to resolve a given scale of motion we can summarize the scale consideration concerning the terms 2 and 5 in the following table

L_b = 10000 km → $Ro_b \sim 10^{-2}$ ↔ grid-distance ~ 2000 km

L_b = 1000 km → $Ro_b \sim 10^{-1}$ ↔ -"- ~ 200 km

L_b = 100 km → Ro_b $10^{0}=1$ ↔ -"- ~ 20 km

We see that for grid-distances larger than 200 km the terms 2 and 5 are one to two orders of magnitudes less than the diffusion term in the Ekman layer (in the surface layer it is of course completely dominating). From this we might draw the conclusion, that there is really no idea to use a 3-dimensional numerical ABL-model unless one can afford a grid-distance of the order of 20 km. As has been pointed out by Barr & Kreitzberg (1975), each grid point in a 3-dimensional model with horizontal grid distance greater than or equal to 100 km will essentially behave as an isolated one-dimensional model. In this case it is more profitable to invest in a detailed one-dimensional model than in 3-dimensionality with sacrifices in physical fidelity without getting the desired horizontal coupling. In the present model the consequences of these arguments have been followed and an one-dimensional model has been developed awaiting increased computer capacity.

2.6 The one-dimensional model equations

In order to arrive at the one-dimensional model we will make the following assumptions.

1. The ABL is assumed to be approximatively horizontally homogeneous implying fairly flat land with little variation in surface roughness z_o or other surface properties. Of course this restricts the applicability of the model but is a fairly good assumption as long as airports are concerned, with large, flat land areas around the runway system.

2. w' is equal to zero due to assumed hydrostatic equilibrium and following 1.

3. In the thermodynamic and the moisture conservation equation we retain the terms $\bar{w}\frac{\partial T'}{\partial z}$ and $\bar{w}\frac{\partial q'}{\partial z}$ in order to model the behaviour of the ABL at a capping inversion or overlaying stable layer.

4. In the continuity equation we assume $\frac{\partial \rho'}{\partial t} = 0$ in order to be consistent with 1. and 2.

5. From the scale analysis it also follows that horizontal advection terms like $u' \frac{\partial \bar{u}}{\partial x}$ should be neglected even if that is not necessary. These terms can be included by means of the large scale variables.

6. In the model, pressure will be computed from $\bar{p}_H$, H being the top of the model, and the predicted temperature profile from the hydrostatic equation. From total p density ρ will be computed (instead of $\bar{\rho}$). Pressure, p, is used in the calculation of q and θ (see below).

7. In most numerical weather prediction models the treatment of the atmospheric boundary layer has been very crude even if more refined formulations are coming into use at the present time. From a practical point of view, however, we assume that the background eddy diffusivity $\bar{K} = 0$. Furthermore we will also assume in all simulations in this report that $\bar{u}$ is constant with height. This latter assumption will make the term $K' \cdot \frac{\partial \bar{u}}{\partial z} = 0$. The large scale flow may, however, have a non-zero vertical wind shear due to horizontal baroclinicity. In these cases a thermal wind can be added to the constant $\bar{u}$. To provide for this we will keep the term $K' \cdot \frac{\partial \bar{u}}{\partial z}$.

The equations for the one-dimensional model then read

$$\frac{\partial u'}{\partial t} = fv' + \frac{\partial}{\partial z}\left(K'_m \frac{\partial u}{\partial z}\right) \tag{30}$$

$$\frac{\partial v'}{\partial t} = -fu' + \frac{\partial}{\partial z}\left(K'_m \frac{\partial v}{\partial z}\right) \tag{31}$$

$$\frac{\partial T'}{\partial t} + \bar{w}\frac{\partial T'}{\partial z} = \frac{\partial}{\partial z}\left\{K'_h\left(\frac{\partial T}{\partial z} + \Gamma_d + \frac{L}{c_p}\frac{\partial q_s}{\partial z} - \gamma_{cg}\right)\right\} - \frac{L}{c_p}\frac{dq_s}{dt} - \frac{1}{c_p}\cdot\frac{\partial F'}{\partial z} \tag{32}$$

$$\frac{\partial q'}{\partial t} + \bar{w}\frac{\partial q'}{\partial z} = \frac{\partial}{\partial z}\left(K'_h \frac{\partial q}{\partial z}\right) + Q'_q \tag{33}$$

$$dp = -\rho g dz \tag{34}$$

Potential temperature used in the model is calculated from

$$\theta = T\left(\frac{p_o}{p}\right)^{R_d/c_p}$$

$$p_o = 1000 \text{ mb}$$

2.7 Boundary conditions

The boundary conditions get a slightly different form than usual.

at z = 0: u = v = w = 0 gives

$$u' = -\bar{u}(0)$$
$$v' = -\bar{v}(0)$$
$$T' = T_{surf} - \bar{T}(0)$$

In the simulations with prescribed lower boundary conditions

$$\left(\frac{\partial q}{\partial z}\right)_{z=0} = 0$$

For the cases with a complete surface energy balance see section 4.3.

at z = H = the top of the model (usually at 2000 m)

$$u' = v' = T' = q' \equiv 0$$

2.8 Advantages and disadvantages with the Gutman formulation

The Gutman formulation of the equations leads to some advantages in comparison to an ordinary unsteady Ekman formulation (i e $\frac{\partial u}{\partial t} - f(v-v_g) = \frac{\partial}{\partial z}\left(K \frac{\partial u}{\partial z}\right)$.

1. The absence of the geostrophic wind in eqs (30) and (31) filters out the class of diffusive-intertial oscillations generated by a changing geostrophic wind in an ordinary Ekman formulation.

These oscillations have been discussed theoretically by Ching & Businger (1968) but, to the knowledge of the author, never been observed. The "filtering effect" of the Gutman formulation is demonstrated in Bodin (1974). This formulation, however, only changes slightly the capability of the model to simulate the intertial oscillations leading to the formation of a nocturnal jet as described by Blackadar (1957).

2. No need to specify both the geostrophic and the "real" wind at the upper boundary.

3. Implicit incorporation of the effects of large scale advections by means of the background variables (note that a change in a background variable affects practically the whole ABL). This effect might, however, be disadvantageous if observed values are used as background data. This will be illuminated in connection with the numerical simulations.

4. Simple adaptations to a synoptic scale numerical model supplying upper boundary values.

5. Problems with the Gutman formulation may arise when actually observed values are used as background values. The differences between a simulation by means of the present formulation of the equations and a conventional unsteady Ekman formulation will be discussed in section 7.4.

3. Turbulence closure

3.1 The turbulent energy equation for unsaturated and fully saturated processes

In order to be able to properly model most of the features of turbulence in the ABL without having to go to the more time-consuming and elaborate second-order closure schemes the turbulent energy equation (TE) has been used.

It is shown in this report that by means of an also properly designed mixing length it is possible to simulate very well the growth of a convective boundary layer, the non-stationary transition between the unstable and stable boundary layer and the development of the nocturnal inversion in a typically diurnally varying boundary layer.

The basic TE-equation will not be derived in this section. For that the reader is referred to, for example, Lumley & Panofsky (1964). The starting point will then be

$$\frac{db}{dt} = - \overline{u'w'} \frac{\partial \bar{u}}{\partial z} - \overline{v'w'} \frac{\partial \bar{v}}{\partial z} + \frac{g}{\theta} \overline{w'\theta'} - \\ - \frac{\partial}{\partial z} \left(\overline{w'b'} + \frac{\overline{p'w'}}{\rho} \right) - \varepsilon \qquad (35)$$

where b is defined by

$$b = \frac{1}{2} \{ \overline{u'^2} + \overline{v'^2} + \overline{w'^2} \} \qquad (36)$$

where primes and bars have their usual meaning as turbulent fluctuations and time averages.

The first two terms represent the generation of turbulent energy by shearing stress. The third term, proportional to the heat flux, $\overline{w'\theta'}$, is the generation or destruction of turbulent energy by buoyancy. The fourth term expresses a redistribution of turbulent energy by the turbulence itself and by pressure fluctuations. Finally ε represents the local dissipation of turbulent energy.

In order to close the system we make use of the assumptions (3) and (10). Furthermore, by dimensional arguments (see for example Monin & Yaglom (1971) or Donaldson (1973)) the dissipation ε can be written as

$$\varepsilon = a_3 \cdot b^{3/2} / \ell_\varepsilon \qquad (37)$$

where ℓ_ε is a dissipation length scale and a_3 a constant.

The fourth term is modeled in a way commonly done (see for example Shir (1973))

$$\overline{w'b'} + \frac{\overline{w'p'}}{\rho} = a_2 K_m \frac{\partial b}{\partial z} \qquad (38)$$

where a_2 is a constant of the order of one.

By means of these semi-empirical assumptions we get the TE-equation in the form

$$\frac{\partial b}{\partial t} = K_m\left(S^2 - \frac{g}{\theta}\alpha_T\left(\frac{\partial \bar{\theta}}{\partial z} - \gamma_{cg}\right)\right) + a_2 \frac{\partial}{\partial z}\left(K_m \frac{\partial b}{\partial z}\right) - \frac{a_3 b^{3/2}}{\ell_\varepsilon} \qquad (39)$$

where α_T is the ratio K_h/K_m,

γ_{cg} is the countergradient heat flux correction discussed in section 3.3, and

$$S^2 = \left(\frac{\partial \bar{u}}{\partial z}\right)^2 + \left(\frac{\partial \bar{v}}{\partial z}\right)^2 \qquad (40)$$

Eq (39) makes no provision for the change in buoyancy and turbulence structure when the air is saturated and condensation occurs like in a fog or in stratus clouds. By means of the assumption of conservation of static energy h_s it is possible to modify the TE-equation in a similar way as the thermodynamic equation. The underlying assumption is that condensation and evaporation are reversible processes with a time-scale for the phase-changes of water similar to the dominating turbulent fluctuations. In fogs and stratus clouds with a small water content and small drops this seems to be justified. For a more extensive derivation the reader is referred to appendix I.

The actual change in eq (39) consists of an extra term in the heat flux term similar to eq (11)

$$\frac{\partial b}{\partial t} = K_m\left(S^2 - \frac{\alpha_T g}{\theta}\left(\frac{\partial \bar{\theta}}{\partial z} + \frac{L}{c_p}\frac{\partial \bar{q}_s}{\partial z} - \gamma_{cg}\right)\right) +$$

$$+ a_2 \frac{\partial}{\partial z}\left(K_m \frac{\partial b}{\partial z}\right) - a_3 \frac{b^{3/2}}{\ell_\varepsilon} \qquad (41)$$

3.2 Closure assumptions, constants and boundary conditions

Eq (41) is the form of the TE-equation used in the model. Some further assumptions, however, have to be made in order to close the system. In order to relate the turbulent energy to the eddy diffusion coefficient K_m will make use of a mixing length hypothesis. Dimensional reasoning gives

$$K_m = a_4\, b^{1/2} \cdot \ell \qquad (42)$$

The mixing length in eqs (41), (the dissipation mixing length) and in (42) are not necessarily the same. However, we will assume that they are equal in the model i e

$$\ell = \ell_\varepsilon$$

This will be reflected in the choice of the multiplying constant in the dissipation term. The proportionality constant a_4 can be determined from the ratio u_*^2/b close to the ground. Peterson (1972) gives a value of 0.16 and Zilitinkevich et al. (1967) 0.21 but the result is not critically dependent on the exact value. For convenience we choose a value of 0.2. Eq (42) then reads

$$K_m = (0.2b)^{1/2} \cdot \ell \qquad (43)$$

Furthermore, close to the ground we should have an approximate balance between the generation of turbulent energy by shear stress and dissipation.

That gives us, since $u_*^2 = \frac{\tau}{\rho} = K_m \frac{\partial \bar{u}}{\partial z}$ and $K_m = kzu_*$ close to the ground:

$$K_m S^2 = \varepsilon \text{ or } \frac{u_*^3}{kz} = \frac{a_3 (b^{3/2})}{kz} \qquad (44)$$

where we have assumed that ℓ approaches kz when $z \to 0$. k is von Karman's constant = 0.35 (from Businger et al. (1971)). Since $K_m = kzu_* = (0.2b)^{1/2} \cdot kz$ we get $b = \frac{1}{0.2} u_*^2$. This gives us $a_3 = (0.2)^{3/2}$ and

$$\varepsilon = \frac{(0.2b)^{3/2}}{\ell} \qquad (45)$$

The data by Businger et al. (1971) also indicates that the ratio

$$\alpha_T = \frac{K_h}{K_m} = 1.35 \text{ for neutral conditions}$$

in the surface layer. In stable conditions α_T is fairly constant out to stability values $\zeta = z/L = 3.5$ where L is the Monin-Obukhov length and

$$L = - \frac{u_*^3}{k \frac{g}{\Theta} w'\Theta'} \qquad (46)$$

For unstable stratifications α_T increases up to 2.5 for $\zeta = -2.5$.

The models, as it seems, is not very sensitive to variations in α_T and α_T has been chosen in the first version to be constant and equal to 1.35 over the whole stability range. It is, however, possible to include a variation of α_T as given by measurements in the surface layer. No data, however, are available for the variation of α_T in the Ekman layer.

Finally the constant a_2 is taken to be 1.2, which is the value used by Yamada & Mellor (1975). Zilitinkevich et al. (1967) gives a value of 0.7 but then α_T is set to 1 instead of ~ 2.5 in free convection.

Boundary conditions for b

The existence of a logarithmic layer close to ground implies, as above, that the lower boundary condition for b should be

$$z=z_o \quad b = 5.0\, u_*^2 = 5.\ell^2 S^2 = 5.0 \cdot k^2 z_o^2 S^2 \qquad (47)$$

This condition, however, underestimated the turbulent energy in unstable conditions, presumably because of the first gridpoint being at 5 cm. Delage (1974) used the boundary condition

$$\frac{\partial b}{\partial z} = 0 \quad z = 0 \qquad (48)$$

in his simulation of the nocturnal boundary layer with very similar results as eq (47). This boundary condition was tested in the present model yielding an improvement for the unstable boundary layer. The formulation (48) has therefore been adopted.

At the upper boundary we apply the same condition, i e eq (48).

3.3 The countergradient heat flux term

Observations have indicated that in a convective boundary layer capped by an inversion the air has a lapse rate which is slightly stable, i e potential temperature is increasing slightly with height in the central and upper parts of the boundary layer.

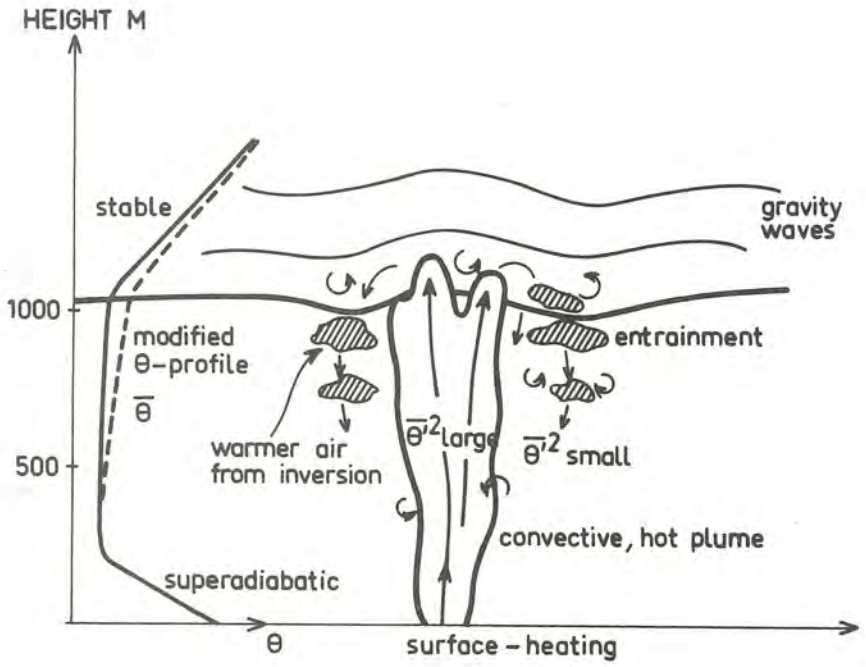

Figure 2

Mass continuity requires a downward transport of warmer air from the inversion above the convective layer. Each new plume from the heated surface a typical summerday is slightly warmer than the previous one and therefore penetrates somewhat higher up into the inversion. New portions of warm air push the former ones ahead downward. This gives rise to a heating of the upper part of the ABL slightly stabilizing the mean temperature profile.

The fact that measured heat flux profiles show a positive, upward, heat flux implies that looked upon from the point of view of mean temperature profiles heat is actually transported counter to the gradient. This has been demonstrated in simultaneous heat flux and temperature observation by Lenshow (1970) and Warner (1971).

In figure 2 is schematically showed how this is coming about. Already Priestley and Swinbank in 1947 gave an explanation of this effect in terms of a mixing-length consideration. Deardorff (1966) suggested that the effect of the "counter gradient" heat flux could be parameterized by a simple additional term γ_{cg} in the expression for the heat flux

$$\overline{w'\theta'} = - K_h \left(\frac{\partial \overline{\theta}}{\partial z} - \gamma_{cg}\right) \qquad (49)$$

In Deardorff (1972), on the basis of the temperature variance equation, an expression for γ_{cg} is derived and

$$\gamma_{cg} \simeq \frac{g}{\theta} \cdot \frac{\overline{\theta'^2}}{\overline{w'^2}} \qquad (50)$$

Measurements of $\overline{\theta'^2}$ and $\overline{w'^2}$ give values of γ_{cg} ranging from 0.3 K/km to 3.0 K/km. The contribution to γ_{cg} is proportional to the temperature variance, which, as indicated in the figure, is much larger in a thermal plume than in the ambient air.

Deardorff (1973) used results from his 3-dimensional boundary layer model to estimate the ratio of the temperature variance and the vertical velocity variance and suggests the following form of γ_{cg}

$$\gamma_{cg} = \frac{10.(\overline{w'\theta'})_s}{w_* \cdot h} \qquad (51)$$

where $(\overline{w'\theta'})_s$ is surface heat flux, h the height of the boundary layer and w_* a scaling velocity

$$w_* = \left(\frac{g}{\theta} (\overline{w'\theta'})_s \cdot h\right)^{1/3} \qquad (52)$$

In (51) and (52) the height of the mixed layer, h, enters as an important parameter. As would be expected from simple physical reasoning γ_{cg} is greatest when the boundary layer is comparatively thin. When it grows γ_{cg} decreases to values of the order of 0.1-0.3 K/km.

3.4 Mixing length formulation

The remaining entity to specify in order to close the turbulence parameterization is the mixing length ℓ. This problem is one of the most important aspects of the model. In Bodin (1978) is discussed different formulations of ℓ. Several expressions for ℓ have been tested in the present model. We will discuss separately the stable case and the unstable case.

1. Stable case, surface heat flux, $\overline{w'\theta'}_s<0$

The first expression for ℓ tested was that used by Delage (1974), slightly modified:

$$\frac{1}{\ell} = \frac{1}{k(z+z_o)} + \frac{1}{\lambda} + \frac{\beta}{kL} \qquad (53)$$

where L is the Monin-Obukhov length

λ an estimate of the upper limit of ℓ proportional to the boundary layer height

z_o is the roughness height

β = 4.7 from surface layer measurements

Eq (53) with $\lambda = 4\cdot10^{-4}\cdot\frac{|V_g|}{|f|}$ is an extension of Blackadar's formulation from 1962. More often the constant in λ has been taken as $2.7\cdot10^{-4}$. Eq (53) gives a limit consistent with surface layer theory. The last term β/kL is a local stability term implying that the Monin-Obukhov length is the limiting length scale in stable stratification. Physically it seems reasonable that the mixing-length goes to zero in very stable stratification. As pointed out by Delage (1974), however, the height of the nocturnal boundary layer with this formulation is grossly underestimated.

In eq (53) we drop the last stability dependent term and modify the length scale λ to be

$$\lambda = 0.2\cdot h \qquad (54)$$

where h is the height of the mixed layer. Several definitions of h have been tested.

Among the ones giving too slow a growth of the ABL is

$$Ri(h) = Ri_c \qquad (55)$$

where R_c is a critical Richardson number for the onset of turbulence. Ri_c = 0.4 and 0.7 gave no difference.

λ defined as above has also been tested but with $|\mathbb{V}|$ instead of $|\mathbb{V}_g|$ since $|\mathbb{V}_g|$ is not available in the model. The best results, however, were obtained by

$$h = 0.1 \cdot \frac{u_*}{|f|} \qquad (56)$$

This means that ℓ is given by

$$\frac{1}{\ell} = \frac{1}{k(z+z_o)} + \frac{1}{0.2h} \qquad (57)$$

The mixing length formulated in this way is only bounded by the dynamical equilibrium height scale $u_*/|f|$ and not by L. The reason why the formulation (57) works better than eq (53) might be the presence of gravity waves in the inversion above the mixed layer. Now and then gravity waves break creating turbulence thereby letting the ABL grow into regions where Ri>0.25. The mixing length according to eq (57) does not prevent this growth but acts as a potential mixing length in layers where turbulence is not yet present. With this formulation the nocturnal inversion rises at about the correct rate. This is evident from the Wangara data simulations and the simulation of the Finnish data presented in sections 7 and 8.

2. <u>The unstable case, surface heat flux $\overline{w'\theta'}_s > 0$</u>

The mixing length in unstable conditions must be able to reflect the dramatic change in size of the energy transporting eddies. Results from Deardorff's numerical simulations (Deardorff (1973), (1974)) show that ℓ very rapidly grows beyond its neutral value with height, z, to a maximum value of 0.8h in the middle of the mixed layer under near free-convection conditions.

At the same time the formulation of ℓ must have a correct neutral limit. Most formulations of ℓ to-day give too small values of ℓ in unstable conditions. This is true for, for example, Djolov's formulation, used by Yu (1976), and Blackadar's (1962) used by Yamada & Mellor (1975). In Yu there is obviously too little mixing in the convective ABL and the ABL is growing too slowly in Yamada & Mellor's formulation.

Another formula, used by Gutman and collaborators, relates ℓ to values of turbulent energy at lower levels. This, however, does not allow ℓ to grow rapidly enough in the lower parts of the ABL.

The formulation of ℓ used in this model is suggested by Deardorff (personal communication) and is an interpolation for ℓ_ε given in Deardorff (1974b), figure 19.

$$\frac{1}{\ell} = \frac{1}{\ell_N} - \frac{1}{h} \frac{1+1.32 \frac{z+z_o}{h}}{0.001+ \frac{k(z+z_o)}{h}} \cdot \frac{1}{1-a \cdot \frac{L_o}{h}} \qquad (58)$$

L_o is the surface Monin-Obukhov length and
ℓ_N is defined as in eq (57) but with a different definition of h.

The height of the ABL, h, in unstable conditions was previously assessed from the heat flux profile but is at the present time calculated from the potential temperature profile (see section 6.6.3).

Eq (58) has the limit ℓ_N when $L_o \to \infty$ and ℓ_{max} reaches a value of 0.8h when $L_o \to 0$. Deardorff suggested a value of a=1 but it proved to give a too rapid approach to free convection conditions. Instead a has been chosen as having a value of 50. Furthermore eq (58) gives too large values of ℓ at the base of the capping inversion thereby over-estimating the downward heat flux in the stable layer.

ℓ as determined by eq (58) has therefore been modified by simple multiplying ℓ from eq (58) by a linearly decreasing function defined by

$$\begin{aligned} g(z) &= 1.9 - 1.8\,\frac{z}{h} \quad 0.5h < z < 1.1h \\ g(z) &= 0.1 \qquad\qquad\quad z \geqslant 1.1h \end{aligned} \tag{59}$$

This formulation of the mixing length allows a consistent transition between unstable and stable conditions and vice versa in the diurnal cycle of the ABL.

4. Surface energy balance

4.1 Surface temperature equation

The surface temperature, T_o, is needed as a lower boundary condition for temperature in eq (32). T_o is defined as the temperature at the interface between the atmosphere and the soil, i e T(o). The most widely used method for getting the surface temperature is to assume a balance of the different heat fluxes at the surface. If we define F_{ts} to be the turbulent flux of sensible heat, F_ℓ to be the latent heat flux, F_s to be the soil heat flux and R_{net} to be the net radiative (long wave and short wave flux) at the surface we can write the energy balance condition as

$$\varepsilon_s\,\sigma T_o^4 + R_{net} + F_{ts} + F_\ell - F_s = 0 \tag{60}$$

ε_s is the surface emissivity.

Usually F_{ts}, F_ℓ and F_s are functions of T_o making eq (60) a 4th order algebraic equation to be solved numerically by, for example, iterative techniques.

In this model we will instead make use of an approximative predictive equation for T_o which avoids a solution of the kind necessary for eq (60). This equation will be a consistent numerical analogue of eq (60). Such an equation was used by Karlsson (1972).

To derive the prognostic equation for T_o we consider the surface and the adjacent layers of air and soil as depicted in figure 3.

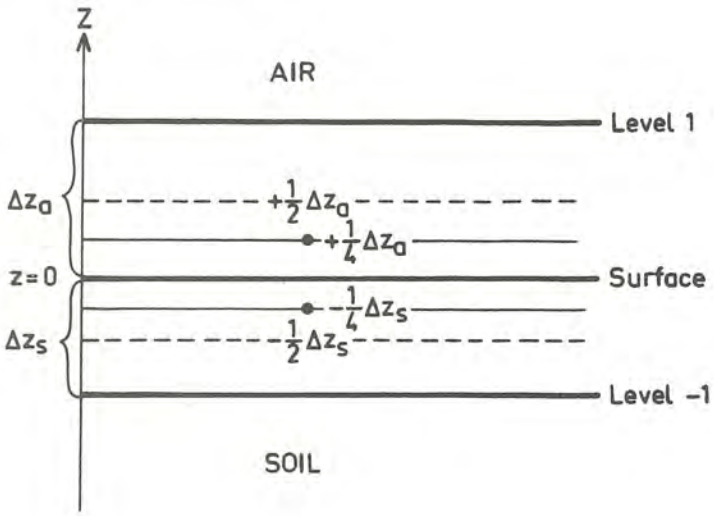

Fig 3
The lowest layer of the atmosphere and the topmost layer in the ground in the model.

At the points at $+\frac{1}{4}\Delta z_a$ and $-\frac{1}{4}\Delta z_s$ we can formulate simple thermodynamic equations given by

$$\frac{\partial T}{\partial t} = -\frac{1}{\rho_i c_i}\frac{\partial F}{\partial z} \qquad (61)$$

where c_i is the specific heat capacity for air, i=a, or the soil, i=s. ρ_i is the density for the medium considered. In the air we get

$$\frac{1}{2}\rho c_p \Delta z_a \frac{\partial T_a}{\partial t} = -F_a(\frac{1}{2}\Delta z_a) + F_a(o) \qquad (62)$$

where F_a is the total energy flux in the lowest atmospheric layer. For the soil layer we get

$$\frac{1}{2}\rho_s c_s \Delta z_s \frac{\partial T_s}{\partial t} = -F_s(o) + F_s(-\frac{1}{2}\Delta z_s) \qquad (63)$$

From eq (60) we have $F_s(o) = F_a(o)$.

After adding eqs (62) and (63)

$$\frac{1}{2}(\rho c_p \Delta z_a \frac{\partial T_a}{\partial t} + \rho_s c_s \Delta z_s \frac{\partial T_s}{\partial t} = F_s(-\frac{1}{2}\Delta z_s) -$$

$$- F_a(\frac{1}{2}\Delta z_a) \qquad (64)$$

We now make a series expansion of the temperature T_a and T_s getting

$$\frac{\partial T_a}{\partial t} = \frac{\partial}{\partial t}(T_o + \frac{1}{4}\Delta z_a \frac{\partial T_{o+}}{\partial z} + ...)$$

$$\frac{\partial T_s}{\partial t} = \frac{\partial}{\partial t}(T_o - \frac{1}{4}\Delta z_s \frac{\partial T_{o-}}{\partial z} + ...)$$

Substituting $\frac{\partial T_a}{\partial t}$ and $\frac{\partial T_s}{\partial t}$ in eq (64) and neglecting second order terms of the type

$\frac{1}{8} \cdot \rho c_p (\Delta z_a)^2 \frac{\partial^2 T_o}{\partial z \partial t}$ we get

$$c^* \cdot \frac{\partial T_o}{\partial t} = F_s(-\frac{1}{2}\Delta z_s) - F_a(\frac{1}{2}\Delta z_a) \qquad (65)$$

where c^* is an average heat capacity for the air-soil layer

$$c^* = \frac{1}{2}\{\rho c_p \Delta z_a + \rho_s c_s \Delta z_s\} \qquad (66)$$

In the model eq (65) is used to predict surface temperature. The fluxes of sensible heat, latent heat and soil heat are computed exactly at $z = \frac{1}{2}\Delta z_a$ and $z = -\frac{1}{2}\Delta z_s$.

The flux F_a is given by

$$F_a = -\rho c_p k_h (\frac{\partial \theta}{\partial z} - \gamma_{cg}) - \rho L K_h \frac{\partial q}{\partial z} - F_R - F_{sun} \qquad (67)$$

and

$$F_s = -\kappa \frac{\partial T_s}{\partial z} \qquad (68)$$

where $F_R = \varepsilon_s \sigma T^4 - F\downarrow(o)$
and κ the thermal conductivity of the soil.

4.2 Soil temperature

In eq (68) we need the soil temperature. It is computed by solving the heat conduction equation for a top soil layer assuming homogeneous thermal properties.

The heat transfer equation is simply

$$\frac{\partial T_s}{\partial t} = K_s \cdot \frac{\partial T^2_s}{\partial z^2} \qquad (69)$$

where $K_s = \kappa/\rho_s c_s$ is the thermal diffusivity.

The boundary conditions for eq (69) are

at z=0: $T_s = T_o$

z=-D=-1m: $T_s = T_d$ = constant

The constants K_s and κ are usually difficult to get from measurements and they normally vary considerably with soil water content. In some simulations they have been systematically varied to give realistic maximum and minimum surface temperatures. The effect of different K_s and κ has been discussed by Long and Shaffer (1975) and Zdunkowski and Trask (1971).

4.3 Soil water

In order to get the latent heat flux at the surface we need the specific humidity at the surface, q(o). Many modelers have been using the so-called Halstead parameter, H, (Halstead et al. (1954)). This formulation and a formulation based on a given, constant, relative humidity at the surface are compared in Nappo (1975). In the present model surface specific humidity is based on the Halstead parameter approach but connected to a simple soil moisture model suggested by Forsman and Bergström at SMHI (personal communication). More elaborate soil moisture models have been used by Zdunkowski et al. (1975) and Sasamori (1970).

The approach taken here is admittedly a weak point of the model. However, the problem is complicated and no satisfactory solution exists today taking into account the effect of vegetation and evapo-transpiration. There are, however, some simplified parameterizations that are worth trying. These are reviewed by Deardorff (1977).

In this section we denote evaporation from the surface by E and the potential evaporation, i e the evaporation from a completely wet surface by E_p and soil water content by w. The Halstead parameter is then defined as

$$H = E/E_p = f(w) \qquad (70)$$

where f(w) is a function of soil water content. This function will be defined as a piecewise linear function outlined in figure 4.

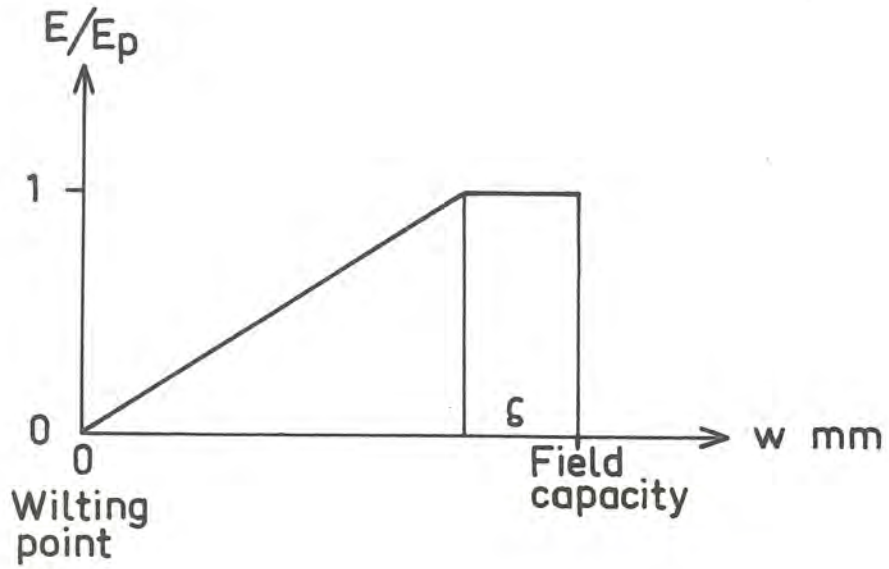

Fig 4

The form of the function f(w) shows that we can have potential evaporation before the ground is completely wet. This is usually observed in reality even if the range δ above varies between different types of soil. The water content w is allowed to vary due to rain, evaporation and ground water run-off.

The ground and the interface are regarded as two interlinked reservoirs as shown in fig 5. When it rains the upper, interception reservoir, gets filled first before any water penetrates into the ground. This reservoir is usually of the order of 5 mm and corresponds to the rain water that adheres to the vegetation and the foliage of the trees. If there is water in the interception reservoir evaporation takes place from that before water in the ground is used.

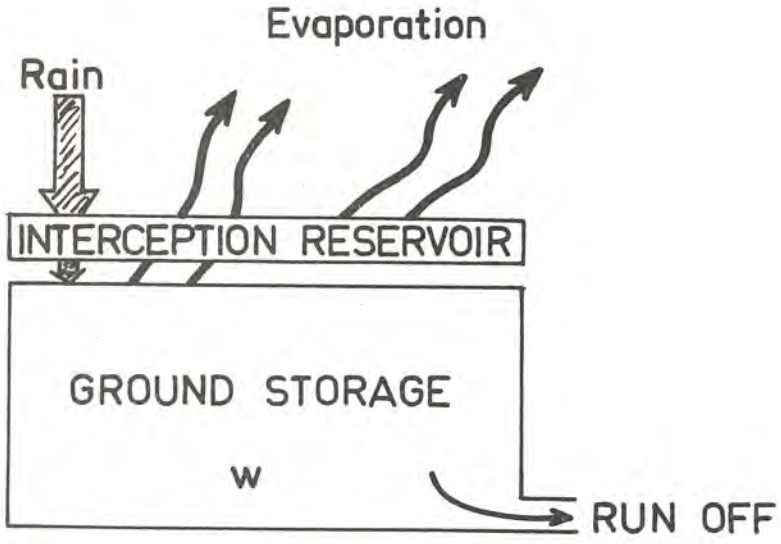

Fig 5

The relation between run-off and precipitation, depends on the soil moisture content. The higher soil moisture content the larger the run-off. If we denote the stored precipitation by Δw, hydrologists suggest the following relation

$$\Delta w/P = (1 - \frac{w}{FC})^{\beta} \qquad (71)$$

where $\beta \sim 2\text{-}3$ and FC is the field capacity. P is precipitation.

In the simulation runs so far there is no rain and the soil water content is allowed only to vary, i e decrease, because of evaporation.

This decreases w and because of eq (70) and fig 5 the evaporation decreases.

Knowing f(w) we can compute q(o) from the following equation

$$q(o) = (q_s(o) - q(z_1)) \cdot f(w) + q(z_1) \qquad (72)$$

where $q_s(o)$ is saturation specific humidity and z_1 is the first level above the ground in the model.

5. Radiation

The radiation subroutine is taken from Shaffer & Long (1973) with some slight modifications. It is based on the radiation scheme developed by Atwater (1970). The major difference from Atwater is the neglection of the influence of air pollution and aerosols. The scheme treats the incoming solar radiation in a simplified way, allowing for absorbtion and scattering by clouds above and in the ABL, where also heating of clear air is accounted for. Long wave radiation is treated by solving the radiative heat transfer equation by means of the emissivity approximation.

5.1 Solar radiation

The solar radiation reaching the top of the atmosphere is roughly 1400 W/m^2 or 2.0 $cal/cm^2 \cdot min$. Part of this is absorbed by water vapor and other absorbers and part of it is scattered back to space. In the upper atmosphere, i e above the boundary layer, the absorbtion due to water vapor is given by McDonald (1960) and

$$A_w = 0.077(u \sec z)^{0.3} \qquad (73)$$

where u is the path length and z the zenith angle and sec z = 1/cos z.

The transmitted short wave radiation, neglecting the influence of water vapor but accounting for scattering, is according to Kondratyev (1969)

$$\tau = 1.041-0.16\{(0.949\ \frac{p_H}{p_o} + 0.051)\sec z\}^{1/2} \quad (74)$$

where p_H is the pressure at the top of the BL and p_o = 1000 mb.

The amount of solar radiation that reaches the top of the PBL is then, in the absence of clouds,

$$F_s = F_o \cos z\ (\tau - A_w) \quad (75)$$

where F_o is the incident solar radiation at the outer edge of the atmosphere. $F_s = 0$ if $\cos z \leqslant 0$. Clouds above the boundary layer are treated in a simplified way. From predicted relative humidities in the troposphere, from the large scale model, or from cloud observations the fractional cloud cover can be estimated. Each of these cloud categories has a transmission function as given by Pandalfo et al. (1971).

$$\begin{aligned} T_{low} &= 0.35 - 0.15 \cdot \sec z \quad i=1 \\ T_{middle} &= 0.45 - 0.01 \cdot \sec z \quad i=2 \\ T_{high} &= 0.9 - 0.04 \cdot \sec z \quad i=3 \end{aligned} \quad (76)$$

From predictions of liquid water content in the PBL it will also be possible to include

$$T_{PBL} = 0.25 - 0.01 \sec z \quad (77)$$

The resulting short wave flux at the top of the PBL will then be

$$F_{PBL} = F_s \cdot \prod_{i=1}^{3} (1-c_i(1-T_i)) \quad (78)$$

where c_i is the cloud cover of category i.

Within the PBL the absorbtion by water vapor in a layer of optical thickness du is

$$dA_w = - 7.55 \times 10^{-4} (u \sec z)^{-0.7} du \qquad (79)$$

Furthermore, scattering is given by

$$dS = - 7.592 \cdot 10^{-5} \cdot F_o \cdot \{(0.949 \frac{p}{p_o} + 0.051) \sec z\}^{-1/2} \cdot dp \qquad (80)$$

The final flux at the surface will then be

$$F_{surf} = (F_{PBL} + \int_{p_H}^{p_o} (dA_w + dS))(1 - C_{PBL}(1 - T_{PBL})) \qquad (81)$$

The surface will reflect part of this radiation. With the albedo being A we get the solar radiation absorbed at the surface as

$$F_{abs} = (1-A)F_{surf} \qquad (82)$$

The heating by the reflected radiation will not be taken into account. The amount of solar radiation absorbed in the PBL as given by (79) will be used to heat the air correspondingly.

5.2 Long wave radiation

The heating or cooling in a layer due to long wave radiation flux divergence is calculated from the radiative transfer equation. The net radiation, F^{ν}_{net} for the frequency ν at the level z can be written as the sum of the downward and upward energy fluxes, $F^{\downarrow}_{\nu}$ and $F^{\uparrow}_{\nu}$. The upward flux is defined to be positive.

According to, for example, Kondratyev (1969), the transfer equation can be written

$$F^{\nu}_{net} = F^{\uparrow}_{\nu} + F^{\downarrow}_{\nu} = F^{\uparrow}_{\nu}(o)T_{\nu}(o,z) + \int_{o}^{z} \Pi B_{\nu}(z') \frac{dT_{\nu}(z',z)}{dz'} dz' - \int_{z}^{\infty} \Pi B_{\nu}(z') \frac{dT_{\nu}(z,z')}{dz'} dz' \qquad (83)$$

where $F\uparrow(o)$ is the flux emitted by the lower boundary and $T_{\nu}(z',z)$ is the transmission function for the frequency ν in the layer z to z'. Eq (83) has to be integrated over frequency to give a total net flux.

There are many ways of doing this. In this radiation model the integration over frequence problem is solved by making use of the so-called emissivity approximation (see Rodgers (1977)). Instead of the transmission function we introduce an absorbtion function A = 1-T.

For the downward flux we can write

$$F\downarrow = \int_{o}^{\infty} d\nu \int_{z}^{\infty} \Pi \frac{dA}{dz'} B(z')dz' = \int_{z}^{\infty} \frac{dE(z,z')}{dz'} \sigma T^4(z')dz' \qquad (84)$$

where $E(z,z') = \int_{o}^{\infty} d\nu \int_{z}^{z'} \frac{dA\Pi}{dz''} \frac{B(\nu,z'')}{\sigma T^4(z'')} dz''$ (85)

The emissivity function is usually obtained from measurements. E(z,z') is usually defined as a function of a pressure corrected optical path length u, i e E(u).

Also expressing the upward flux by means of the emissivities we get the total net flux through a level z in the absence of clouds.

$$F_{net} = \varepsilon_s \sigma T^4 \cdot (1-E(0,z)) - \int_{o}^{z} \sigma T^4 \frac{dE}{dz'} dz' + F\downarrow(o)(1-\varepsilon_s)(1-E(o,z)) + \int_{z}^{\infty} \sigma T^4 \frac{dE}{dz'} dz' \qquad (86)$$

where the third term on the right hand side expresses the reflected radiation at the surface. ε_s is the surface emissivity.

In the computations it is assumed that only water vapor and carbon dioxide are active. It is also assumed that the absorbtion bands are not overlapping, i e the emissivities are additive.

The emissivities for water vapor are taken from measurements by Kuhn (1963) expressed in the form of simple logarithmic functions as given by Atwater (1974).

A pressure corrected path length for water vapor is defined as

$$\Delta u = u(z,z') = \int_z^{z'} \frac{p}{p_o} \rho_w u dz = -\frac{1}{g} \int_{p_z}^{p'_z} \frac{p}{p_o} q_v \, dp \qquad (87)$$

In terms of u, E is given by

$$E(u) = \begin{cases} 0.1129 \log_{10} (1+12.63u), & \log u \leq -4 \\ 0.104 \log (u) + 0.440, & \log u \leq -3 \\ 0.121 \log (u) + 0.491, & \log u \leq -1.5 \\ 0.146 \log (u) + 0.527, & \log u \leq -1 \\ 0.161 \log (u) + 0.520, & \log u \leq 0 \\ 0.136 \log (u) + 0.542, & \log u > 0 \end{cases} \qquad (88)$$

u is given in cm.

For carbon dioxide u is defined as

$$u_{CO_2} = \frac{1.66}{\rho^0_{CO_2}} \int_z^{z'} \rho_{CO^2} \, dz \qquad (89)$$

where ρ_{CO^2} is the density of CO_2 and $\rho^0_{CO^2}$ is the density at NTP. u_{CO^2} is in cm. The ρ_{CO^2} used in the calculations corresponds to 320 ppm.

The CO_2-emissivity is that of Kondratyev (1969)

$$E_{CO_2} = 0.185(1-e^{-0.3919u_{CO_2}^{0.4}}) \qquad (90)$$

The two emissivities are added and used in eqs (91) and (92) below.

Clouds in and above the boundary layer are regarded as black bodies. Cirrus and cirrostratus are assumed to be "half-black" bodies. If we introduce c_c for the fraction of clouds we can rewrite equation (86) to account for clouds.

For the downward long wave flux at the level z we get

$$F\downarrow(z) = \int_z^\infty \{(1-c_c(z'))\cdot c_n(z,z')\sigma T^4 \frac{dE}{dz'} + c_c(z')c_n(z,z')\cdot\sigma T^4 \cdot \frac{dE_c}{dz'}\}\, dz' \qquad (91)$$

where $E_c(z,z')$ is an emissivity function modified to account for clouds. $E_c(z,z')$ is equal to one in clouds. $C_n(z,z')$ is an effective cloudiness in the layer z to z', in which overlapping of clouds is taken into account.

For the upward flux we get in the same way

$$F\uparrow(z) = (\varepsilon_s\sigma T^4 + F\downarrow(o)(1-\varepsilon_s))(1-E(o,z))c_n(z,o) - \int_o^z \{(1-c_c(z'))c_n(z',z)\sigma T^4 \frac{dE}{dz'} + c_c(z')c_n(z',z)\sigma T^4 \cdot \frac{dE_c}{dz'}\}dz' \qquad (92)$$

6. Numerical integration

6.1 Summary of model equations

The model equations, which have to be solved numerically can be summarized:

a) PBL

$$\frac{\partial u'}{\partial t} = fv' + \frac{\partial}{\partial z}\left(K'_m \frac{\partial u}{\partial z}\right) \tag{30}$$

$$\frac{\partial v'}{\partial t} = -fu' + \frac{\partial}{\partial z}\left(K'_m \frac{\partial v}{\partial z}\right) \tag{31}$$

$$\frac{\partial T'}{\partial t} + \bar{w}\frac{\partial T'}{\partial z} = \frac{\partial}{\partial z}\left\{K'_h\left(\frac{\partial T}{\partial z} + \Gamma_d + \frac{L}{c_p}\frac{\partial q_s}{\partial z} - \gamma_{cg}\right)\right\} - \frac{L}{c_p}\frac{dq_s}{dt} - \frac{1}{c_p}\frac{\partial F'}{\partial z} \tag{32}$$

$$\frac{\partial q'}{\partial t} + \bar{w}\frac{\partial q'}{\partial z} = \frac{\partial}{\partial z}\left(K'_h \frac{\partial q}{\partial z}\right) + Q'_q \tag{33}$$

$$\frac{\partial b}{\partial t} = K_m\left(S^2 - \alpha_T \frac{g}{\Theta}\left(\frac{\partial \Theta}{\partial z} + \frac{L}{c_p}\frac{\partial q_s}{\partial z} - \gamma_{cg}\right)\right) + 1.2\frac{\partial}{\partial z}\left(K_m \frac{\partial b}{\partial z}\right) - \frac{(0.2b)^{3/2}}{\ell} \tag{41}$$

b) soil and surface

$$\frac{\partial T_s}{\partial t} = K_s \frac{\partial^2 T_s}{\partial z^2} \tag{69}$$

$$c^* \frac{\partial T_{surf}}{\partial t} = \left[-\kappa \frac{\partial T_s}{\partial z}\right]_{-1/2\Delta z_s} + \left[\rho c_p K_h\left(\frac{\partial \Theta}{\partial z} - \gamma_{cg}\right) + \rho L K_h \frac{\partial q}{\partial z}\right]_{1/2\Delta z_a} + F_R + F_{sun} \tag{65}$$

6.2 Time integration

All of the equations can be formally written as

$$\frac{\partial Q}{\partial t} = \frac{\partial}{\partial z}\left(K \frac{\partial Q}{\partial z}\right) + G \qquad (93)$$

where Q is one of u, v, T, q, b or T_s and G represents low order terms. K usually depends on Q itself making eq (93) non-linear.

Disregarding the term G, eq (93) reduces to the diffusion equation with a variable diffusion coefficient. Numerical solutions of the diffusion equation have been studied by Long (1975), who compared several different finite difference schemes, among them Dufort-Frankel and Crank-Nicolson. Long showed that for large Fourier numbers, $K\Delta t/(\Delta z)^2$, e g for large time steps, Crank-Nicolson was superior in terms of accuracy. From an operational point of view it is desirable to use as long timestep as possible to cut down on CPU-time. A generalized Crank-Nicolson scheme as applied to equation (93) can be written

$$\frac{Q^{\tau+1}-Q^{\tau}}{\Delta t} = \mu\left[\frac{\partial}{\partial z}\left(K \frac{\partial Q}{\partial z}\right)\right]^{\tau+1} + (\mu-1)\left[\frac{\partial}{\partial z}\left(K \frac{\partial Q}{\partial z}\right)\right]^{\tau} + G^{t} \qquad (94)$$

where $t = \tau \cdot \Delta t$. If $\frac{1}{2} \leqslant \mu \leqslant 1$ the scheme is always stable. μ is a weighting factor making it possible to put more or less weight on the forward timestep $\tau+1$. When μ is equal to 1, i e all the weight is on the forward timestep, the scheme is also called Laasonen's scheme. This version has the advantage of supressing non-linear instabilities arising because of the dependence of K on Q.

It is the Laasonen scheme that is used in the present model.

6.3 Space differences

Second order centered finite differences have usually been used in approximating the diffusion term. However, as pointed out by Taylor & Delage (1971), enough accuracy is difficult to obtain in the vertical with a uniform grid point spacing Δz. Large gradients are present close to the ground and sometimes at the top of the ABL, especially at the inversion capping an unstable ABL. A natural way to proceed is to use a non-uniform grid with higher resolution in the lower layers.

One way of doing this is to make use of a transformation of the vertical z-coordinate, eq

$$\xi = \int_o^z \frac{dz'}{K(z')} \qquad (95)$$

This would get K out of the differentiation in eq (93). However, the transformation would depend on the variable K which is not known a priori but changes during the integration.

In the present model the vertical coordinate transformation is based on the shape of the neutral mixing length ℓ_N

$$\frac{1}{\ell_N} = \frac{1}{k(z+z_o)} + \frac{1}{\lambda} \qquad (96)$$

The transformation is

$$\xi = D \cdot \int_o^z \frac{dz}{\ell_N} \qquad (97)$$

which gives after integration

$$\xi = D \cdot \left(\frac{1}{k} \ell n \frac{z+z_o}{z_o} + \frac{z}{\lambda}\right) + 1 \qquad (98)$$

The constant D can be chosen to give $\Delta\xi = 1$ for a specified number of gridpoints. $\xi_o = 1$ corresponds to $z = 0$. These properties are convenient in Fortran coding.

The constant λ is chosen to be a fraction of the depth of the ABL-model, H, and

$$\lambda = a \cdot H, \; a = 0.03$$

Fig 21a shows on the left the height to every second grid point when H = 2000 m and the number of grid points is equal to 35.

In the soil the z_s-coordinate is transformed logarithmically and

$$\xi_s = a_s \cdot \ell n(bz+1) + 1 \qquad (99)$$

Fig 6 shows the vertical grid used in the model. The variables are staggered. u, v, T and q are carried in the gridpoints to the left while turbulent energy, b, and various diagnostic quantities are computed at gridpoints in between.

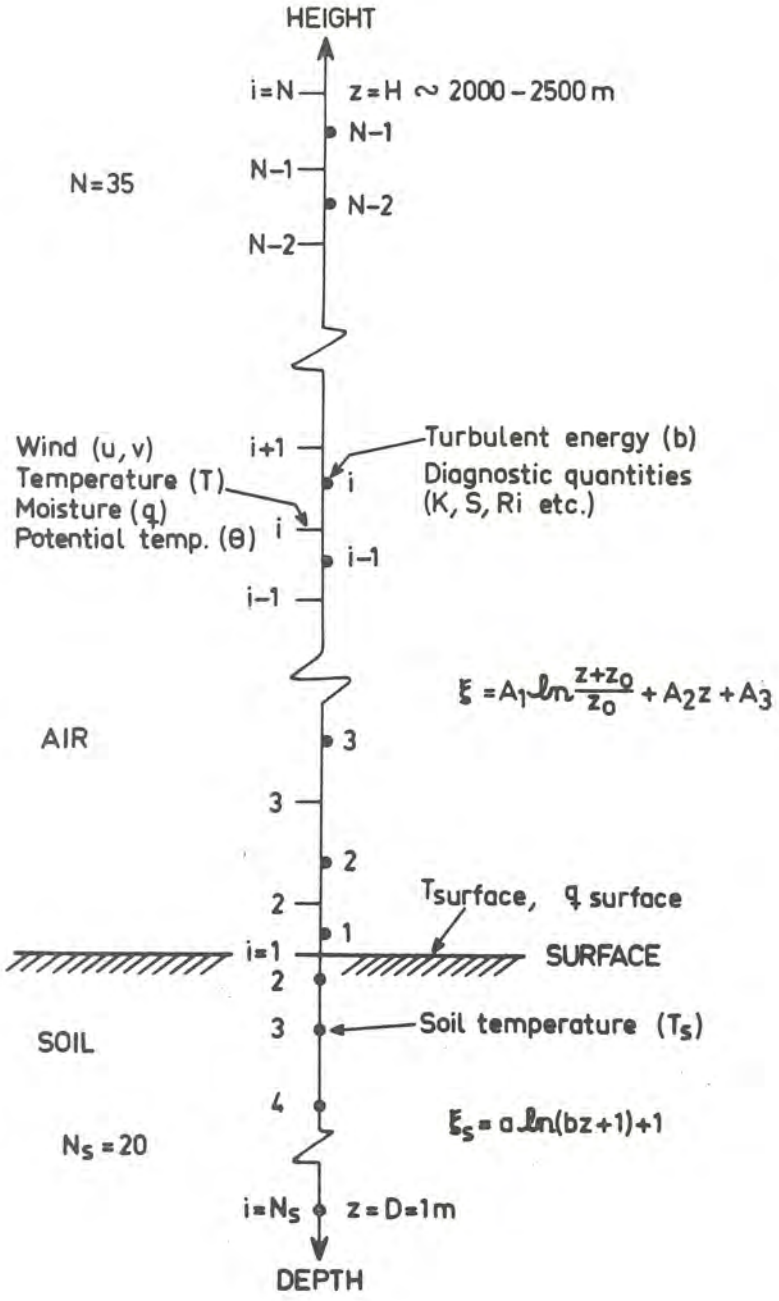

Fig 6
The vertical grid structure of the model

All vertical derivatives are transformed according to eq (98) or eq (99) respectively. Second order centered differences are then formed with a uniform grid distance $\Delta\xi = 1$.

The Laasonen scheme is applied to the diffusion terms while lower order terms are treated explicitely.

The resulting tri-diagonal matrices are inverted by means of a simple Gaussian elimination method.

The Coriolis term is treated in a special way. Eq (30) is first solved giving $u^{\tau+1}$ which is then used in eq (31), i e $-fu'^{\tau}$ is replaced by $-fu'^{\tau+1}$.

The complete finite difference equations are given in appendix II.

6.4 Solution of the thermodynamic equation

In the test integrations reported on here observed data have been used as background variables instead of LFM-predicted one's. This has some consequences for the thermodynamic equation. The background values for T, $\overline{T}$, have been extracted from observed values at the top of the model, H, and

$$\overline{T} = T_H(\text{obs})$$

In the vertical advection term in eq (32), however, is assumed that the background temperature also varies because of the large scale vertical motion as predicted by a LFM. When using observed data for $\overline{T}$ this is no longer true and the effect of large scale subsidence has to be included in eq (32) directly. This is done by changing

$$\overline{w}\,\frac{\partial T'}{\partial z} \text{ into } \overline{w}\left(\frac{\partial T'}{\partial z} + \Gamma_d\right)$$

since $\overline{T}$ is assumed constant with height.

In eq (32) we also have to approximate the term dq_s/dt. This can be done by using the definition of q (following Karlsson (1972))

$$q_s = \varepsilon\,\frac{e_s}{p} \qquad (100)$$

Differentiating (100) with respect to time gives

$$\frac{dq_s}{dt} = \frac{\varepsilon}{p}\,\frac{de_s}{dt} - \frac{\varepsilon e_s}{p^2}\,\frac{dp}{dt} \qquad (101)$$

Using Calusius-Clapeyron's formula

$$\frac{de_s}{e_s} = \frac{\varepsilon L dT}{R_d T^2} \tag{102}$$

for the phase transition "vapor to water" we get

$$\frac{L}{c_p}\frac{dq_s}{dt} \approx \frac{L}{c_p} \cdot \left(\frac{\varepsilon^2 e_s L}{pR_d T^2}\frac{dT}{dt} - \frac{e_s \varepsilon}{p^2}\frac{dp}{dt}\right) \tag{103}$$

In

$$\frac{dT}{dt} = \frac{\partial T}{\partial t} + \mathbb{V}\cdot\nabla_H T + w\frac{\partial T}{\partial z}$$

and

$$\frac{dp}{dt} = \frac{\partial p}{\partial t} + \mathbb{V}\cdot\nabla_H p + w\frac{\partial p}{\partial z}$$

we only retain the following terms, consistent with the previous approximations,

$$\frac{dT}{dt} \approx \frac{\partial T}{\partial t} + w\cdot\frac{\partial T}{\partial z} \tag{104}$$

and

$$\frac{dp}{dt} \approx -wg\rho \tag{105}$$

writing $c_q = \left(1 + \frac{q_s \varepsilon L^2}{c_p R_d T^2}\right)$ (106)

we get by using eq (17)

$$\frac{L}{c_p}\frac{dq_s}{dt} = (c_q-1)\frac{\partial T'}{\partial t} + (c_q-1)\frac{\partial \bar{T}}{\partial t} + (c_q-1)\bar{w}\frac{\partial T}{\partial z} + \frac{gLq_s}{c_p R_d T}\cdot\bar{w} \tag{107}$$

The thermodynamic equation can now finally be written as

$$c_q\frac{\partial T'}{\partial t} + \bar{w}\cdot\left\{c_q\frac{\partial T'}{\partial z} + \Gamma_d + \frac{gLq_s}{c_p R_d T}\right\} = \frac{\partial}{\partial z}\left\{K_h\left(\frac{\partial T}{\partial z} + \Gamma_d + \frac{L}{c_p}\frac{\partial q_s}{\partial z} - \gamma_{cg}\right)\right\} - (c_q - 1)\frac{\partial \bar{T}}{\partial t} - \frac{1}{c_p}\frac{\partial F'}{\partial z} \tag{108}$$

6.5 Solution of the Turbulent Energy equation

The solution of the TE-equation requires some extra consideration. It can be written in the following form

$$\frac{\partial b}{\partial t} = E_1 b^{1/2} - E_2 b^{3/2} + F \qquad (109)$$

where

$$F = 1.2\, D_z \frac{\partial}{\partial \xi}(K\, D_z \frac{\partial b}{\partial \xi}) \qquad (110)$$

$$E_1(z) = (0.2)^{1/2} \ell (S^2 - \alpha_T \frac{g}{\Theta}(\frac{\partial \Theta}{\partial z} + \frac{L}{c_p}\frac{\partial q_s}{\partial z} - \gamma_{cg})) \qquad (111)$$

$$E_2(z) = (0.2)^{3/2}/\ell \qquad (112)$$

and

$$D_z = \frac{\partial \xi}{\partial z}$$

Equation (109) is clearly non-linear in the turbulent energy b with the additional property that $b \equiv 0$ also is a solution of eq (109). We also have the requirement that $b \geqslant 0$ at all times.

We can formally write a Crank-Nicolson approximation of eq (109) as

$$\frac{b^{\tau+1}-b^{\tau}}{\Delta t} = \mu(E_1^{\tau}(b^{\tau+1})^{1/2} - E_2^{\tau}(b^{\tau+1})^{3/2} + F^{\tau+1}) + (1-\mu)\cdot(E_1^{\tau}(b^{\tau})^{1/2} - E_2^{\tau}(b^{\tau})^{3/2} + F^{\tau}) \qquad (113)$$

The coefficients are taken at timestep τ but the non-linear terms at $\tau+1$. This system has to be linearized in some way to make it possible to solve for $b^{\tau+1}$. We could also have chosen an explicit approximation. This may, however, lead to negative b and would require a shorter timestep.

Instead we follow a suggestion by Richtmeyer & Morton (1967), p 201, and linearize these terms by a Taylor series expansion in time.

We then get

$$(b^{\tau+1})^{1/2} = (b^{\tau})^{1/2} + \frac{1}{2}(b^{\tau})^{-1/2}(b^{\tau+1}-b^{\tau}) + \text{higher order terms}$$

$$(b^{\tau+1})^{3/2} = (b^{\tau})^{3/2} + \frac{3}{2}(b^{\tau})^{1/2}(b^{\tau+1}-b^{\tau}) + \text{higher order terms}$$

or

$$(b^{\tau+1})^{1/2} \approx \frac{1}{2}(b^{\tau})^{-1/2} \cdot b^{\tau+1} + \frac{1}{2}(b^{\tau})^{1/2} \qquad (114)$$

$$(b^{\tau+1})^{3/2} \approx \frac{3}{2}(b^{\tau})^{1/2} b^{\tau+1} - \frac{1}{2}(b^{\tau})^{3/2} \qquad (115)$$

In order to see the effect of the linearization we can study a test equation

$$\frac{\partial b}{\partial t} = Eb^{\alpha} \qquad (116)$$

where $\alpha = 1/2$ or $3/2$ correspond to our cases and where E can be both positive and negative.

The general Crank-Nicolson solution of eq (116) can be written after linearization as above

$$b^{\tau+1} = b^{\tau}\frac{1+E(1-\alpha\mu)\Delta t(b^{\tau})^{\alpha-1}}{1-E\alpha\mu\Delta t(b^{\tau})^{\alpha-1}} \qquad (117)$$

If $\mu = 1$ eq (117) corresponds to the Laasonen scheme.

We can now study under what conditions $b^{\tau+1}$ stays positive if $b^{\tau} > 0$ for $\mu = 1$.

I. The energy dissipation term corresponds to $\alpha = 3/2$ and $E_2 = -|E| < 0$. In this case we get

$$b^{\tau+1} = b^{\tau} \cdot \frac{1+\frac{1}{2}E_2\Delta t(b^{\tau})^{1/2}}{1+\frac{3}{2}E_2\Delta t(b^{\tau})^{1/2}} = F \cdot b^{\tau} \qquad (118)$$

The factor F is always positive definite provided that $b^\tau > 0$.

II. Bouyancy term, $\alpha = 1/2$ and $E = E_1 \gtrless 0$

$$b^{\tau+1} = b^\tau \frac{1 \pm \frac{1}{2} E_1 \Delta t (b^\tau)^{-1/2}}{1 \mp \frac{1}{2} E_1 \Delta t (b^\tau)^{-1/2}} \qquad (119)$$

where upper sign corresponds to $E>0$ and lower sign to $E<0$. In both cases we see that $b^{\tau+1}<0$ if

$$\frac{1}{2}|E_1|\Delta t (b^\tau)^{-1/2} > 1 \quad \text{even if } b^\tau > 0$$

Since E_1 can become quite large this might very well occur. The suggested form of linearization does not work well in this case.

The term $E_1 b^{1/2}$ really represents the effect of wind shear and bouyancy flux generation of turbulent energy. For $Ri>0.74$ this term is negative indicating a dying out of turbulence. However, here is an intrinsic inconsistency in the closure assumptions since the analytic solution to the equation if E_1 = const

$$\frac{\partial b}{\partial t} = - E_1 b^{1/2}$$

is

$$b = \frac{1}{2}(b_o^{1/2} - E_1 t)^2$$

, i e turbulence decays quadratically instead of, let us say, exponentially. The analytic solution is always positive but a finite difference solution (linearized) instead gives negative values for too large a time step.

The implicit scheme above for this term can give negative values for E_1 being both greater than or less than zero. An explicit scheme

$$b^{\tau+1} = (\Delta t E_1 (b^\tau)^{-1/2} + 1) b^\tau$$

can only give negative solutions when $E_1<0$.

Because of this the $E_1 b^{1/2}$-term is integrated explicitely.

To avoid negative b:s when b should approach zero the tendency is numerically adjusted in such a way that if $\Delta t E_1 < 1$

$$\Delta b = b^{\tau+1} - b^{\tau} = - 0.9999 b^{\tau} \qquad (120)$$

This is a minor alteration in the finite difference scheme and corrections of this kind only occur in the inversion capping the unstable ABL where Ri-number rapidly grows with height and b is small.

6.6 Auxiliary relations

6.6.1 Pressure

Pressure in the model is calculated from the hydrostatic relation at a height z by integrating downward from the given pressure at the top of the model, H.

Thus

$$\ell n \; p_z/p_H = \frac{g}{R_d} \sum_{i=1}^{N_z} \frac{1}{2}\left(\frac{1}{T_i} + \frac{1}{T_{i+1}}\right)\left(\frac{1}{D_z}\right)_{i+1/2} \qquad (121)$$

where $i = N_z$-NMAX, NMAX, number of highest gridpoint and N_Z number of gridpoint at level z counted from the bottom.

Density is calculated by

$$\rho_z = p/R_d T$$

6.6.2 Saturation vapor pressure

Saturation vapor pressure, e_s, is calculated for each degree between -40°C and +40°C and stored in a table, from which the actual $e_s(T)$ is interpolated. Over water ($-20^{\circ}<T<40^{\circ}C$) the following formula is used

$$e_s = 6.105 \exp\left[25.22\left(1-\frac{273}{T}\right) - 5.31 \ln \frac{T}{273}\right] \qquad (122)$$

over ice ($-40^{\circ}C<T<-20^{\circ}$)

$$e_s = 6.105 \exp\left[4.332\left(\frac{1}{273} - \frac{1}{T}\right) + 2.31 \ln \frac{T}{273}\right] \qquad (123)$$

is used from which $q_s = 0.622 \frac{e_s}{p}$ is computed.

6.6.3 Boundary layer height in unstable conditions

When the surface heat flux is upward the ABL is classified as unstable. In this case the ABL-height is needed in the mixing length formula and has to be assessed in some way.

Fig 7 shows a typical heat flux and potential temperature profile during unstable conditions.

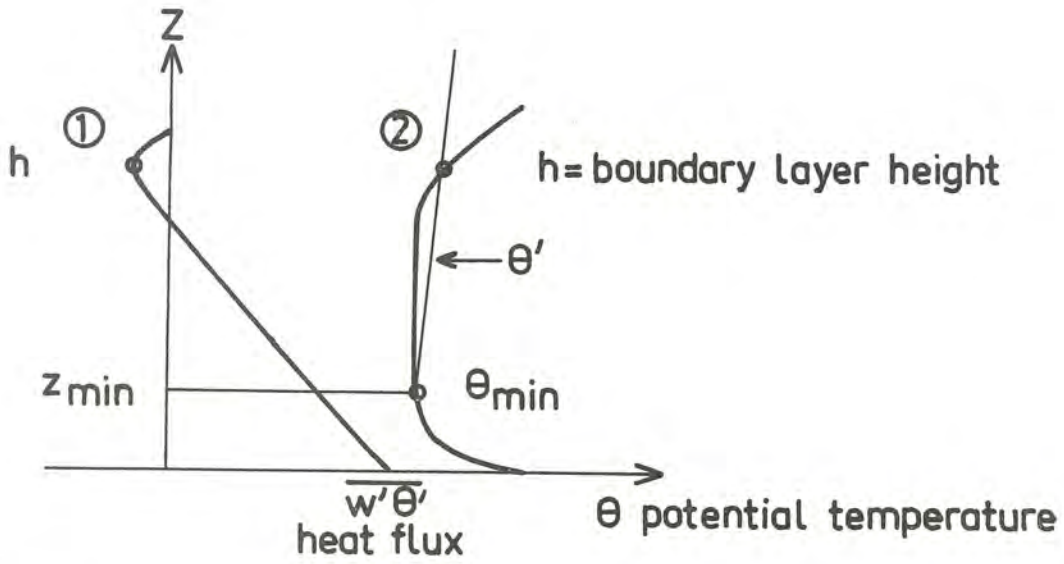

Fig 7

The first method used to assess the boundary layer height utilized the fact that the heat flux profile had a minimum (1) at some level. This level was found by fitting a quadratic polynomial to the three points closest to the observed smallest value of $\overline{w'\theta'}$. From the parabola the level of minimum heat flux was found and put equal to the boundary layer height. This method, working fine for the prediction of the mean variables, gave, however, rise to fairly large numerical oscillations, of the order of 150-200 m in the ABL-height. Instead a different method is used now.

The minimum of $\theta(z)$ is found. From this point a linear relation is established.

$$\theta' = \theta_{min} + 1.5 * \gamma_{cg}(z - z_{min})$$

The interception between $\theta'(z)$ and $\theta(z)$ yields the boundary layer height.

6.6.4 Astronomical constants

Some astronomical parameters are needed in the radiation computations.

The solar declination is calculated from

$$\delta = 23.5 \sin\{ \frac{2\Pi}{365} (DOY-80)\}$$

where DOY is the day of the year starting with one for 1 January.

The local hour angle is given by

$$HAL = (time_{GMT} - Noon_{GMT}) \cdot 15 + longitude$$

where longitude is counted negative to the east.

6.7 Numerical tests

The model was tested in a simple case to determine spatial and time truncation errors. In these tests the dry version was run from an initial steady state solution of eqs (30), (31) and (41) with a given initial temperature profile resembling the initial temperature of the Wangara data, Day 33, at 0900 local time. (Clarke et al (1971)). The background wind components were $\bar{u}$ = 5 m/s and $\bar{v}$ = 0, which were kept constant in time. Figures 8 and 9 show potential temperature profiles after 6 hours of integration and temperature profiles after 24 hours of integration for three different resolutions, 20, 30 and 65 points in the vertical between the surface and 2000 m. The surface temperature had a sinusoidal diurnal variation. Some minor differences are found at the inversion height in both cases. However, if the 65 point solution can be regarded as a high accuracy reference it is clear that 20 points are enough to simulate the diurnal course of a dry ABL.

In the Wangara data simulations 35 points between the surface and 2000 m have been used to conform to the resolution of the observations.

Similar tests have been carried out with different time steps ranging from 30 seconds to 6 minutes. No appreciable deterioration was found for Δt = 4 minutes, the time step presently used.

No signs of numerical instability are present. The integrated kinetic energy and static energy are checked every time step in order to detect numerical instability. However, some slight oscillations in surface temperature have been noticed around sunset and in late morning before sunrise.

7. Simulations of Day 33 and 34 of the Wangara data

The very complete set of boundary layer data, the Wangara data, taken and compiled by Clarke et al (1971) has been used in a number of ABL model simulations. Notable are the experiments carried out by Deardorff (1974a and b) and Yamada & Mellor (1975). Deardorff used a 3-dimensional model over a volume 5x5x2 km discretized by 64 000 gridpoints. Part of the turbulence field was treated explicitly part of it was treated as subgrid-scale motion. These 3-dimensional simulations have given considerable insight into ABL behaviour in unstable conditions. Yamada & Mellor (1975) used an one-dimensional boundary layer model with a simplified second order closure scheme as turbulence parameterization. They simulated three days of the Wangara data, Day 33, 34 and 35, both day and night. They also went into considerable details in extracting the time and vertical variation of the geostrophic wind and the mean vertical velocity from the observations. From the thermal wind relation they also determined the horizontal temperature advection. Because of these and similar studies it is of considerable interest to try to simulate the same data with the present model. Another reason is that we, at the present time, are lacking detailed data from more northerly latitudes, e g Scandinavia, which can be used for model validation.

The Wangara data (Wangara meaning "west wind" in the language of the aborigines) were taken at a place called Hay in a flat, semi-arid region in south-eastern Australia. The observational campaign lasted 40 days centered around August 1967. Pilot balloons were released every hour from 5 points and radiosondes for temperature and moisture measurements every third hour. Some micrometeorological observations were also carried out. All of this is documented by Clarke et al (1971).

The location chosen for the measurements come close to the ideal place as far as horizontal homogeneity is concerned.

7.1 Initial and background data

The initial data, used in the simulations described below, are from 0900 local time of Day 33 (August 16) of the Wangara data. The profiles shown in fig 10 have been slightly smoothed and are interpolated logarithmically between 50 m and the ground.

The background values for u, v, T and q have been extracted from the observed values at 2000 m. Fig 11 shows the time variation of u and v at 2000 m, surface geostrophic wind and the mean geostrophic wind in the layer between the ground and 2000 m. The background wind is assumed constant with height, i e baroclinicity is neglected in the simulations.

Temperature at 2000 m only varies with about $\pm 0.5^{\circ}C$ during the ensuing 24 hours and is assumed constant, which is also true for the specific humidity which is set at 0.7 g/kg at 2000 m.

Hay is located at $34.5^{\circ}S$ which gives a corresponding value for the Coriolis parameter of $0.826 \cdot 10^{-4} s^{-1}$. Surface roughness was estimated to be an average 0.01 m for the 5 stations involved. Pressure at 2000 m was kept constant at 798 mbs.

These initial and background data have been used in a number of experiments to study different aspects of the model.

7.2 First experiment
Prescribed surface temperatures

In this simulation surface temperature was prescribed. The 1.2 m screen temperature was used to calculate a surface temperature by means of Monin-Obukhov's similarity theory.

The Wangara data also contain information about wind speed at 0.5, 1, 2, 4, 8 and 16 meters height and temperature differences between 2 and 1 meters and 4 and 2 meters. This makes it possible to evaluate u_* and the Monin-Obukhov length L from which surface temperature, T_o, can be determined by using the Businger et al (1971) flux-profile relations for the universal functions ϕ_m and ϕ_h. This also gives the possibility of comparing computed stresses and heat fluxes at the surface with "observed" ones. Fig 12 shows the computed surface temperature used in the first experiment in which radiation and large scale vertical velocity were neglected.

In this experiment the impact of different formulations of the mixing length during the night was studied. The basic results are shown in figs 13, 14 and 15, showing the simulated time-height variation of the u-component of the wind, potential temperature profiles during the day and two nocturnal profiles at night. Observed values of temperature are also shown. The nocturnal profiles are only shown up to 250 m above which the model is incapable of predicting any changes because of the neglection of radiation and vertical velocity.

7.2.1 Day-time temperature prediction

During the day potential temperature is well predicted. Fig 13 shows a well mixed ABL that is growing in depth during the day. Verification temperature profiles in fig 20b show that the growth of the ABL is well predicted. The potential temperature profiles slope slightly to the right, i e slightly stable conditions persist above the unstable lowest 100-200 m. This is a result of the counter-gradient term.

Another feature of the potential temperature profiles is the "overshoot" of the profiles in relation to the initial one.

It shows that turbulent mixing occurs in the stable layer capping the well mixed layer. The ability to simulate this well documented feature of the unstable ABL is because of the inclusion of the vertical diffusion term in the turbulent energy equation, eq (41). It is interesting to note, however, that excluding this term (as is done in usual K-formulations) also affects the total heating and the surface heat flux. Neglecting the counter-gradient term only affects the heat flux in the morning when the ABL is shallow. This is illustrated in figs 15 and 16, which show Θ-profiles and surface heat flux in the two cases $\frac{\partial}{\partial z}(K_m \frac{\partial b}{\partial z}) \equiv 0$ and $\gamma_{cg} \equiv 0$. In the former case the height of the ABL is not only much lower but the mean temperature in the ABL is about $1^{\circ}C$ less than the "normal run" in the afternoon. $\gamma_{cg} \equiv 0$ only makes minor changes to the Θ-profiles. In the case $\frac{\partial}{\partial z}(K_m \frac{\partial b}{\partial z}) \equiv 0$ surface heat flux is considerably reduced as shown in fig 18 while only a minor reduction is present in the morning when $\gamma_{cg} \equiv 0$ (during the time when it is usually largest).

7.2.2 Nocturnal temperature profiles

Predicted and observed nocturnal temperature profiles at midnight and 0600 in the morning of Day 34 are shown in fig 14. Two cases are shown, one using the basic mixing length formulation in eq (57) and the other using Delage's formulation, eq (53). This figure illustrates very clearly the inability of Delage's mixing length formulation to correctly simulate the growth of the thickness of the nocturnal ABL. The absence of radiation, however, also restricts the growth of the ABL in case one. The difference between the two formulations, however, is considerable. In Delage's formulation the ABL only grows up to about 50 m while in the present formulation the top of the inversion is at about 125 m. After 21 hours of integration the difference between the simulation and observations is less than $1/2^{\circ}C$ up to 100 m, above which the neglection of radiation becomes critical.

7.2.3 Wind simulation

The wind simulation will be illustrated with the u-component of the wind shown in a time-height cross section in fig 17. The observed variation is shown in the lower part of the figure. The two dominating features of the diurnal cycle are well predicted. During day time well mixed ABL, weak winds persist most of the time with a speed varying between 1-2 m/s. After sunset the wind speed starts to increase at practically all levels and at 0530 in the morning of day 34 a wind maximum of 11.1 m/s at a height of 350 m develops in the model simulation.

The maximum is, however, quite broad in the vertical. Observations indicate a similar development of a nocturnal jet. The observed maximum, amounting to 12.8 m/s occurs, however, at 0300 at a height of 200 m.

The nocturnal jet

The formation of wind maxima of this kind was discussed by Blackadar (1957) who gave a simple explanation of the phenomenon. More recently Thorpe & Guymer (1977) have studied the same phenomenon by means of a simple 2-layer model applied to the Wangara data as well as data from southern England.

The main mechanism in creating this nocturnal wind maximum, which usually exhibits a wind which is strongly supergeostrophic with a factor of 1.5, is an inertial oscillation. In stationary large scale conditions the strong turbulent mixing during the day creates cross-isobaric flow extending up to the top of the ABL. At sunset the whole boundary layer collapses and turbulence rapidly dies out at levels above the lowest 50-100 m. The bulk of the previously mixed layer suddenly becomes the "free", non-turbulent, atmosphere. The wind is, however, unbalanced and an adjustment starts as an inertial oscillation. The period of the oscillation, $T = 2\Pi/f$, is about 21 hours at the latitude of Hay and about 12.5 hours in the middle parts of Sweden. The maximum occurs after about 9 hours after the surface energy balance has resulted in a stable layer close to the ground.

In the case of Day 33 of the Wangara data the unstable ABL collapses at about 1700 LT. The maximum would then occur around 0200 which is close to the observed time.

In the model, however, the maximum occurs around 0530, which is about 2 1/2 hours too late. The time of the maximum is probably also influenced by baroclinicity and variations of the geostrophic wind which is not constant during this period. Furthermore the present model uses observed winds at 2000 m as boundary values instead of geostrophic wind. As shown in fig 11 the observed winds are far from being geostrophic and the u-component has a marked maximum around 0600 LT.

Other models have also been used in simulating the Wangara data. Yu (1976), also using the turbulent energy equation but a usual Ekman formulation of the equations of motions, got his wind maximum occurring a little before midnight instead (see section 7.4.2 for further discussion). Yamada & Mellor (1975) predicted its occurrence at about 0130, only 1 1/2 hour before the main maximum. Their model also takes into account baroclinicity, i e the vertical variation of the geostrophic wind, and vertical advections.

There is still another interesting feature of the wind variation. After the maximum wind has been reached, wind speed decreases much more rapidly at upper levels than at lower levels in contrast to the increase in wind speed which seems to take place at the same rate at all levels up to the mixed layer height during the afternoon. This produces a bell shaped tapering off of the maximum with strong wind shears both above and below the wind maximum. The final break down of the nocturnal jet comes when convection reaches the height of the jet.

Because the simulated maximum occurs so late this phenomenon has no time to develop.

7.3 Second experiment: Full model simulation

In this series of experiments the full model has been used, i e including radiation computations and vertical velocity. In the first part the model has been run in its basic Gutman-formulation while in the second part the momentum equations have been modified to conform to a model using the ordinary unsteady, horizontally homogeneous Ekman boundary layer equations (Ekman version) as used by for example Yamada & Mellor (1975), Yu (1976) and Delage (1974). This is done to allow a direct comparison between the Gutman version and the Ekman version and results by other authors.

7.3.1 Initialization, radiation and vertical velocity

In the full model simulation by the Gutman version the same background values for u, v, T and q as in the prescribed surface temperature experiment have been used. The previously computed surface temperature at 0900 LT has been used as initial surface temperature. Turbulent energy is calculated diagnostically from the steady state turbulent energy equation neglecting the diffusion term.

The radiation computations require a down-ward flux at the upper most level and which is set to 90 w/m^2 corresponding to the energy radiated from a black surface of temperature 200 K. In order to conform to the upper boundary condition cooling rates are only calculated up to 1300 m above which they are linearly decreasing to zero.

The vertical velocities are not the original ones. Instead the vertical velocity in the upper kilometer (1-2 km) has been smoothed in time and space and referred to the top of the model at 2000 m.

The vertical velocity is assumed to vary linearly from its 2000 m value to zero at the ground and interpolated between hourly values for each time step.

The following table shows the vertical velocity used at 2000 m.

Table 1
Vertical velocities at 2000 m (in cm/s)

Time	09	10	11	12	13	14	15	16	17	18	19	20	21	22
w	-1.0	-3.4	-1.0	+1.0	+1.5	-3.0	-3.5	-3.7	-2.7	-1.8	-3.0	±0	-0.3	0

Time	23	24	01	02	03	04	05	06	07	08	09
w	0	+2.0	0	0	-0.8	-1.5	0	0	0	+3.0	+2.0

It is worth remembering that the estimated error in the measured vertical velocitites is of the order ±2 cm/s!

7.3.2 Wind simulation

The evolution of the u- and v-components in the full model simulation was found to be very similar to the prescribed surface temperature simulation. The nocturnal maximum is occurring just before 0600 LT with a value close to 11 m/s. Here is instead shown the time-height variation of wind speed, which is a composite of the variation of the u- and v-component (see fig 18). Since wind speed in this case is dominated by variation of the u-component also in this case the maximum is occurring at 0600 LT, while the wind speed maximum is observed at 0245.

7.3.3 Temperature prediction

The temperature prediction is naturally changed by the inclusion of radiative temperature changes and vertical advection as compared to the previous paragraph. Fig 19 (a,b) shows the observed and predicted time-height cross sections of temperature.

Temperature is dominated by the strong heating during the day in the growing, unstable ABL and the radiational cooling and turbulent heat flux close to the ground during the night. These features are well simulated by the model. The vertical velocity creates warming and cooling in the upper 1 km of the model. Consequently the inversion rises and sinks. In lower layers turbulence is the dominating term in the thermodynamic equation while during the night radiational cooling is strong enough to offset the warming of subsidence. This is also primarily because the lapse rate was left close to the dry adiabatic one making the vertical advection term $w(\frac{\partial T}{\partial z} + \Gamma_d)$ very small below the inversion. The warming between 18 and 21 at 1500 m seems to be exaggerated in the model simulation.

The growth of the nocturnal inversion is well depicted. The mixed layer depth during night is impossible to assess from the observations. The surface inversion height as a measure of boundary layer height is on the other hand possible to use for comparison. Both observations and prediction show a growth of the inversion height ending up at about 300 m. The observations also show a sudden lifting of the top of the inversion between 0300 and 0600 which is difficult to explain by radiational cooling and turbulent heat exchange. A more probable explanation is the presence of horizontal advection which also explains the general warming occurring through a deeper layer between 22 and 04.

Figs 20 and 21 further illustrate the behaviour of the daytime and nocturnal thermal boundary layer. Fig 20 shows predicted and observed potential temperature profiles at times 12, 15 and 18, where potential temperature is defined as

$$\theta = T(\frac{p_o}{p})^{\kappa} \qquad \kappa = R_d/c_p$$

$p_o = 1000$ mb

The evolution of the convective boundary layer is very well depicted by the model. The predicted mixed layer temperatures are all within 1/2°C from the observed ones. The temperature profiles are slightly tilted towards the right because of the countergradient heat flux term while this slight increase of temperature with height is only present in the observed profiles at 12 o'clock.

The growth of the mixed layer is the result of heating and erosion of the inversion by turbulent, thermal plumes and the large scale vertical velocity in the inversion region. The mixed layer depth is also very well predicted even if the height of the capping inversion at 15 o'clock is about 150 m too high.

Figs 21a and b show predicted and observed nocturnal temperature profiles at times 18, 00, 06 and 09 plotted in log-linear height scale (grid-point plotting) to resolve the variation in the lowest 200-300 m.

Fig 21a shows that quite rapid cooling takes place below 50 m. During the rest of the night turbulent mixing is increasing and the top of the surface inversion is rising. At 0600 it has reached 250 m. At 9 o'clock a convective ABL has already formed extending up to about 80 m.

Looking at the observations they verify very well for the 18 and 00 profiles. At 06 o'clock substantial cooling has taken place above 100 m and the top of the inversion is actually at about 500 m. This cooling seems impossible to explain by radiational and turbulent cooling solely. Between 1 m and 100 m the prediction is quite good. Observations also show a very sharply peaked inversion at 1100 m, which, if it is the result of subsidence, indicates very strong sinking motion.

This sinking motion is not present in the vertical velocities used in the simulation.

The observed profile at 9 o'clock, day 34, is looking somewhat strange with constant temperature between 1.2 and 50 m while the prediction shows an unstable layer up to about 100 m. This discrepency between observation and prediction is difficult to explain. The 1.2 m temperatures, however, only differ by 1/2 a degree.

7.3.4 Turbulence properties

The primary goal with the present model is not to predict the detailed turbulent structure of the ABL but is focused on the prediction of the averaged meteorological variables like wind, temperature and moisture. The turbulent energy equation is used to supply consistent eddy diffusivities for the momentum equations, the thermodynamic equation and the moisture conservation equation. It is, however, of some interest to study the turbulent energy and the balance of the turbulent energy budget, i e distribution through the ABL of the different terms in the turbulent energy equation. It is also possible in this way to detect and correct inconsistencies in the parameterization.

The results concerning the turbulent properties are shown in figs 22 through 24. Figs 22 show time-height cross sections of turbulent energy, as defined by eq (36),and the mixing length used by the model.

In fig 22a the growth of the convective ABL is well reflected by the increase of turbulent energy up to a maximum at about 1 o'clock pm occurring at a height about 200 m. Isopleth values are scaled with a factor of 100, maximum value being 3.1 J/kg. The correctness of the predicted values is difficult to assess. Comparison with Yamada & Mellor (1975) shows a larger maximum value than they obtained for day 33.

This might, however, depend on the fact that the present model simulation predicts weaker winds during the day than the Yamada & Mellor (Y&M) simulation making the model closer to free convection condition with enhanced turbulent energy. The height at the maximum is about the same. Deardorff (1974b) presents results for the vertical velocity variance (the variance of the horizontal components of the wind is more constant with height) which show a maximum at a height of around 3/10 of the ABL-height, which corresponds to 300 m with a boundary layer depth of 1000 m. This is also in agreement with Kaimal et al (1976) and Wyngaard et al (1974).

The graph also shows the rapid collapse of the unstable ABL occurring after the heat flux at the surface has turned negative. The night time values are more than one order of magnitude less than the convective ones.

Fig 22b shows the mixing length calculated according the formulas (57) and (58). During the day large values are obtained in the middle of the mixed layer in accordance with Deardorff (1974a). The maximum is about 600 m at 600 m height. During the night the limiting value is about 50 m. The large mixing length and turbulent energy values during the day lead to maximum eddy diffusivities of the order of 400 m^2/s. This does not seem unreasonable in conditions with strong heating and weak winds.

Fig 23 shows the turbulent energy budget by means of a direct evaluation of the terms in the turbulent energy equation, i e the vertical distribution of the shear generation, bouyancy generation, diffusion and dissipation terms. a) shows the balance at 12 o'clock while b) shows nocturnal conditions at 3 o'clock in the morning of day 34. Values in m^2/s^3 are multiplied by a factor of 1000 for convenience.

At 12 o'clock on day 33 the height of the mixed layer is 950 m. The bouyancy generation term, proportional to the kinematic heat flux, is the dominating one in the bulk of the ABL. Its profile shape indicates a 50-100 m thick constant flux layer. Above this height the bouyancy term is decreasing almost linearly to a minimum value at 950. This means that turbulence is generated through the bulk of the ABL. It is only at the top turbulence is destroyed, or consumed by bouyancy. The physical reason for the latter is the existence of turbulence in the stable layer right above the mixed layer (see sect 3.3). This turbulence is the result of a redistribution of turbulent energy due to the action of vertical velocity, turbulent energy and pressure correlations, represented by the diffusion term in the turbulent energy equation.

This term is negative in the middle parts of the ABL and positive in the upper 1/3 of the PBL and at the very bottom. This shows that turbulence is exported from the middle parts of the ABL and imported in the upper parts.

Energy dissipation has its maximum at the surface and declines rapidly to a more or less constant value through the bulk of the ABL. Shear production of turbulence is significant only in the lowest 5 m of the convective ABL.

The turbulent energy budget predicted by this simplified turbulence model is well supported by observations and other, 3-dimensional, simulations.

The constancy of the dissipation term and the linear decrease of bouyancy (heat flux) is documented in e g Kaimal et al (1976). In this paper observations show dissipation rates about half the surface value of the bouyancy term. In the present simulation the dissipation rate is somewhat less, but coinciding with dissipation rates predicted by Deardorff (1974b).

On the other hand Yamada & Mellor (1975) get a linearly decreasing dissipation rate with height which is not supported by observations and values seem too high. In their case dissipation is almost completely balanced by bouyancy due to diffusion being very close to zero.

The profile of diffusion can be compared with Deardorff's (1974b) results showing that the predicted shape and magnitude is very similar to his results with negative values in the middle parts and positive in other parts of the ABL. The predicted energy balance is also consistent with Lenschow's (1970) aircraft measurements.

The ratio of the maximum downward heat flux at the top of the PBL to its surface value is about 20% but varies during day between 10% to 50%. This shows that the model is capable of predicting this overshoot behaviour of potential temperature found by many authors. The Yamada & Mellor (1975) model on the other hand predicts much too small values for this ratio (of the order of 1-5%).

Yu (1976) also used the turbulent energy equation in an one-dimensional model simulation of day 33 and 34 of the Wangara data but failed to predict these characteristics of the turbulent energy budget discussed here.

Fig 23b shows the corresponding terms in the turbulent energy equation at 3 o'clock in morning of day 34. Similar observations as in the unstable case are not available for the nocturnal PBL. From a physical point of view, however, the predicted energy balance does not look unreasonable. The two dominating terms are shear production and bouyancy destruction of turbulent energy while dissipation is significant only close to the surface where it balances the shear production.

The diffusion term indicates an export of turbulent energy from the surface layer to higher levels. The heat flux profile also shows a constant flux layer extending up to about 50 m, which seems to be extremely shallow in Yamada & Mellor's (1975) simulation.

The results show that the simplified version of the turbulent energy equation, with a proper choice of a mixing length, can simulate the basic properties of the overall turbulent energy budget in the unstable ABL and does not look unreasonable in the stable ABL.

Fig 24 will end our discussion of the turbulent properties of the model. The picture shows a time-height cross section of kinematic heat flux. Upward heat flux is extending higher and higher up from 9 through 14 o'clock after which the zero line actually goes down*. This behaviour is not exactly what has been predicted by other authors but might be the result of the interaction between subsidence and the counter-gradient heat flux term, which is decreasing with time due to the increase in boundary layer height and decrease in surface heat flux. This also means that downward heat flux exists in a deeper layer in the afternoon, after the maximum surface heat flux has occurred than before heat flux maximum.

During the night the heat flux is small but increases with time as the depth of the ABL grows and turbulence intensity increases due to enhanced shear production following the formation of the nocturnal jet.

7.4 Ekman-version simulations and comparison with the Gutman-version

The boundary layer model, using the Gutman-approach, presupposes background values predicted by another, primitive equations, model.

*) This does not happen in the Ekman-version discussed below.

Problems arise when observed values for wind, temperature and moisture have to be used. Comparisons with other studies and observations show that the wind maximum is predicted to occur about 2 1/2 hours too late while the temperature prediction is very good. It is therefore of considerable interest to compare the present Gutman simulation with a more conventional formulation of the momentum equations. It is also desirable to be able to compare with other simulations, i e in particular with Yamada & Mellor's very extensive simulation of the Wangara data.

For this end the model has been modified so to conform with the ordinary, horizontally homogeneous, unsteady momentum equations used by most one-dimensional ABL-models - hereafter called the Ekman version. The thermodynamic, moisture and turbulent energy equations have been left unchanged.

The Ekman version has been run with three different specifications of the geostrophic wind

1. Constant geostrophic wind from the surface to 2000 m equal to the average geostrophic wind. Varying in time.

2. Constant shear through the PBL making the surface geostrophic wind and the geostrophic wind at 2000 m coincide with observations.

3. Exactly the same geostrophic wind as used by Yamada & Mellor (1975).

In this paragraph we will focus on experiments 1 and 3. The former to allow a direct comparison between the Gutman and the Ekman version (no one including a shear in the background or geostrophic wind) and the latter to allow a direct comparison with Yamada & Mellor (1975).

7.4.1 Modifications for the Ekman version

The same programme code has been possible to use with the minor addition of the terms fv_g and $-fu_g$ in eqs (30) and (31) and changing the meaning of u' and v' to denote the total, ordinary wind. The initial wind profiles have been modified at the top to conform to the boundary conditions used in this case.

$$z = 0: \quad u = v = 0$$
$$z = 2000 \text{ m}: \quad u = u_g, \quad v = v_g$$

The variation of the mean geostrophic wind and the surface geostrophic wind in time is shown in fig 11 while the geostrophic wind used in the Yamada & Mellor comparison is shown in Yamada & Mellor (1975), fig 5.

The rest of the model is exactly the same as in the Gutman case.

7.4.2 Wind simulation, no shear case

In this case the average geostrophic wind in the layer 0-2000 m has been used to allow direct comparisons with the Gutman simulation.

Figs 25-28 show the results of this comparison. Fig 25 shows the predicted time-height variation of windspeed. The most striking change as compared to the Gutman version is the displacement of the wind maximum from around 6 o'clock in morning to about 20 minutes to 2. This is actually an improvement. This time is only about one hour off the observed time for the wind speed maximum.

Another feature is that wind speed is somewhat higher during the day and the inertial oscillation seems to start somewhat earlier in this case than in the Gutman case.

The absence of geostrophic shear makes the isotachs vertical during the inertial oscillation phase, i e it istaking place at the same rate at all levels in the previously mixed layer.

In fig 26 are plotted u- and v-components of wind at 250 m and 450 m from observations (full lines) and predictions, where dash-dotted lines shows Gutman-version, dashed lines Ekman-version without shear and dotted lines Ekman-version with constant shear. The picture shows that the u-component of the wind is very well predicted by the Ekman-version up to about 1 o'clock am, after which the observed wind suddenly increases to a second maximum around 3 o'clock. The v-component is overpredicted by about 2 m/s during the day while during the night it follows very well the observed evolution.

The Gutman-version on the other hand starts off like the Ekman-version but around 13 o'clock departs from the observed evolution. The whole inertial oscillation phase seems to be shifted in time with the maximum u-wind occurring at 6 o'clock in the morning. The v-component stays negative up to 15 o'clock while observed values and the Ekman-versions show positive v-components. Also here there is a phase shift. The background v-component (fig 11) is negative all day. The reason for this behaviour could be errors in the observed 2000 m wind, but a more likely explanation could be the use of observed background values inconsistent with the definition of background quantities as given by eqs (18)-(23), i e predicted by a LFM. Comparing with observations the Ekman-versions definitely perform better than the Gutman version.

The observed variation of the wind after midnight is very interesting. Up to midnight the predicted and observed values have followed each other extremely closely and a first maximum is occurring exactly at the same time.

After midnight there is a sudden increase in u- but a decrease in the v-component. This means a change in wind direction more than an increase in u. This sudden change looks strange and is difficult to explain in terms of an inertial oscillation. Horizontal advection is a more probable explanation. The same general evolution is maintained also at 450 m where the sudden maximum looks even more off the regular change due to the inertial oscillation. The fact that the present model predicts a maximum at midnight instead of at 3 o'clock should then not necessarily be taken as a deficiency of model.

In their simulation Yamada & Mellor get the maximum of the u-component at about 0130 LT which is closer to the observed maximum but further away from the first midnight maximum. When comparing their results with the present results there is one important difference that should be pointed out. The starting time for the inertial oscillation, which is important for the time of the jet maximum, can be taken as the time when the well mixed unstable boundary layer collapses, i e when the surface energy balance changes so that the surface heat flux changes from positive (upward) to negative (downward). If this time is changed the time for the maximum is also changed. This time occurs in the present model slightly before 1700 hours but in Yamada & Mellor's simulation about an hour later. The reason for this is that in the present model the surface temperature is calculated explicitly from eq (65) while Yamada & Mellor are using prescribed (observed) temperatures at 1.2 m and the temperature difference between 1-2 m to calculate a lower boundary condition. This temperature difference is positive at 1700 hours indicating unstable conditions (when the heat flux at the ground already may have turned negative) and negative at 1800 hours. The effect of this can be seen in their fig 17 where the collapse and change of surface heat flux takes place close to 1800 hours.

This might be an explanation of why their wind maximum is occurring about an hour later than in the present model. Adding an hour to the present time of the maximum u-component makes the difference only half an hour between the two cases.

7.4.3 Temperature simulation, no shear case

The simulated temperature during the day by the Ekman version of the model is almost exactly coinciding with temperature predicted by the Gutman-version. This can be seen in fig 12 where, in addition to the derived surface temperature from observations, is also shown the predicted surface temperature by the two versions. It is only after 1800 hours they start to diverge, the Ekman-version being about 1^{o} warmer than the Gutman case. However, they are both ending up at the same surface temperature right before sunrise which is coinciding with the one derived from observed temperatures at 1.2 m. The reduced cooling rate during the first 7-8 hours after 18 o'clock can be explained by the increase in mixing and downward heat flux resulting from the stronger winds and earlier occurrence of the wind maximum in the Ekman case. After the wind maximum between 1-2 in the morning cooling rate increases again while the Gutman case shows strong cooling in the beginning of the night but almost constant surface temperature after midnight. Both, however, come close to "observations" with a maximum deviation of 2^{o}.

Fig 27, showing predicted temperature profiles during the night, also illustrates this different behaviour during the night. They are fairly similar at 18 o'clock even if the inversion top is somewhat higher in the Ekman case. The midnight profile is considerably warmer than the Gutman case and the top of the inversion is at 250 m instead of 140 m for the Gutman case. The resulting profiles at 6 and 9 o'clock on the other hand are quite similar.

7.4.4 Boundary layer height and friction velocity

Finally a comparison is made between the predicted and observed boundary layer height in fig 28. The boundary layer height during the day is picked out from the well mixed potential temperature profiles while during the night the top of the surface inversion is used as a measure of ABL height. Friction velocity, u_*, is computed from observations using the same procedure as for the previously presented surface temperatures. These are then not truly observed values but deduced values.

Fig 28a shows predicted and observed boundary layer height. As mentioned before both predictions overshoot the observed height at 1500 hours with about 150 m but ending up at 1800 hours at about the observed height. The evolution of the nocturnal ABL is somewhat different in the two cases. The Ekman-version predicts a more rapid initial growth of the inversion depth in accordance with the further increase in wind speed, faster even than the observations, while the Gutman case is quite good during most of the night except for the extraordinary cooling event around 6 o'clock in the morning when the predicted boundary layer height is too low in both cases. However, generally speaking both versions do a very good job in predicting the nocturnal ABL, which usually has been a problem in other models. For example both Delage (1974) and Yamada & Mellor (1975) underpredict the depth of the nocturnal boundary layer.

Fig 28b shows "observed" and predicted u_* as a function of time. u_* increases during day which is well predicted by the Ekman-version but missed entirely by the Gutman-version of the model. On the other hand the low values during the night are somewhat better predicted by the Gutman-version than the Ekman-version even if the increase in u_* in late night comes too early as compared to "observations".

The Ekman-version behaviour is very similar to the simulation by Yamada & Mellor (1975).

7.4.5 Relative merits of the two versions of the model

There is no doubt that looking at the wind predictions of the Wangara data, days 33 and 34, the Ekman-version of the model is superior to the Gutman one. The problems might arise because of the use of inconsistent background winds in the Gutman-version. The Gutman approach does not say anything explicitly about the scales of barred (eg $\bar{u}$) and primed (eg u') quantities. However, the definition of $\bar{u}$, $\bar{v}$, $\bar{T}$ and $\bar{q}$ by eqs (18)-(23), i e a LFM, implies certain length and time scales as exemplified in the scale analysis in chapter 2.5. In a LFM, with a grid distance of Δx, u', v', T' and q' refer to ABL properties on a scale smaller than Δx while $\bar{u}$, $\bar{v}$, $\bar{T}$ and $\bar{q}$ refer to scales larger than Δx. The observed values at 2000 m represent both large and small scale properties of the flow. Observed values are then inconsistent with the assumptions of the Gutman version. This aspect has to be tested when running the model coupled to a LFM supplying the background data, the situation for which the Gutman-version actually was derived. Temperature and moisture predictions (not shown in this report) show very little difference, probably because 2000 m values were practically constant, and from the observations during the night it is difficult to assess the relative merits.

The Ekman-version seems, however, to be preferable when simulating past data and certainly more consistent than the Gutman-version.

7.4.6 Simulation with Yamada & Mellor's geostrophic wind

We will end this chapter by showing some results from the Ekman-version using Yamada & Mellor's (1975) derived geostrophic winds using the reported shears in the two layers 0-1000 m and 1000-2000 m and the surface geostrophic wind.

Quadratic polynomials are used to interpolate vertically. Shears and surface geostrophic wind are interpolated linearly in time. The differences between the present model and Yamada & Mellor's lie in the turbulence parameterization, lower boundary condition for surface temperature (predicted versus prescribed), vertical velocities and the vertical resolution, Yamada & Mellor using 80 gridpoints contrasted to 35 in the present model between the ground and 2000 m.

Fig 29 shows the predicted u- and v-components of the wind and fig 30 potential temperature by the present model. These graphs should be compared with Yamada & Mellor (1975), figs 7, 8 and 9, where also the verification can be found. These figures can also be found in Bodin (1978).

Fig 29a shows the predicted u-component of wind. The day-time part of the prediction is not very different from the vertically constant geostrophic wind case. However, the nocturnal part is different. The maximum wind is taking place at 0020 and the u-maximum is 11.9 m/s where Y&M got 11.7 m/s. Adding one hour (see section 7.4.2) to this time gives us 0120, which is very close to the Y&M time of maximum u, 0130.

The decay of the wind maximum, however, is predicted differently in the two cases. Observations show a very well marked "bell shape" of the u-maximum with a much slower decrease of u at the level of its maximum than at higher levels (fig 17b). This leads to a zone of fairly strong vertical wind shear also above the wind maximum. This feature is very well predicted by the present model but to a less extent by Yamada & Mellor's.

The reason for this slower decay could be, in reality and in the present model, the interaction between the growing boundary layer and the jet maximum.

The slower decay at the level of the maximum of the u-component indicates that the rate of change is slower than that from the inertial oscillation present above. This can come about if the boundary layer grows sufficiently high during the night so to reach the level of maximum wind. In this case a turbulent stress term will again be introduced in the momentum equations thereby delaying the inertial oscillation. In the present model turbulent mixing reaches about 350 m in the early morning. By 6 o'clock the top of the surface inversion has only reached 150 m in Yamada & Mellor's simulation (see their fig 33). This does not allow any interaction between turbulent mixing and the inertial oscillation at the level of the wind maximum!

André et al (1978) also predict much too shallow a boundary layer during night resulting in a too low wind maximum and no "bell shaped" tapering off of the u-component.

It is also interesting to note that in the observations there is virtually no shear in the observed u-component above the wind maximum. This could indicate that the assumed geostrophic wind leading to a predicted shear above 300 m in the morning of day 34 is wrong.

Fig 29b shows the predicted v-component. Comparison with Yamada & Mellor's result shows that they are very similar except for the phase shift of the maximum of one hour in the late morning of day 34.

Finally fig 30 shows the predicted potential temperature. Comparison with Yamada & Mellor shows differences primarily during the night when the top of the inversion grows up to about 300 by 6 o'clock in this model but stays at about 150 m in the Y&M case. The present model prediction is more in agreement with observations.

The comparison of the Ekman-version of the model with Yamada & Mellor's simulation does not speak in favour of the latter. On the contrary, some features during the night are better predicted by this, more simplified, model. Also the turbulent energy balance seems to come out better in the present model and looks more like the results obtained by André et al (1978) in their third order turbulence closure model study of days 33 and 34 of the Wangara data. But also in this case the present simplified model performs better during the night.

The crux seems to be the mixing length formulation which makes it possible to use a simplified turbulence model during the day and still predict a basically correct turbulence energy balance.

8. Simulation of Hyrylä data

Most of the development work of the model has been done using the Wangara data, days 33 and 34, as test data. This data set is representing conditions on the southern hemisphere, in a semi-aride, flat area, at fairly low latitudes. Since the model is going to be applied at northerly latitudes in the northern hemisphere in a terrain different from that in Australia it is of considerable interest to test the model in an atmospheric environment close to our own. One of the problems is, however, that no good data set, of the same quality and extent as the Wangara data, exists for northerly latitudes. One way of solving this problem is to arrange an observational program, for example in Sweden. In October 1977 a pilot study was performed in the Östgöta Plain in the southern parts of Sweden. The boundary layer was observed for 48 continuous hours and the measurements included pibal ascents every third hour, surface layer measurements of mean temperature, wind and humidity, soil temperature and acoustic sounder monitoring of the ABL-height. In spring 1980 an extended experiment is planned.

8.1 Initial and background data

Awaiting the results from these experiments we have used some Finnish data to test the model. This data set, which was collected in 1972, is rather incomplete and a complete verification is not possible to make. The place Hyrylä is located about 25 km NNE of Helsinki. Surface measurements and balloon ascents took place on a fairly dry meadow with 20 cm high grass. There is open land out to a distance of 2 km where the forest starts. In the southwest there are some buildings about 500 m away and further soutwest there is a ridge about 60 m high. The wind direction during the days 5-6 June 1972 was predominantly southwesterly. Vertical soundings of temperature, humidity and wind speed and direction were available at 0800, 1400 hours local time on 5 June 1972 and 0800 on 6 June 1972 extending up to 2500 m. Data from 0800, 5 June 1972, were used as initial data and were interpolated to the model grid after some slight smoothing.

The background values for $\bar{u}$, $\bar{v}$, $\bar{T}$ and $\bar{q}$ were taken from the 2500 m values and supplemented with data from the regular soundings at Jokioinen located about 100 km northwest of Hyrylä. Vertical velocities at 2500 m were derived from the downward displacement of a well defined subsidence inversion present both in the Hyrylä data and in Jokioinen's temperature records. Soil parameters and roughness length were chosen as being representative of the surface and soil conditions reported by the Finnish Meteorological Institute. That gave z_o = 0.02 m, thermal diffusivity $0.5 \cdot 10^{-6}$ m^2/s, thermal conductivity 0.5 J/mKs. An albedo of 0.23 was used. In this prediction 40 grid points were used between the ground and 2500 m with a time step of 4 minutes.

8.2 Results

The 24 hour period from 8 o'clock on 5 June to 8 o'clock on 6 June 1972 was characterized by a fairly steady southwesterly flow over southern Finland and clear skies except for 1/8 of cumulus during the day and some scattered stratocumulus during the night. Above 2500 m no clouds were present. The night is very short at this time of year and the inertial period is only about 12 hours at latitude 60.3°N. Figures 31-37 show the results of the 24 hour simulation.

Fig 31 shows the predicted wind speed in a height-time cross section. During the day the model indicates rather well mixed conditions with a maximum at 1300 m. During the night the wind speed drops to about 5 m/s above the nocturnal ABL at the top of which a nocturnal "jet" develops at 250 m height at 0200 o'clock in the morning.

Figs 34a and b show predicted and observed profiles of u and v at 1400 hours, 5 June, and 0800 hours, 6 June. The wind prediction in this case is not as good as in the Wangara case. At 1400 hours the model overpredicts the wind in both the u- and v-components, especially at lower layers. An explanation to this could be the topographic influence of the upwind hills and buildings. Nappo (1977) has shown that even low hills have a marked effect on the wind profile especially in unstable and neutral stratification, while the effect is less in stable conditions. Up to 600-700 m there is a reduction in wind speed in hilly terrain by a factor of 2. This explanation is further supported by the fact that the synoptic station upwind of the hills reports a 10 m wind almost exactly coinciding with the predicted wind at 10 m during the afternoon. Similar behaviour, but to a less extent, is also seen in the u-component at 0800 hours. However, the v-component in the morning is better predicted than the u-component.

The wind prediction is difficult to evaluate also because of large errors in the pibal balloon measurements of the wind.

Fig 32 shows a time-height cross section of potential temperature. The picture shows very well the diurnal variation of temperature. During the day the heating extends to higher and higher levels because of the growth of the mixed layer. Surface temperature reaches a maximum of 24°C. Between 1800 and 1900 hours the energy balance switches sign at the surface and a stable layer is established close to the ground. Cooling goes on during the night resulting in a 300 m deep surface based inversion. The minimum temperature occurs around 0230, local time. A new unstable layer starts to grow around 5 o'clock in the morning.

Verifying temperature profiles are available at 1400 hours, 5 June and 0800, 6 June, i e at the end of the forecast period. Fig 35 shows predicted and observed vertical profiles of temperature. At 2 o'clock the predicted values agree with observations within 1°C and after 24 hours of simulation within 2°C except at the bottom of the subsidence inversion. One can also see the downward movement of the subsidence inversion. The mixed layer, however, does not reach up to the subsidence inversion.

Figs 33 and 36 show some other aspects of the model predictions. Fig 33 is time-height plot of turbulent energy. This picture illustrates very clearly the two distinctly different phases of the diurnal cycle. During the day the mixed layer grows up to a height of about 1500 m.

Turbulent energy reaches a maximum at about 250 m because of bouyancy generation, which is in general agreement with mixed layer observations or simulations, even if the maximum is a little too low.

Between 5 and 6 pm the unstable boundary layer is replaced by a shallow stable layer. Turbulence is now formed by shear generation and the maximum is found close to the surface with an almost linear decrease up to the top of the nocturnal ABL. Intensities are 1-2 orders of magnitude less than in the unstable ABL.

Fig 36, the kinematic heat flux, is also in agreement with what would be expected. During the day heat flux decreases almost linearly up to the top of the mixed layer where it becomes slightly negative as in the Wangara data case. The magnitude of this downward heat flux is about 10-20% of the surface heat flux in agreement with what is usually assumed. The night time heat fluxes are small and directed downward.

Some conclusions can be drawn from this experiment.

The wind prediction errors could be explained by topographical influences. Another reason could be the use of the Gutman version in this simulation as evidenced by the Wangara data simulation. A factor speaking against this, however, is the fact that the day time simulations of the Wangara data do not differ significantly between the Gutman and the Ekman versions. The errors in the Hyrylä simulations are largest during the day. It seems that one should be careful when interpreting one-dimensional model predictions to particular places, where even low topography can have a great impact on the local wind, especially in unstable conditions.

Temperature in this prediction did not show the same sensitivity to topographical influences. Karlsson & Aspling (1977) on the other hand noticed considerable deviations between observed and predicted values of temperature in an one-dimensional model study of data from Barkarby north of Stockholm. They attributed these errors to the local topographic conditions, which favoured cold air drainage during the night.

9. Conclusions and future work

Numerical modeling for operational applications means compromising between computer time limitations and dynamical, physical and numerical accuracy. In this way one is forced to find the best solutions - to the lowest cost. It means that many ways open to the experimental modeler are closed to the applied numerical modeler.

From many points of view "higher order" closure schemes seem to be the most logical approach to turbulence closure, even if they make use of a number of assumptions and constants, that have to be determined from observations. However, such closures lead to the order of 15 additional equations to be solved. This gives rise to unrealistic computer demands in most applications.

The use of simplier, but more economical, parameterizations necessarily leads to semi-empirical closure assumptions, that have to be tested in terms of generality, validity and applicability. This is certainly true in the development of the present model. Numerical modeling in this sense is very much a patch work. The benefits, however, are substantial.

9.1

The results of the present model, presented in this report, show that the diurnal cycle of the ABL can be well predicted in fairly calm, large scale, conditions. The basic turbulence parameterization used in the present model has shown considerable advantages and seems to be able to simulate the basic diffusive properties of atmospheric turbulence as well as more complicated closure schemes - to a much lower computational cost.

The Gutman formulation did not show any superiority over the more conventional Ekman formulation of an unsteady, horizontally homogeneous ABL.

This was partly expected because of the use of observed data as background data and the small variations in geostrophic wind.

These and other simulations of the Wangara data show that even over very flat terrain horizontal advections might be of importance. In general, however, the agreement between observed and predicted evolution of the ABL is good. In hilly or rough terrain wind seems to be the variable mostly affected, sometimes showing large deviations from observations. The influence on temperature is rather small provided that the observation site is not affected by cold air drainage during the night.

Modeling the unstable, convectively growing ABL, is nowadays not a difficult problem. Even very simple models can predict mean potential temperature and the mixed layer height with high accuracy. The day time evolution is also very well handled by the model. The advance has been in the prediction of the nocturnal ABL. Previous models have usually underpredicted the height of the nocturnal inversion. This was true in Delage (1974) but also in Yamada & Mellor (1975) and André et al (1978). The present formulation of the mixing length together with the turbulent energy equation seems to give quite satisfactory results. This further seems to be important in predicting the later stages of the nocturnal jet.

9.2 The model is intended to be used operationally at some airports in Sweden. It means that it must be able to cope with changes in the large scale flow in which clouds in the troposphere affect the boundary layer. One of the objectives with the model is to predict fog conditions and stratus clouds. Provisions for condensation and cloud formation have been made in the model but have not been tested. Some improvements of radiation computations when fog droplets are present should be made following Brown & Roach (1976).

These aspects of the model will be tested and developed using data from fog cases of the Wangara data and measurements made in Sweden in October 1977.

The data available as initial and background values in an operational context will not have the same quality as the Wangara data. It is planned to start daily predictions based on radiosoundings from Bromma Airport, local surface data for Arlanda Airport and background values from the balanced forecast model used at SMHI to test the predictive power of the model in the beginning of June 1979. In this context we will try to assess what sort of initial data is needed to produce meaningful forecasts by successively degrade data taken from the Wangara data. Procedures for making the interpolation to model gridpoints will also be investigated.

This is only the first step towards the development of a three-dimensional boundary layer model, a work which has already started. At the present time also a two-dimensional model, based on the same closure as here, is available at SMHI.

Acknowledgements

I am indebted to many people for discussions, ideas and useful comments. However, I would especially like to mention Prof Ingemar Holmström, who continuously has shown a great interest in my work, Prof L N Gutman, who triggered off my initiative in PBL-modeling and Dr J Deardorff for suggesting the present form of the unstable mixing length and many illuminating discussions.

A major part of the development work was carried out while I was on a scientific exchange with the National Meteorological Center, Washington D C. I would like to thank Dr John Brown Jr, Dr J Gerrity and the rest of the staff of Development Division for their very kind assistance and for creating such good working conditions. This is also true for the shorter time I spent at TDL, Silver Spring, Md.

I would also like to thank Mrs Pia Bremer and the Finnish Meteorological Institute for their kind cooperation in making the Hyrylä data available to me.

Finally I would like to thank Mr Kjell Ericson and Mr José Melgarejo for programming help and many discussions. Mrs K Fabiansen has typed the manuscript and Mrs W Böhm drawn the figures. Their superb work is gratefully acknowledged.

APPENDIX I

Derivation of TE-equation for saturated conditions

We will start by assuming that in the turbulent energy equation only the vertical component will change as a result of a change in bouyancy, i e $\frac{1}{2}\overline{w'^2}$

The second assumption will be that saturation static energy

$$E_s = c_p T + gz + Lq_s \qquad (I.1)$$

is conserved in turbulent mixing. This is equivalent to the assumption made in section 2.2.

Following Monin & Yaglom (1971) we can derive the prognostic equation for $\overline{w'^2}$ according to

$$\frac{1}{2}\frac{\partial}{\partial t}(\overline{w'^2}) + \frac{1}{2}\frac{\partial}{\partial z}(\overline{w'w'^2}) + \frac{1}{\rho_s}\left(\overline{w'\frac{\partial p''}{\partial z}}\right) =$$

$$= g\beta\overline{\theta'w'} - \varepsilon_w \qquad (I.2)$$

where we have assumed that temperature, T, is decomposed into

$$T = T_s + T' \qquad (I.3)$$

where T_s is a hydrostatic component following a hydrostatic pressure and density distribution p_s and ρ_s.

The non-hydrostatic part is further decomposed into averages and turbulent deviations from these, i e

$$T' = T'_o + \theta'$$

$$p' = p'_o + p'' \qquad (I.4)$$

We now assume a flux-gradient relation for $-\overline{\theta' w'}$

$$-g\beta\,\overline{w'\theta'} = g\beta K_H \frac{\partial T_o'}{\partial z} = g\beta\, K_H \frac{\partial \overline{T'}}{\partial z} \qquad \text{(I.5)}$$

Furthermore we have from (I.1) that

$$\frac{dT_s}{dz} = -\frac{g}{c_p} - \frac{L}{c_p}\frac{dq_s}{dz} \qquad \text{(I.6)}$$

and from (I.3) that

$$\frac{\partial \overline{T'}}{\partial z} = \frac{\partial \overline{T}}{\partial z} - \frac{d\overline{T}_s}{dz} \qquad \text{(I.7)}$$

which gives

$$g\beta\, K_H \frac{\partial \overline{T'}}{\partial z} = g\beta\, K_H\left(\frac{\partial \overline{T}}{\partial z} + \frac{g}{c_p} + \frac{L}{c_p}\frac{d\overline{q_s}}{dz}\right) \qquad \text{(I.8)}$$

Substituting this into (I.2) and adding this equation to the equations for $\overline{u'^2}$ and $\overline{v'^2}$ and using the other closure assumptions give eq (41) for horizontally homogeneous flow.

APPENDIX II

Details of numerical solution

1. Grid transformation

From the grid transformation, eq (98), $\frac{\partial \xi}{\partial z}$ is computed for every grid point in the basic grid valid for u, v, T and q and in the shifted grid, valid for b. All second order derivatives, i e diffusion terms, are transformed according to

$$\frac{\partial}{\partial z}(K \frac{\partial \alpha}{\partial z}) = \frac{\partial \xi}{\partial z} \cdot \frac{\partial}{\partial \xi}(\frac{\partial \xi}{\partial z} K \frac{\partial \alpha}{\partial \xi}) \qquad \text{(II.1)}$$

while first order derivative simply transforms into

$$\frac{\partial \alpha}{\partial z} = \frac{\partial \alpha}{\partial \xi} \cdot \frac{\partial \xi}{\partial z} \qquad \text{(II.2)}$$

Because of the choice of transformation in which $\Delta\xi = 1$ the finite difference approximation of (II.1) and (II.2) will have the form ($\frac{\partial \xi}{\partial z} = D\ell_i$)

$$\begin{aligned} D\ell \frac{\partial}{\partial \xi}(K^t D\ell \frac{\partial \alpha}{\partial \xi}) &= D\ell_i\{(K^t D\ell)_{i+1/2}(\alpha_{i+1}-\alpha_i) - \\ &\quad - (K^t D\ell)_{i-1/2}(\alpha_i-\alpha_{i-1}) = \\ &= A_i\alpha_{i-1} + B_i\alpha_i + C_i\alpha_{i+1} \end{aligned} \qquad \text{(II.3)}$$

where $A_i = (D\ell)_i(K^t D\ell)_{i-1/2}$

$$C_i = (D\ell)_i(K^t D\ell)_{i+1/2}$$

$$B_i = -(A_i + C_i) \qquad \text{(II.4)}$$

For each time step the coefficients A, B and C are computed once and used in all the following calculations.

2. Momentum equations

The momentum equations are written as

$$\frac{\partial u'}{\partial t} = fv' + D\ell\frac{\partial}{\partial \xi}(D\ell K \frac{\partial u'}{\partial \xi}) + D\ell\frac{\partial}{\partial \xi}(KD\ell\frac{\partial \bar{u}}{\partial \xi}) \quad \text{a.}$$

$$\frac{\partial v'}{\partial t} = - fu' + D\ell\frac{\partial}{\partial \xi}(D\ell K \frac{\partial v'}{\partial \xi}) + D\ell\frac{\partial}{\partial \xi}(KD\ell\frac{\partial \bar{v}}{\partial \xi}) \quad \text{b.} \qquad \text{(II.5)}$$

Introducing the Crank-Nicolson weight Θ, $\frac{1}{2} \leqslant \Theta \leqslant 1$ we write the finite difference approximation for (II.5a) as

$$\begin{aligned}\frac{u_i^{t+1}-u_i^t}{\Delta t} &= \Theta(A_i u_i^{t+1} + B_i u_i^{t+1} + C_i u_{i+1}^{t+1}) + \\ &+ (1-\Theta)(A_i u_{i-1}^t + B_i u_i^t + C_i u_{i+1}^t) + \\ &+ (A_i \bar{u}_{i-1}^t + B_i \bar{u}_i^t + C_i \bar{u}_{i+1}^t) + fv_i^t \qquad \text{(II.6)}\end{aligned}$$

where we have dropped the primes on u for convenience. Dividing by Θ and rearranging gives

$$\begin{aligned}A_i u_{i-1}^{t+1} + (B_i - \frac{1}{\Delta t\Theta})u_i^{t+1} + C_i u_{i+1}^{t+1} &= \\ = (1 - \frac{1}{\Theta})(A_i u_{i-1}^t + B_i u_i^t + C_i u_{i+1}^t &\\ - \frac{1}{\Theta}(A_i \bar{u}_{i-1} + B_i \bar{u}_i + C_i \bar{u}_{i+1}) &- \\ - \frac{fv_i^t}{\Theta} - \frac{u_i^t}{\Delta t\Theta} = \delta_i & \qquad \text{(II.7)}\end{aligned}$$

which can be written as a linear system of equations

$$\alpha_i u_{i-1}^{t+1} + \beta_i u_i^{t+1} + \gamma_i u_{i+1}^{t+1} = \delta_i \quad i=2,\ N-1$$

Boundary conditions apply at i=2 and i=N-1.

$$i=2: \quad u_1^{t+1} = - \bar{u}_1^{t+1}$$

$$i=N-1: \quad u_N^{t+1} = 0$$

The v-equation is solved after the u-equation and looks exactly as the u-equation except for the Coriolis term.

In (II.7) - fv_i^t/θ is replaced by $\frac{fu_i^{t+1}}{\theta}$. This means that the Coriolis term is not treated completely explicitly because in (II.5b) the Coriolis term is taken at time t+1 instead of t. This stabilizes the Coriolis term.

3. Thermodynamic equation

The thermodynamic equation we write as:

$$c_q \frac{\partial T'}{\partial t} + \bar{w}\{D\ell c_q \frac{\partial T'}{\partial \xi} + \frac{gLq_s}{c_p R\bar{T}} + \Gamma_d\} = D\ell \frac{\partial}{\partial \xi}(K_h D\ell \frac{\partial T}{\partial \xi}) +$$
$$+ D\ell \frac{\partial}{\partial \xi}(K_H\{D\ell \frac{\partial \bar{T}}{\partial \xi} + \Gamma_d + \frac{L}{c_p}\frac{\partial q_s}{\partial z} - \gamma_{cg}\}) -$$
$$- (c_q - 1)\frac{\partial \bar{T}}{\partial t} - \frac{1}{c_p}\frac{\partial F_s}{\partial z} \qquad \text{(II.8)}$$

The two terms $\frac{\partial \bar{T}}{\partial \xi}$ and $\frac{\partial \bar{T}}{\partial t}$ are given from the LFM or from observed data. Taking all the terms not depending on T' as H^t gives

$$H^t = D\ell \frac{\partial}{\partial \xi}(K_H\{D\ell \frac{\partial \bar{T}}{\partial \xi} + \Gamma_d + \frac{L}{c_p}\frac{\partial q_s}{\partial z} - \gamma_{cg}\}) -$$
$$- (c_q - 1)\frac{\partial \bar{T}}{\partial t} - \frac{1}{c_p}\frac{\partial F_s}{\partial z} - \bar{w}(\frac{g}{c_p}\frac{Lq_s}{R\bar{T}} + \Gamma_d) \qquad \text{(II.9)}$$

$\frac{1}{c_p}\frac{\partial F_s}{\partial z}$ represents the divergence of radiative heat flux which is computed in a subroutine, RADN, delivering point values of heating rates in a COMMON-array, HRAD. The subroutine RADN updates the flux-divergences every 12th minute, i e with a time step of 4 minutes every third time step.

(II.8) can be written

$$c_q \frac{\partial T'}{\partial t} + D\ell\bar{w}\frac{\partial T'}{\partial \xi} = \alpha_T D\ell \frac{\partial}{\partial \xi}(K\ D\ell \frac{\partial T'}{\partial \xi}) + H^t \qquad \text{(II.10)}$$

Applying the same Crank-Nicolson scheme to (II.10) as in the previous section we get the following equation for T^{t+1}.

$$\alpha_i T_{i-1}^{t+1} + \beta_i T_i^{t+1} + \gamma_i T_{i+1}^{t+1} = \delta_i \quad i=2, N-1 \quad \text{(II.11)}$$

where

$$\alpha_i = A_i + \frac{\overline{w}_i^t D\ell_i}{2\alpha_T}$$

$$\beta_i = B_i - \frac{c_q}{\alpha_T \theta \Delta t}$$

$$\gamma_i = C_i - \frac{\overline{w}_i D\ell_i}{2\alpha_T}$$

and

$$\delta_i = (1 - \frac{1}{\theta})(A_i T_{i-1}^t + B_i T_{i+1}^t + C_i T_{i+1}^t) - (1-\frac{1}{\theta})\frac{\overline{w}_i^t D\ell_i}{2\alpha T} \cdot$$

$$\cdot (T_{i+1}^t - T_{i-1}^t) - \frac{c_q}{\alpha_T \theta \Delta t} T_i^t - \frac{H^t}{\alpha_t \theta}$$

where

$$H^t = \alpha_T (A_i (\overline{T}_{i-1}^t + \frac{L}{c_p} q_{s_{i-1}}) + B_i (\overline{T}_i^t + \frac{L}{c_p} q_{s_i}) +$$

$$+ C_i (\overline{T}_{i+1}^t + \frac{L}{c_p} q_{s_{i+1}}) - \overline{w}_i (\Gamma_d + \frac{gLq_{s_i}}{c_p R T_i^t}) +$$

$$+ \alpha_T D\ell_i (\Gamma_d - \gamma_c)(K_{i+1/2} - K_{i-1/2}) -$$

$$- (c_q - 1) \frac{\Delta \overline{T}}{\Delta t} + \text{HRAD}$$

Boundary conditions

In (II.11) the following boundary conditions are applied:

$$i=2: \; T_1 = \overline{T}_1 - T_o$$

where T_o is surface temperature

$$i=N-1: \; T_N = 0$$

4. Moisture conservation equation

$$\frac{\partial q'}{\partial t} + D\ell\bar{w}\frac{\partial q'}{\partial \xi} = \alpha_T D\ell \frac{\partial}{\partial \xi}\left(D\ell K \frac{\partial q}{\partial \xi}\right) \qquad \text{(II.12)}$$

Following straight forwardly what is done above we get:

$$\alpha_i q_{i-1}^{t+1} + \beta_i q_i^{t+1} + \gamma_i q_{i+1}^{t+1} = \delta_i \quad i=2, N$$

where

$$\alpha_i = A_i + \frac{\bar{w}_i^t \cdot D\ell_i}{2 \cdot \alpha_T}$$

$$\beta_i = B_i - \frac{1}{\alpha_T \Theta \Delta t}$$

$$\gamma_i = C_i - \frac{\bar{w}_i^t D\ell_i}{2 \cdot \alpha_T}$$

$$\delta_i = (1 - \frac{1}{\Theta})(A_i q_{i-1}^t + B_i q_i^t + C_i q_{i+1}^t) -$$

$$- \frac{1}{\Theta}(A_i \bar{q}_{i-1}^t + B_i \bar{q}_i^t + C_i \bar{q}_{i+1}^t) - (1 - \frac{1}{\Theta}) \frac{\bar{w}_i^t D\ell_i}{2\ \alpha_T} \cdot$$

$$\cdot (q_{i+1}^t - q_{i-1}^t) - \frac{q_i^t}{\alpha_T \Theta \Delta t}$$

with boundary conditions at

$i=2$: if $q_1 \geqslant q_s(T_o)$ $q_1' = q_s(T_o) - \bar{q}_1$

else

$q_1 = q_{surf}$, computed from the soil moisture model.

$i=N-1$: $q_N=0$

5. Turbulent energy equation

We first write eq (41) as

$$\frac{\partial b}{\partial t} = E_1 b^{1/2} - E_2 b^{3/2} + F \qquad \text{(II.13)}$$

where

$$F = a_b D\ell \frac{\partial}{\partial \xi}(KD\ell \frac{\partial b}{\partial \xi}) \qquad \text{(a)}$$

$$E_1 = (0.2)^{1/2} \ell \cdot (S^2 - \alpha_T \frac{g}{\Theta}(D\ell \frac{\partial \Theta}{\partial \xi} - \gamma_{cg} + \frac{L}{c_p} D\ell \frac{\partial q_s}{\partial \xi})) \qquad \text{(b)}$$

$$E_2 = (0.2)^{3/2}/\ell \qquad \text{(c)} \qquad \text{(II.14)}$$

In the turbulent energy equation we apply the Crank-Nicolson scheme to the E_2 and the F terms while we take $E_1 b^{1/2}$ explicitly according to the result of the discussion in paragraph 6.5. This means

$$\frac{b^{t+1}-b^t}{\Delta t} = \Theta\left[F - E_2 b^{3/2}\right]^{t+1} + (1-\Theta)\left[F - E_2 b^{3/2}\right]^t + E_1 (b^t)^{1/2} \qquad \text{(II.15)}$$

Using the expansion of $b^{3/2}$ in eq (115) and evaluating the diffusion term we get

$$\frac{b^{t+1}-b^t}{\Delta t} = \Theta\left[F^{t+1} - \frac{3E_2}{2}(b^t)^{1/2} b^{t+1}\right] + (1-\Theta)F^t - E_2(1 - \frac{3\Theta}{2})(b^t)^{3/2} + E_1 (b^t)^{1/2} \qquad \text{(II.16)}$$

and

$$\alpha_i b_{i-1}^{t+1} + \beta_i b_i^{t+1} + \gamma_i b_{i+1}^{t+1} = \delta_i \quad i=1, N-1$$

where

$$\alpha_i = \theta\Delta t A_i$$

$$\beta_i = (B_i - e_2)\theta\Delta t - 1$$

$$\gamma_i = \theta\Delta t C_i$$

$$\delta_i = -\Delta t\{(1-\theta)(A_i b_{i-1}^t + B_i b_i^t + C_i b_{i+1}^t) + E_1(b^t)^{1/2} - (1 - \frac{3\theta}{2})E_2(b^t)^{3/2}\} - b_i^t$$

and

$$e_2 = \frac{3}{2} \cdot \frac{(b^t)^{1/2} \cdot (0.2)^{3/2}}{\ell}$$

Boundary conditions

i=1: Two boundary conditions are possible:

1) Assuming a logarithmic wind profile and constant stress in lowest part of the surface layer implies that

$$b_1 = 5.0\ell^2 S^2$$

(first integrated point i=2)

This boundary condition was tested and worked well in the stable boundary layer. In the unstable ABL it seemed to underestimate the turbulent energy when the surface heating was strong.

Instead the following boundary condition was tested and found to work satisfactory for both cases.

2) $(\frac{\partial b}{\partial z})_{z=0} = 0$

or at i=1: $A_1 = 0$

$B_1 = - C_1$

(i=1, first grid point integrated)

i=N-1: At z=H we have $\frac{\partial b}{\partial z} = 0$

which corresponds to the numerical boundary conditions

$C_{N-1} = 0$

$B_{N-1} = - A_{N-1}$

6. Soil heat equation

The thermal diffusivity is constant and we transform eq (69) according to the transformation eq (99) giving

$$\frac{\partial T_s}{\partial t} = K_s b^2 a^2 e^{\frac{-2(z-1)}{a}} (\frac{\partial^2 T_s}{\partial z^2} - \frac{1}{a} \frac{\partial T_s}{\partial z}) \qquad \text{(II.18)}$$

The depth, D, is taken as 1 m and 21 points are used to resolve this layer.

This gives

$$a = \frac{N-1}{\ell n(bD+1)} \qquad \text{(II.19)}$$

and a = 5.0867

b = 50.0

Putting $s = K_s a^2 b^2$

$$g(z) = e^{\frac{2(z-1)}{a}}$$

we get with the Crank-Nicolson scheme

$$\alpha_i T_{s_{i-1}}^{t+1} + \beta_i T_{s_i}^{t+1} + \gamma_i T_{s_{i+1}}^{t+1} = \delta_i \quad i=2, N-1$$

where

$$\alpha_i = 1 + \frac{1}{2a}$$

$$\gamma_i = 1 - \frac{1}{2a}$$

$$\beta_i = -2 - \frac{1}{sg_i \Delta t \theta}$$

$$\delta_i = (1 - \frac{1}{\theta})(\alpha_i T_{s_{i-1}}^{t} - 2 \cdot T_{s_i}^{t} + \gamma_i T_{s_{i+1}}^{t}) - \frac{T_{s_i}^{t}}{sg_i \theta \Delta t}$$

Boundary conditions:

$$i=1: \quad T_{s_1} = T_o = T_{surf}$$

$$i=N: \quad T_{s_N} = T_D = \text{constant}$$

The soil temperature profile is initialized in the following way:

From initial values of u, v, T and q the surface temperature is estimated by means of Monin-Obukhov's similarity theory for the surface layer. This also gives initial surface fluxes of heat and latent heat. The radiation subroutine gives the net radiation at the surface.

Adding these fluxes gives a net flux which has to be compensated by a soil heat flux if requiring an energy balance at the surface. Call this flux F_{in}.

$$F_{in} = -K_s \cdot \frac{T_2 - T_1}{z_2}, \quad T_1 = T_{surf}$$

which gives

$$T_2 = T_{surf} - z_2 \cdot F_{in}/K_s$$

T_D is set to $0.99 \cdot T_2$ and an exponential function:

$$T(z) = A \cdot e^{-BZ} + T_D \qquad \text{(II.20)}$$

is fitted to T_{surf} and T_2. (II.20) is the initial soil temperature profile.

7. Integration scheme

All the simple tri-diagonal systems of linear equations are solved by means of Gaussian elimination.

The model is stepped forward in time in the following manner.

A time step starts with the calculation of boundary values, i e $\bar{u}$, $\bar{v}$, $\bar{T}$, $\bar{q}$, T_{surf} and q_{surf} and when needed interpolation of $\bar{w}$ and wind shear, clouds etc.

The time integration is entered by computing the diffusion coefficients A, B and C which are used in all equations.

The equations are integrated in the following order

u-equation
v-equation, u^{t+1} used in Coriolis term
T-equation
q- equation
Turbulent Energy equation

and finally

surface temperature equation.

After this diagnostic computations are invoked in which auxiliary parameters are computed. This includes Richardson number, boundary layer height, shear, saturation specific humidity, potential temperature, mixing length, eddy diffusivity, K, and the counter-gradient term. Then the cycle starts again.

At the present time the model is run on a UNIVAC 1100/21 computer system and is coded in FORTRAN. With 35 gridpoints and a timestep of 4 minutes about 2 minutes of CPU are needed for a 24 hour forecast.

LITERATURE REFERENCES

André, J.C., et al., 1978: Modeling the 24-hour evolution of the mean and turbulent structures of the planetary boundary layer. JAS, Vol. 35, No. 10.

Atwater, M.A., 1970: Investigation of the radiation balance for polluted layers of an urban environment. Ph.D. Dissertation. New York University.

Atwater et al., 1974: A description of a general 3-dimensional numerical simulation model of a coupled air-water and/or air-land boundary layer. The Center for the Environment and Man. CEM-Report No. 4131-509a.

Barr & Kreitzberg, 1975: Horizontal variability and boundary layer modeling. BLM, Vol. 8, No. 2.

Betts, A.K., 1973: Non-precipitating cumulus-convection and its parameterization. QJRMS, Vol. 99, p. 178.

Betts, A.K., 1974: Further comments on "a comparison of the equivalent potential temperature and the static energy". JAS, Vol. 31, No. 9.

Blackadar, A., 1957: Boundary layer wind maxima and their significance for the growth of nocturnal inversions. Bull. of AMS., Vol. 38, No. 5.

Blackadar, A.K., 1962: The vertical distribution of wind and turbulent exchange in a neutral atmosphere. J. of Geophys. Res. Vol. 67, No. 8.

Bodin, S., 1974: Development of un unsteady atmospheric boundary layer model. SMHI-Reports, RMK No. 2.

Bodin, S., 1976: An unsteady one-dimensional atmospheric boundary layer model. Proceedings from the WMO Symposium on the Interpretation of broad-scale NWP products for local forecasting purposes. Warsaw, Oct. 1976. WMO-No 450.

Bodin, S., 1978: Applied numerical modeling of the atmospheric boundary layer. SMHI-Reports No. RU 15.

Bradshaw et al., 1967: Calculation of boundary layer development using the turbulent energy equation. J. Fluid Mech., Vol 28, part 3, p. 593.

Brown & Roach, 1976: The physics of radiation fog: II-a numerical study. QJRMS. Vol. 102, p. 325.

Businger et al., 1971: Flux-profile relationships in the atmospheric surface layer. JAS, Vol. 28, No. 3.

Ching & Businger, 1968: The response of the planetary boundary layer to time varying pressure gradient force. JAS, Vol. 25, p. 1021.

Clarke et al., 1971: The Wangara experiment. Boundary layer data. CSIRO. Div. of Met. Phys. Techn. Paper No. 19.

Clarke, R.H., 1974: Attempts to simulate the diurnal course of meteorological variables in the boundary layer. Izvt. Atm. and Oceanic Phys. Vol. 10, No. 6, (English translation).

Deardorff, J.W., 1966: The counter-gradient heat flux in the lowest atmosphere and in the laboratory. JAS, Vol. 23, p. 503.

Deardorff, J.W., 1972: Theoretical expressions for the counter-gradient vertical heat flux. J. of Geophysical Res. Vol. 77, No. 30.

Deardorff, J.W., 1973: The use of subgrid transport equations in a three-dimensional model of atmospheric turbulence. Paper presented at the Applied Mechanics and Fluid Engineering Conference, Atlanta, Ga, June 1973.

Deardorff, J.W., 1974a: Three-dimensional numerical study of the height and mean structure of a heated planetary boundary layer. BLM, 7, p. 81.

Deardorff, J.W., 1974b: Three-dimensional numerical study of turbulence in an entraining mixed layer. BLM, Vol. 7, p. 199.

Deardorff, J.W., 1976: Usefulness of liquid-water potential temperature in a shallow cloud model. JAM, Vol. 15, No. 1.

Deardorff, J.W., 1977: Efficient prediction of ground surface temperature and moisture with inclusion of a layer of vegetation. NCAR-Research Papers. Jan., 1977.

Delage, Y., 1974: A numerical study of the nocturnal atmospheric boundary layer, QJRMS, Vol. 100, p. 351.

Djolov, G.D., 1973: Modeling of interdependent diurnal variation of meteorological elements in the boundary layer. Ph. D. thesis. University of Waterloo, Canada.

Donaldson, C. du P., 1973: Construction of a dynamic model of atmospheric turbulence and the dispersal of atmospheric pollutants. Workshop in micro-meteorology. American Met. Society.

Gutman, L.N., 1969: Introduction to the non-linear theory of meso-scale processes. Leningrad 1969. English translation by Israel Programme for Scientific Translation. Jerusalem, 1972.

Gutman, L.N., & Perov, V.L., 1970: Non-stationary problems in meso-meteorology. Izv. Atm. and Oceanic Phys. Vol. 6, No. 1. (English translation).

Halstead et al., 1957: A preliminary report on the design of a computer of micrometeorology. J. of Met., Vol. 14, p. 308.

Kaimal, J.C., et al., 1976: Turbulence structure in the convective boundary layer. JAS, Vol. 33, Nov. p. 2152.

Karlsson, E., 1972: A numerical model for the boundary layer of the atmosphere at neutral and stable stratification. DM-7. Inst of Meteorology, University of Stockholm (in Swedish).

Karlsson, E. & Aspling, G., 1977: Experiments with a numerical model for the boundary layer of the atmosphere. MVC Rapport F8, Swedish Military Weather Service.

Kondratyev, K., 1969: Radiation in the atmosphere. International Geophysics Series, Vol. 12, Academic Press, New York.

Kuhn, P.M., 1963: Radiometersonde observations of infrared flux emissivity of water vapor. JAM, Vol. 2, p. 368.

Lenschow, D.H., 1970: Airplane measurements of Planetary Boundary Layer structure. JAM, Dec.

Long, P.E., 1975: Dissipation dispersion and difference schemes. NOAA Techn. Memo NWS TDL-56.

Long & Schaffer, 1975: Some physical and numerical aspects of boundary layer modeling. NOAA Tech. Memo NWS-TDL-56.

Lumley, J.L., & Panofsky, H.A., 1964: The structure of atmospheric turbulence. New York, Interscience.

Lykosov, V.N., & Gutman, L.N., 1972: Turbulent boundary layer above a sloping underlying surface. Izv. Atmospheric and Oceanic Physics, Vol. 8, No. 8, (English translation).

Madden & Robitaille, 1970: A comparison of the equivalent potential temperature and the static energy, JAS, Vol. 27, p. 327.

McDonald, J.E., 1960: Direct absorbtion of solar radiation by atmospheric water vapor. J. of Met., Vol. 17, p. 319.

Mellor & Yamada, 1974: A hierarchy of turbulence closure models. JAS, Vol. 31, October.

Monin & Yaglom, 1971: Statistical Fluid Mechanics. Mechanics of Turbulence. Vol. 1. MIT-press.

Nappo Jr, C.J., 1975: Parameterization of surface moisture and evaporation rate in a planetary boundary layer. JAM, Vol. 14, No. 3, p. 289.

Nappo Jr, C.J., 1977: Mesoscale flow over complex terrain during the eastern Tennessee Trajectory Experiment (ETTEX). JAM, Vol. 16, Nov.

Pandalfo et al., 1971: Prediction by numerical models of transport and diffusion in an urban boundary layer. The Center for the Environment and Man.

Petersen, E.W., 1969: Modification of mean flow and turbulent energy by a change in surface roughness under conditions of neutral stability. QJRMS, Vol. 95, p. 561.

Richtmyer, R.D. & Morton, K.W., 1967: Difference methods for initial-value problems. Interscience, John Wiley & Sons.

Rodgers, C.D., 1977: Radiative processes in the atmosphere. ECMWF Seminar on 'The parameterization of the physical processes in the free atmosphere'.

Sasamori, T., 1970: A numerical study of atmospheric and soil boundary layers. JAS, Vol. 27, p. 1122.

Shaffer & Long, 1973: A predictive boundary layer model. Paper presented at the Symposium on the Atmospheric Boundary Layer, Oct., 1973, Mainz, Germany.

Shir, C.C., 1973: A preliminary numerical study of atmospheric turbulent flows in the idealized planetary boundary layer. JAS. Vol. 30, p. 1327.

Speranskiy et al., 1975: The turbulent planetary boundary layer above a curve-linear underlying surface in the presence of horizontal heat advection. Izv. Atm and Ocean Phys. Vol. 11, No. 5 (English translation).

Taylor & Delage, 1971: A note on finite-difference schemes for the surface and planetary boundary layers. BLM, Vol. 2, p. 108.

Thorpe, A.J., & Guymer, T.H., 1977: The nocturnal jet. QJRMS, Vol. 103, p. 633.

Warner, J., 1971: Observations of the eddy fluxes of heat and vapor over the sea. QJRMS, Vol. 97, p. 540-547.

Wyngaard, J.C., 1975: Modeling the Planetary Boundary Layer-extension to the stable case. BLM 9, p. 441.

Wyngaard & Coté, 1974: The evolution of a convective planetary boundary layer - a higher order closure model study. BLM, Vol. 7, p. 289.

Yamada & Mellor, 1975: A simulation of the Wangara atmospheric boundary layer data. JAS, Vol. 32, Dec.

Yu, T.W., 1976: Numerical studies of the atmospheric boundary layer with a turbulent energy closure scheme. AMS third symposium on Atmospheric Turbulence, Diffusion and Air Quality. Raleigh, N.C., Oct. 1976.

Zdunkowski & Trask, 1971: Application of a radiative-conductive model to the simulation of nocturnal temperature changes over different soil types. JAM, Vol. 10, p. 937.

Zdunkowski et al., 1975: The effect of soil moisture upon atmospheric and soil temperature near the air-soil interface. Arch. Met., Geoph., Biokl., Ser. A, Vol. 24, p. 245.

Zilitinkevich, D.L., et al., 1967: Dynamics of the atmospheric boundary layer. Izv. Atm. and Oceanic Phys. Vol. 3, No. 3 (English translation).

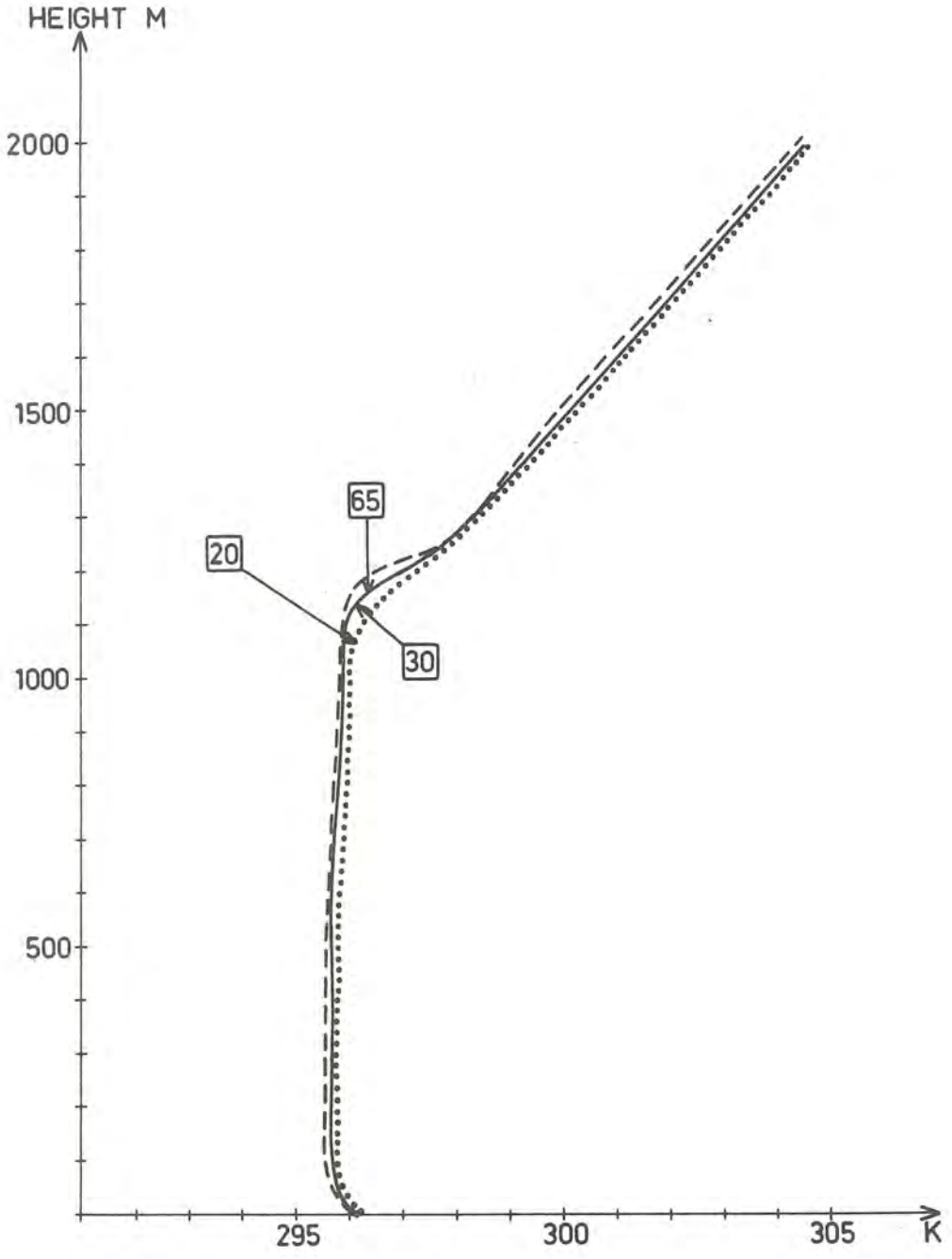

Fig. 8

Vertical profiles of potential temperature using different resolutions - 20, 30 and 65 grid points between the surface and 2000 m. After 6 hours of integration.

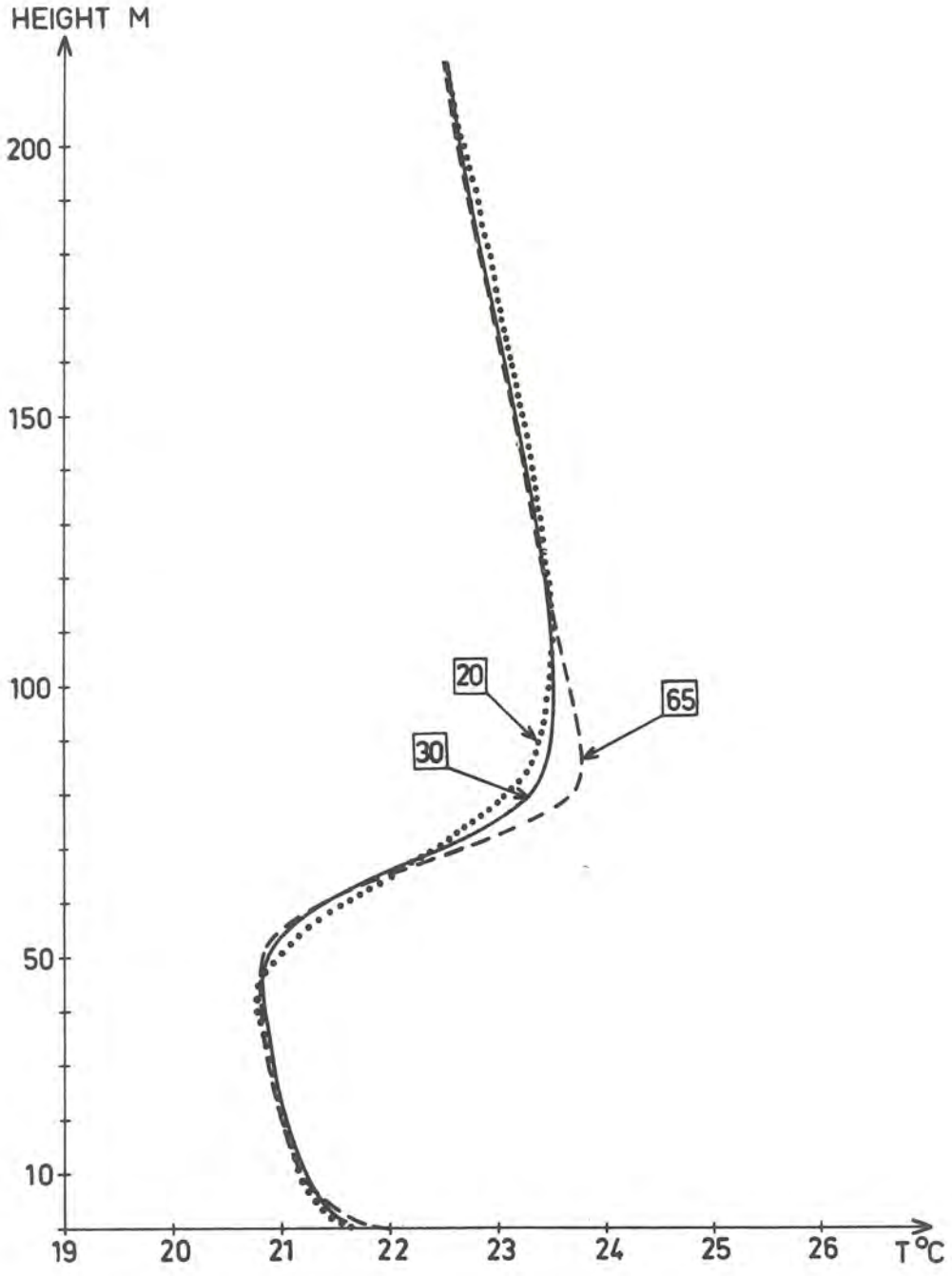

Fig. 9

Vertical profiles of temperature using different resolutions - 20, 30 and 65 grid points between the surface and 2000 m. After 24 hours of integration.

a)

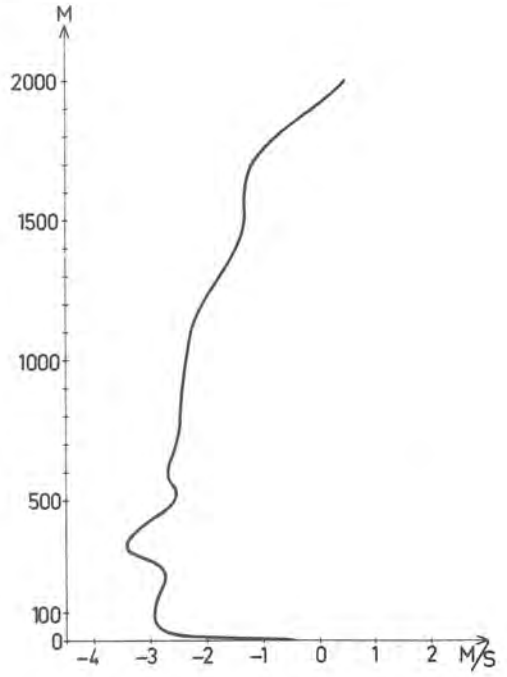

u

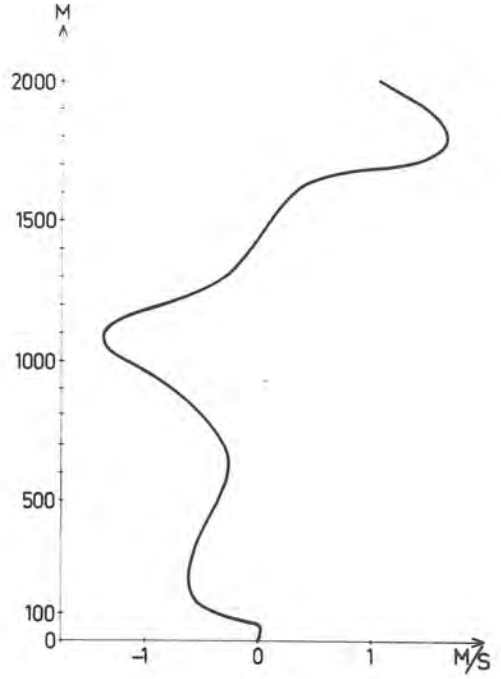

v

b)

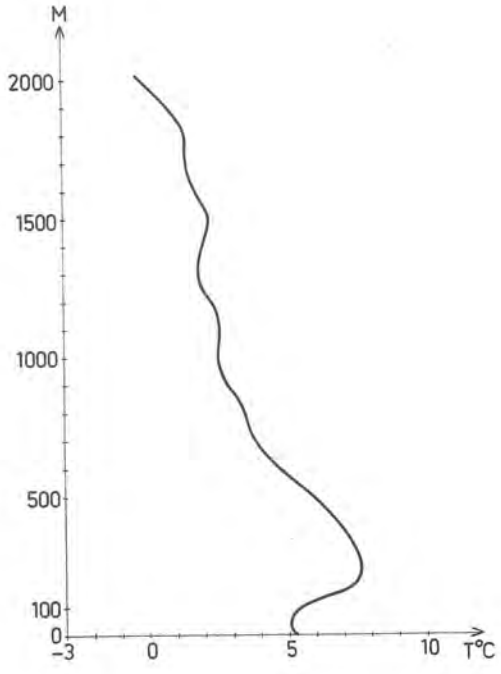

T

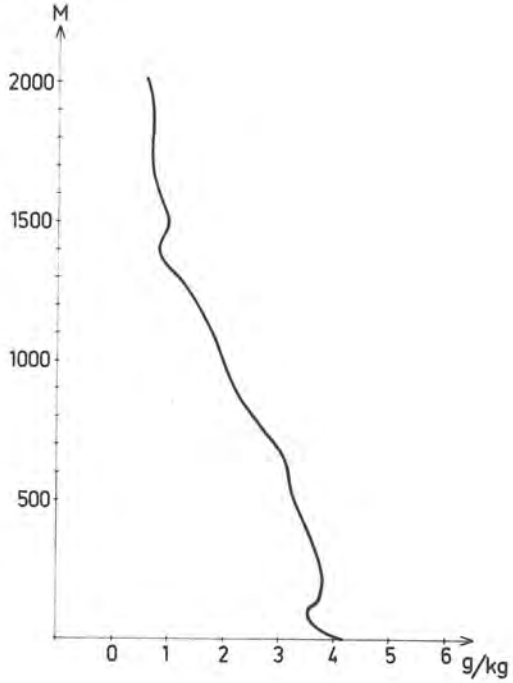

q

Fig. 10

a) Initial profiles of u- and v-components of the wind at 0900 o'clock, Day 33 of the Wangara data, used in the model simulations.

b) Same as fig 10a but for temperature and specific humidity.

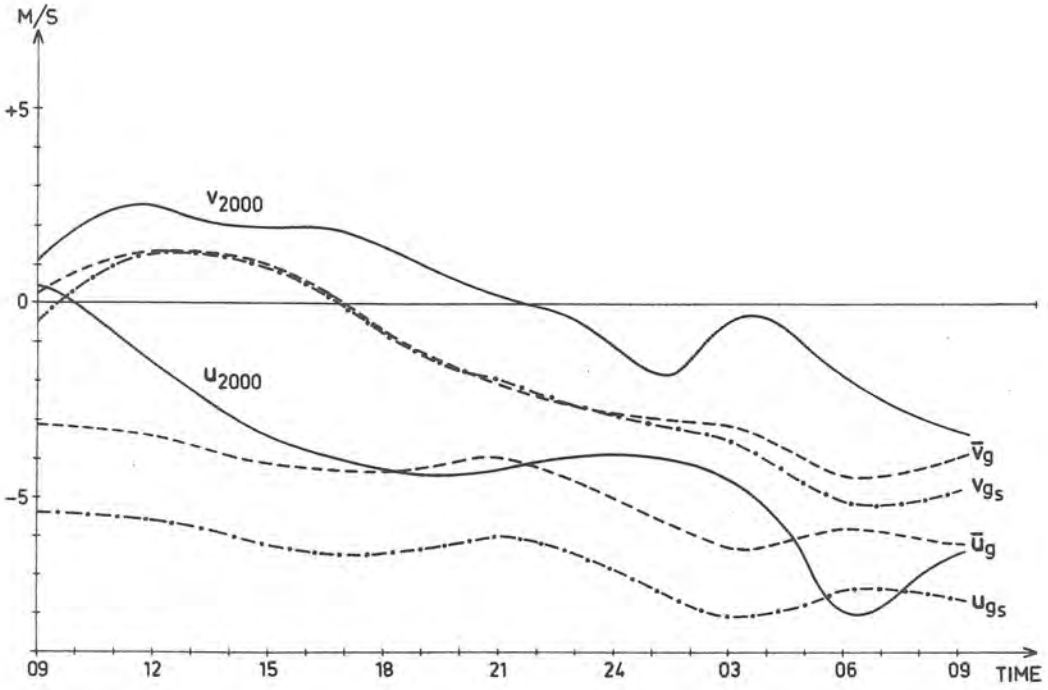

Fig. 11

Various wind components as a function of time during day 33 and 34 of the Wangara data. Full curves show observed 2000 m u- and v-components, dashed curves show mean geostrophic wind components in the layer between the surface and 2000 m and dashed-dotted curves surface geostrophic wind components.

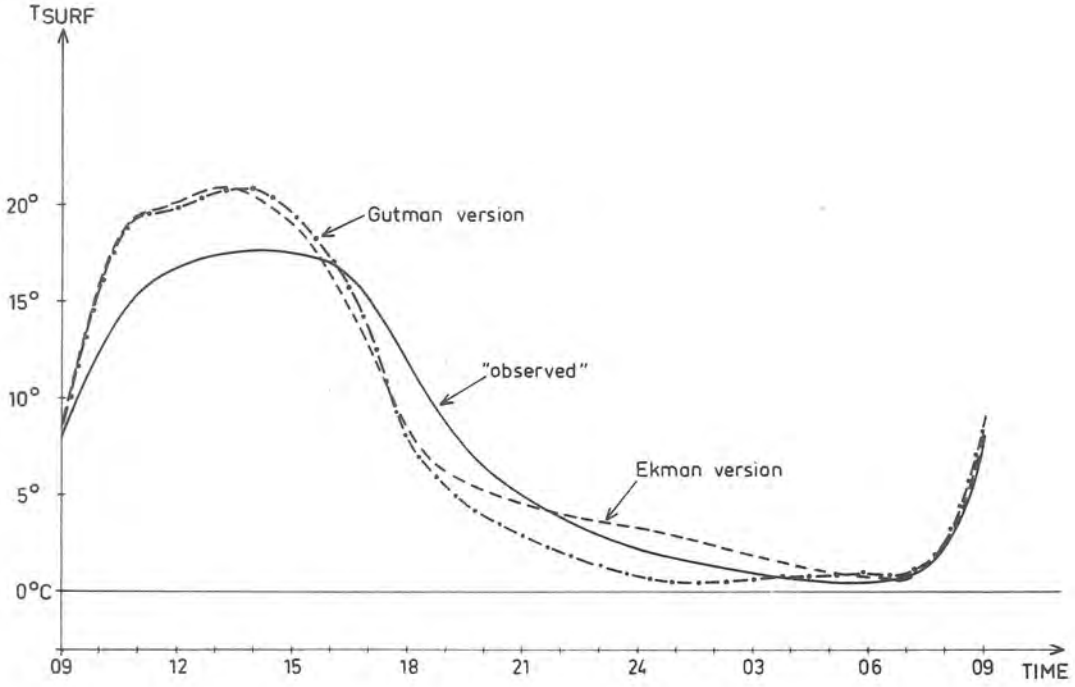

Fig. 12

Surfaces temperatures as a functions of time. Full curve shows surface temperature calculated from observed 1.2 m temperature using Monin-Obukhov's similarity theory. Dashed curve shows predicted surface temperature by the Ekman-version of the model (no shear) and the dashed-dotted curve the surface temperature predicted by the Gutman-version of the model. Day 33 and 34 of the Wangara data.

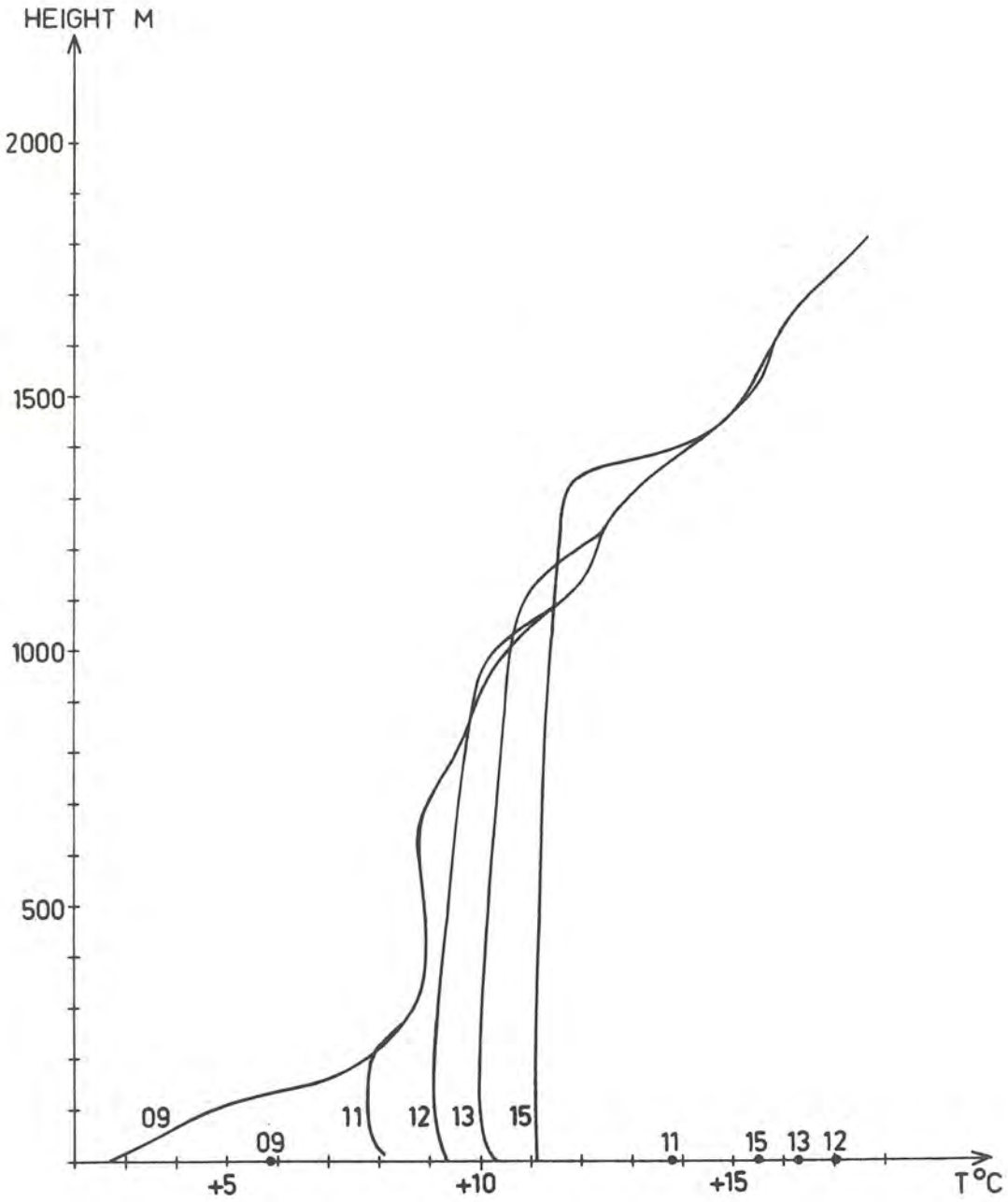

Fig. 13

Day-time potential temperature profiles predicted by the Gutman-version of the model. In this case the surface temperature in fig. 12 is used as lower boundary condition.

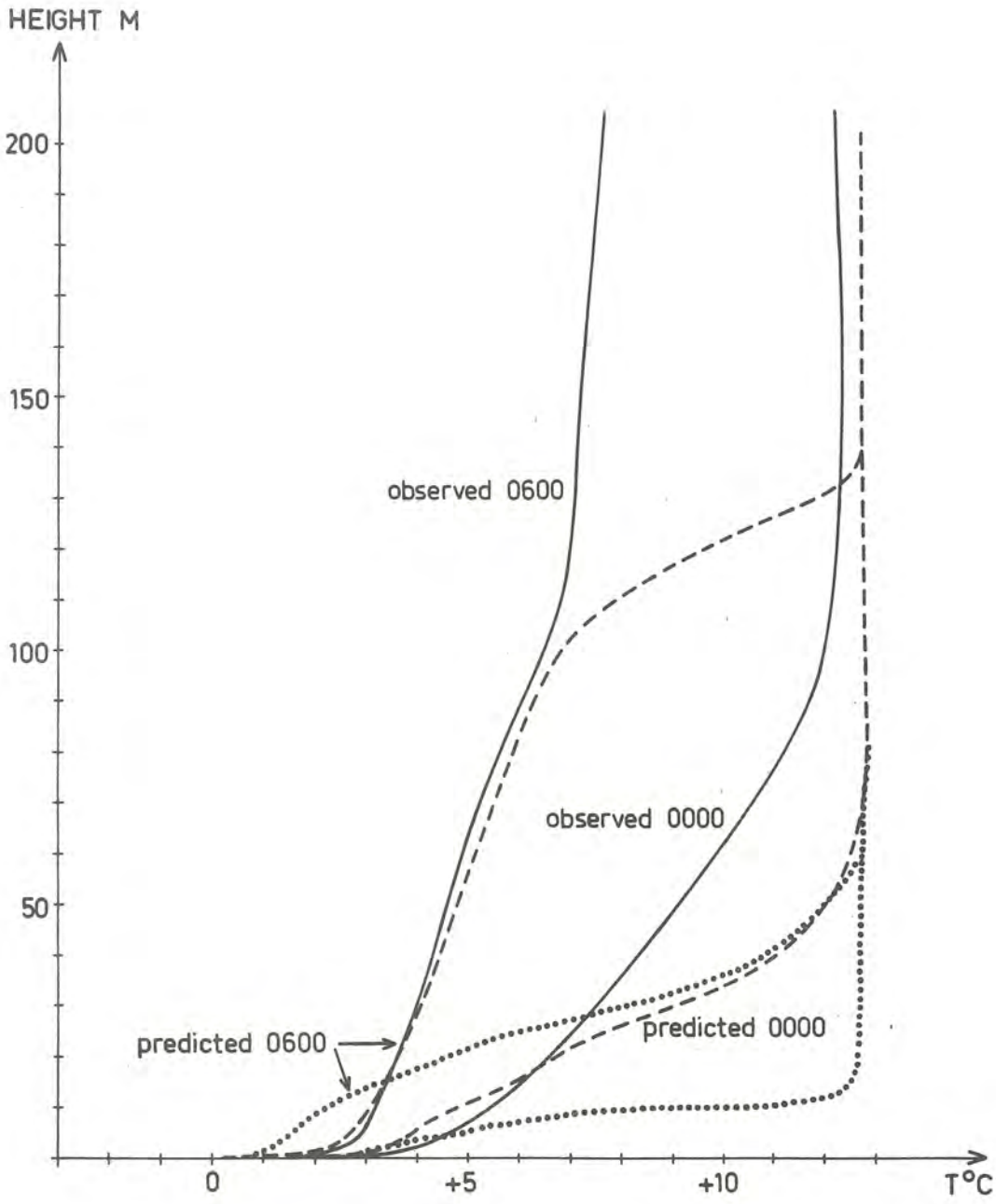

Fig. 14

Same as fig. 13 but for nocturnal temperature profiles. Full lines show observed values and dashed lines predicted values. The two dotted curves show the predicted temperature profiles when using Delage's mixing length (see text).

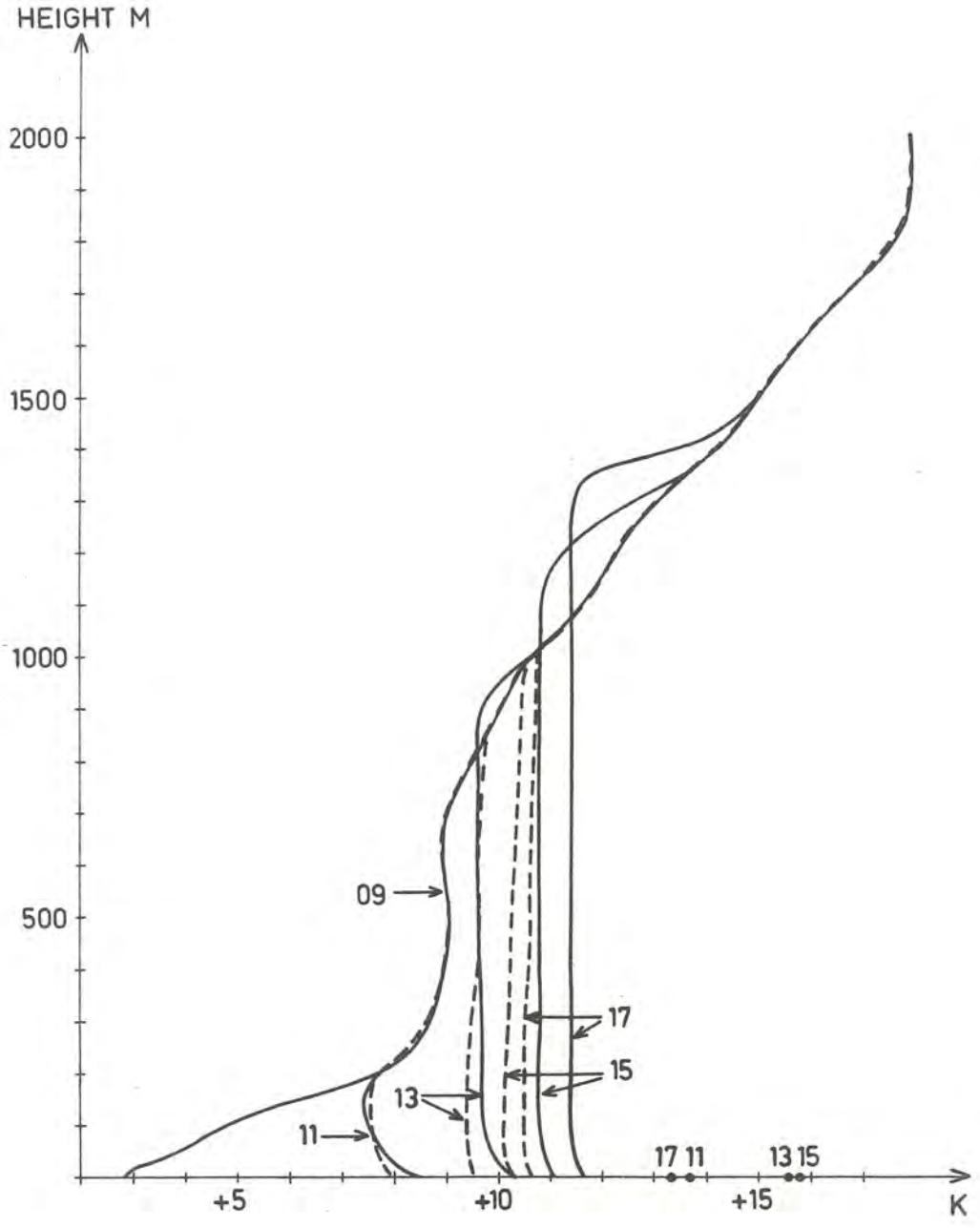

Fig. 15

Predicted day-time potential temperature profiles with prescribed surface temperature variation. The dashed profiles show the effect of putting the diffusion term, $\frac{\partial}{\partial z}(K\frac{\partial b}{\partial z})$, equal to zero in the turbulent energy equation and the full curves profiles resulting after putting the counter-gradient heat flux term, γ_{cg}, equal to zero. (Compare with fig. 13). Day 33 of the Wangara data.

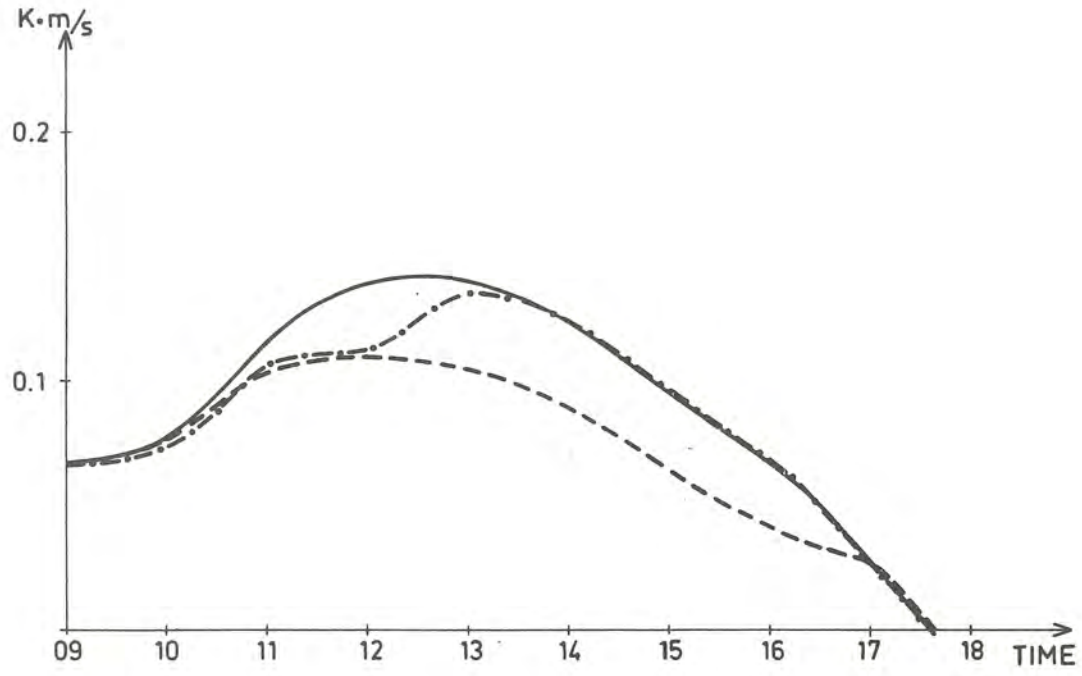

Fig. 16

Surface kinematic heat flux as a function of time. Full curve is the normal model simulation, dashed curve when putting the diffusion term, $\frac{\partial}{\partial z}(K\frac{\partial b}{\partial z})$, equal to zero in the turbulent energy equation and the dashed-dotted curve putting γ_{cg} equal to zero. Day 33 of the Wangara data.

a)

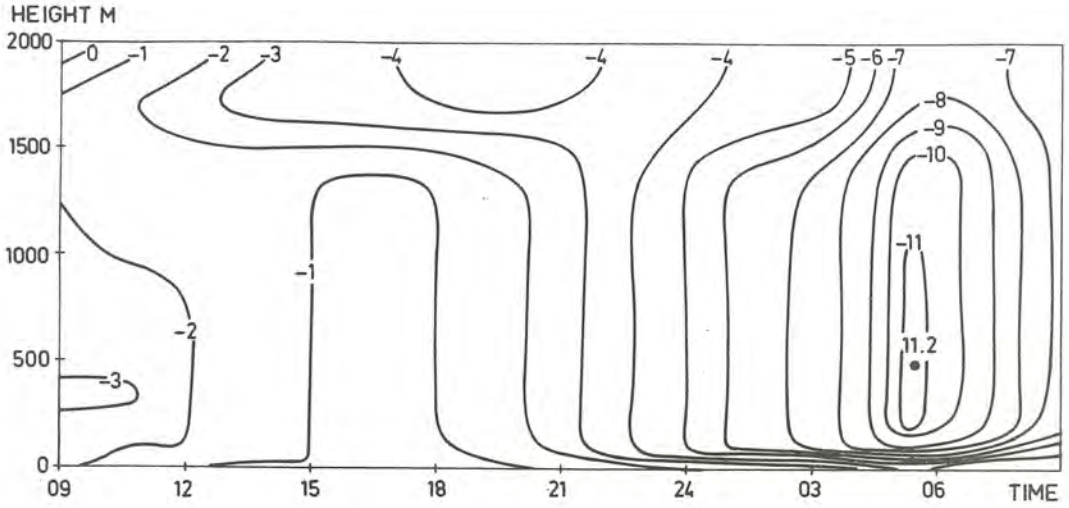

b)

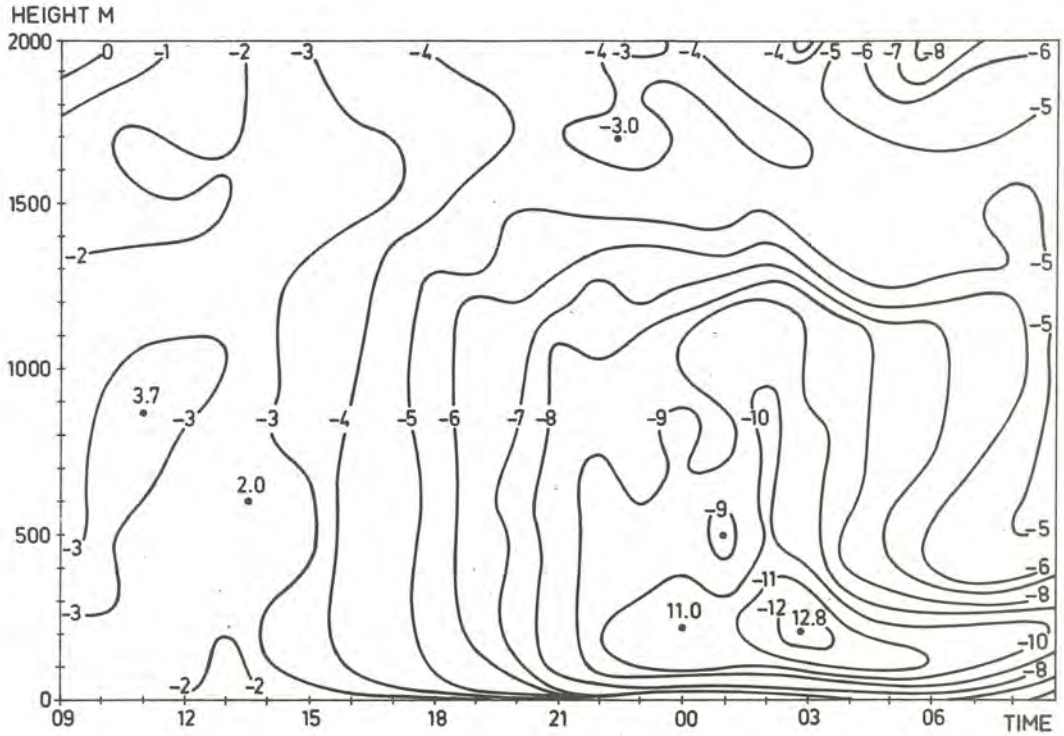

Fig. 17

a) Predicted time-height cross-section of the u-component of the wind. Gutman-version with prescribed surface temperature. Day 33 and 34 of the Wangara data.

b) Observed time-height cross-section of the u-component of the wind. Day 33 and 34 of the Wangara data.

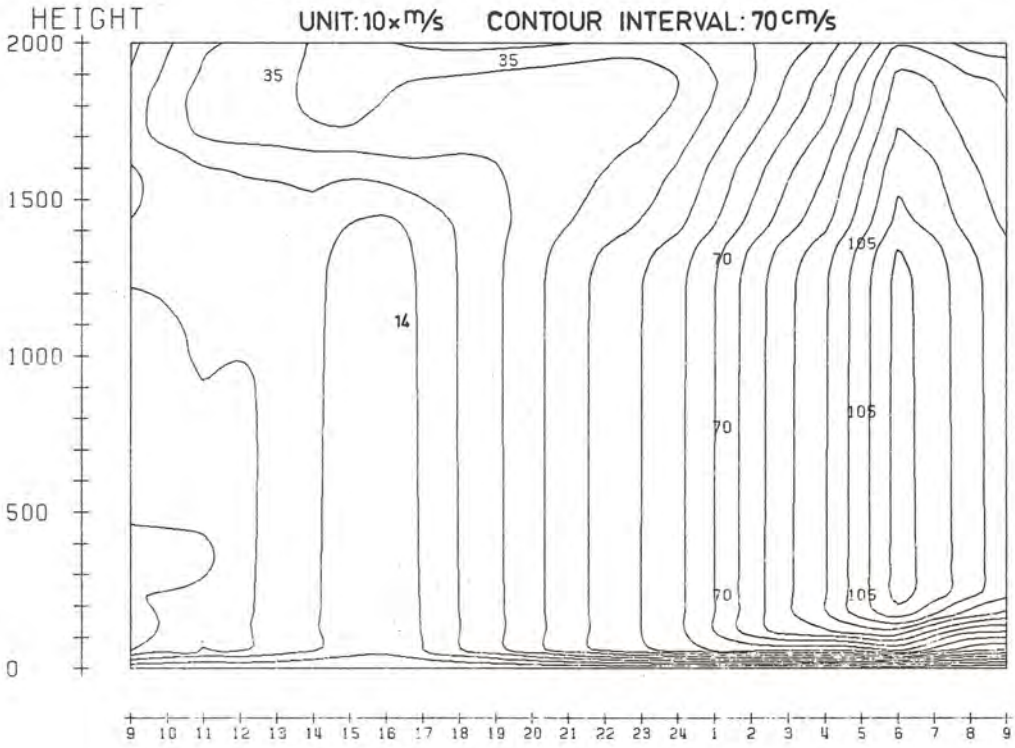

Fig. 18

Predicted time-height cross-section of wind speed using the full Gutman-version including radiation, surface energy balance and vertical velocities. Day 33 and 34 of the Wangara data.

a)

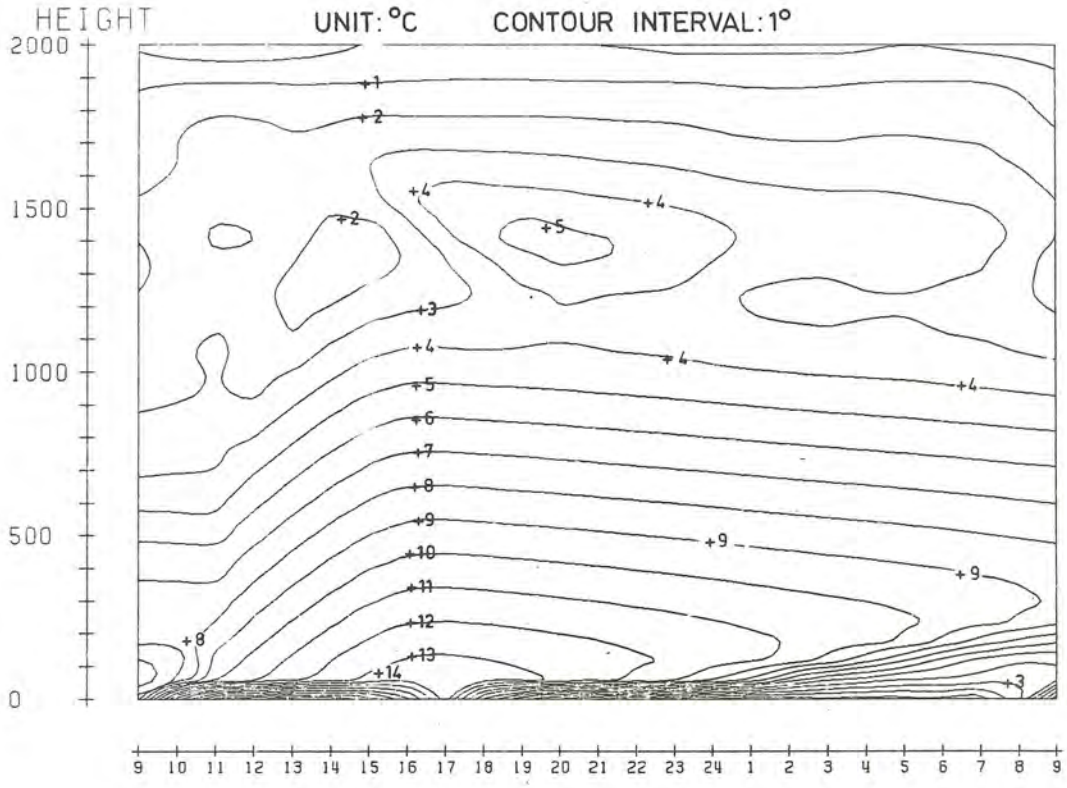

b)

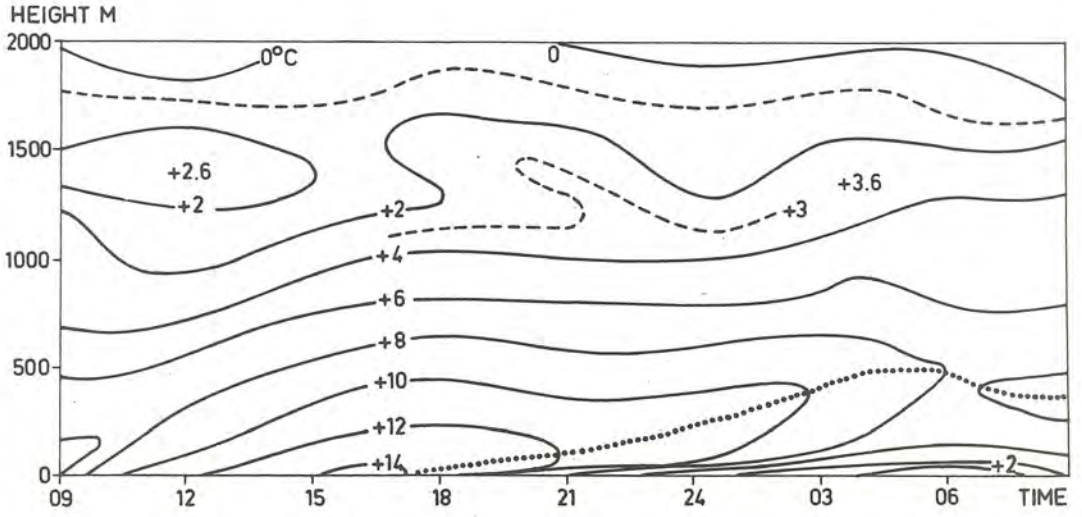

Fig. 19

a) Same as fig. 18 but for temperature.

b) Same as fig. 19a but for observed temperature.

a)

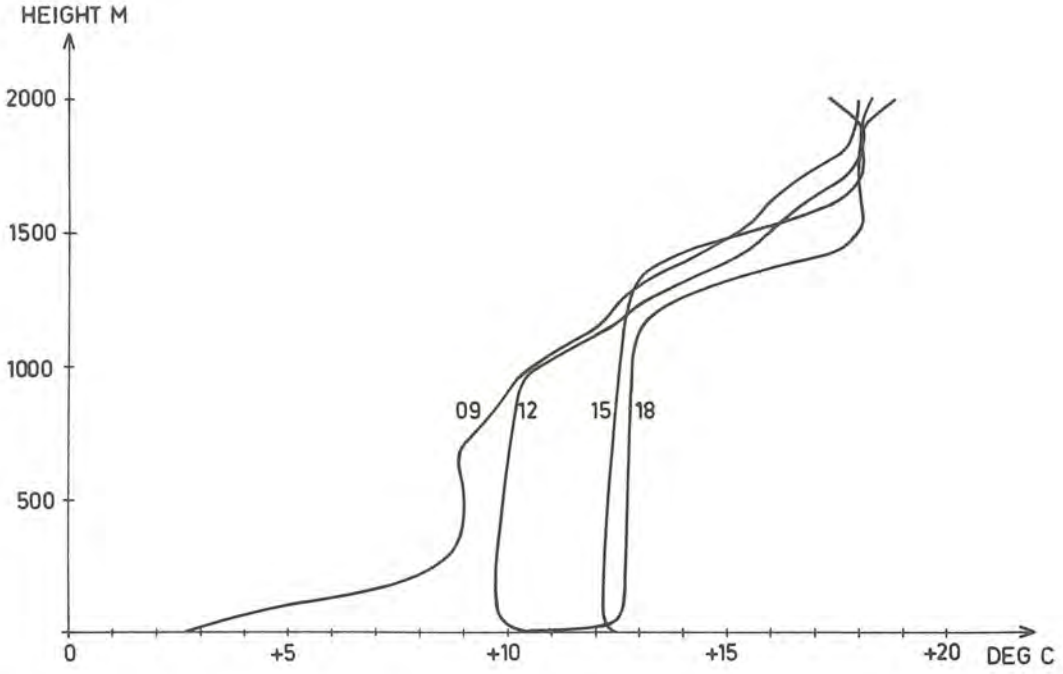

b)

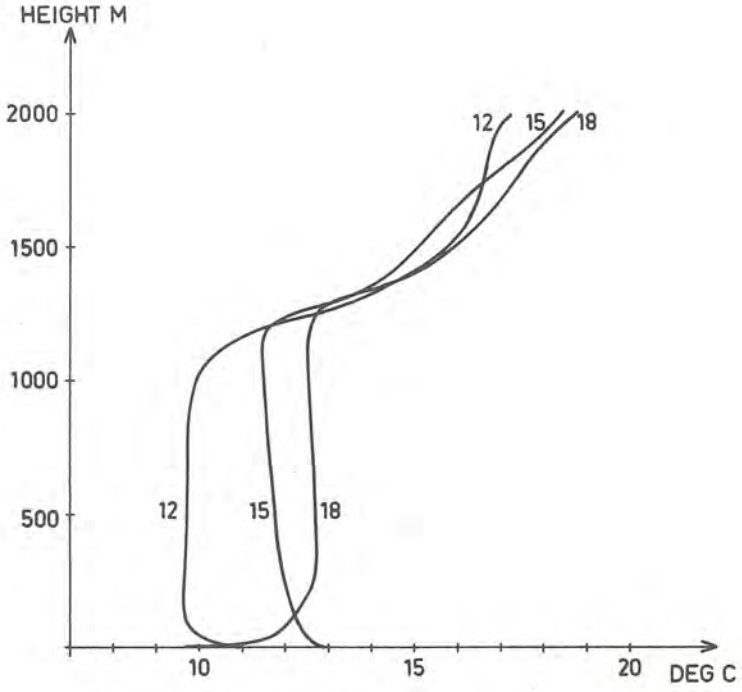

Fig. 20

a) Predicted day-time potential temperature profiles by the full Gutman-version, day 33.

b) Observed potential temperature profiles. Day 33.

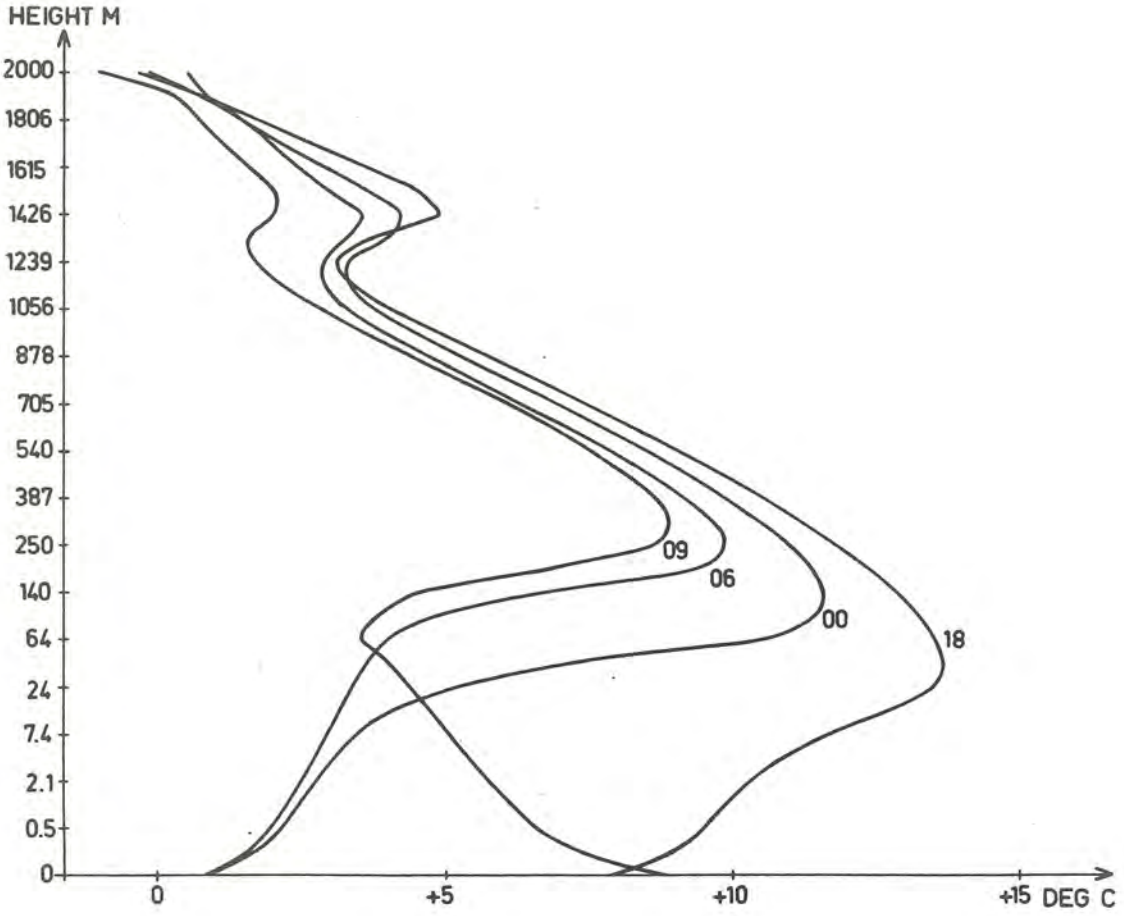

Fig. 21a

Nocturnal temperature profiles predicted by the full Gutman model. Day 33 and 34. Note the log-linear height scale. Height values refer to every second grid point.

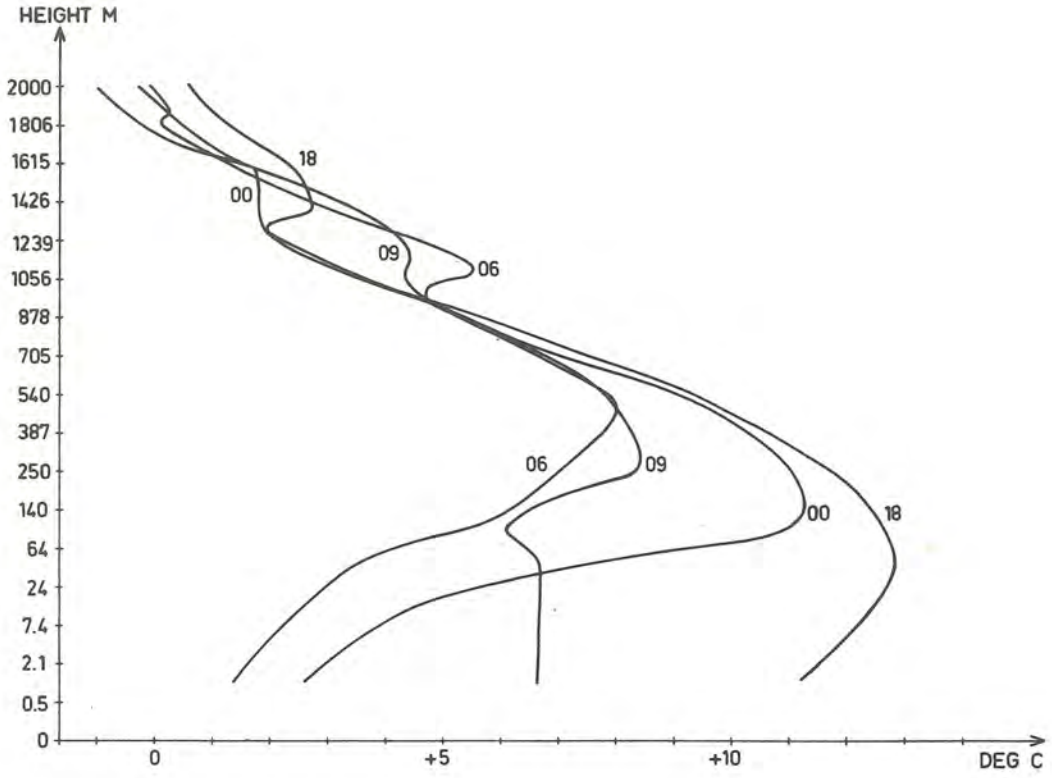

Fig. 21b

Observed nocturnal temperature profiles.
Day 33 and 34.

a)

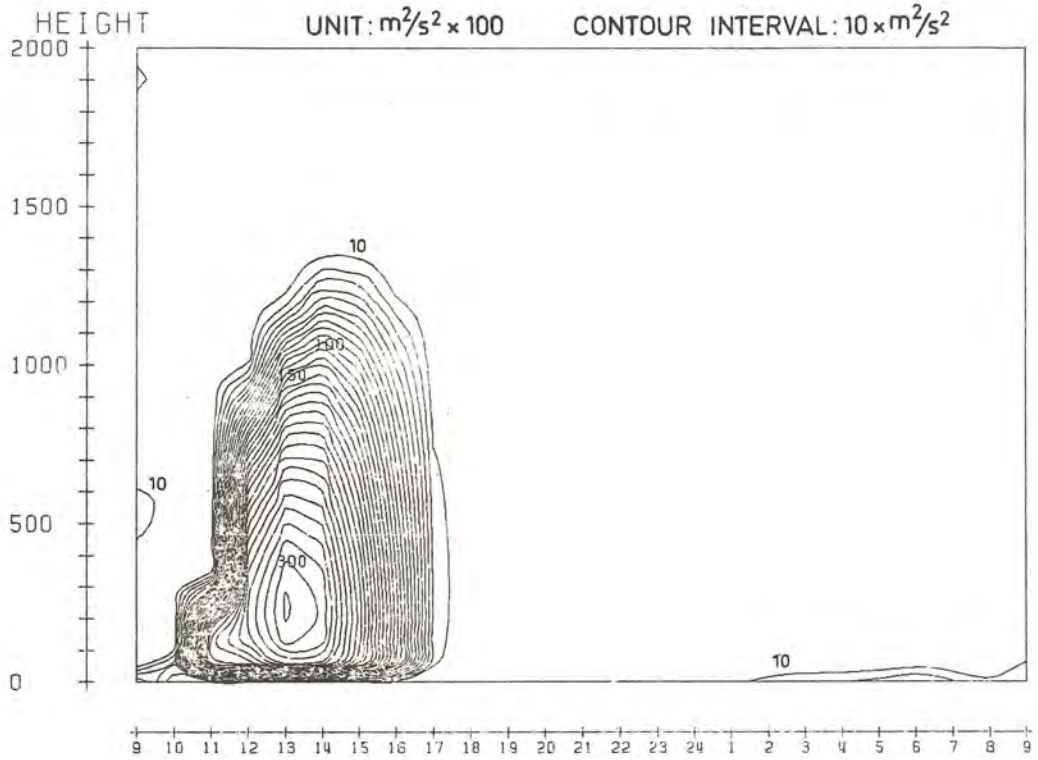

b)

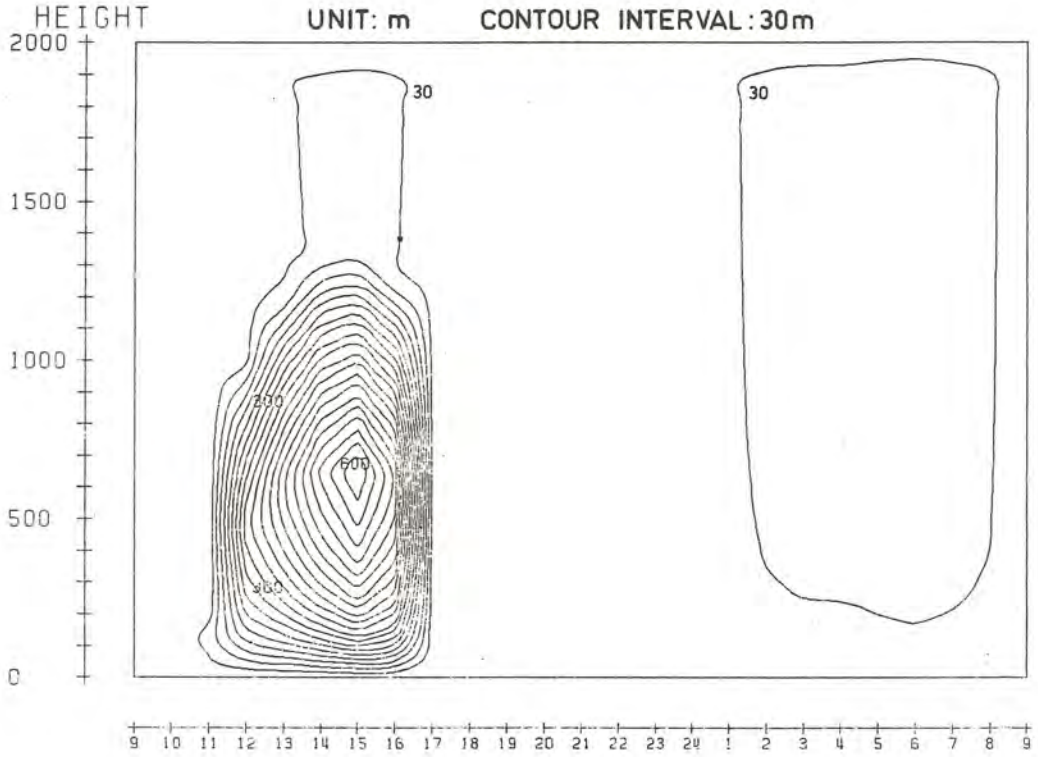

Fig. 22

a) Predicted time-height cross-section of turbulent energy by full Gutman model. Values multiplied by 100. Day 33 and 34.

b) Same as fig. 22a but for the mixing length. Values in meters.

a)

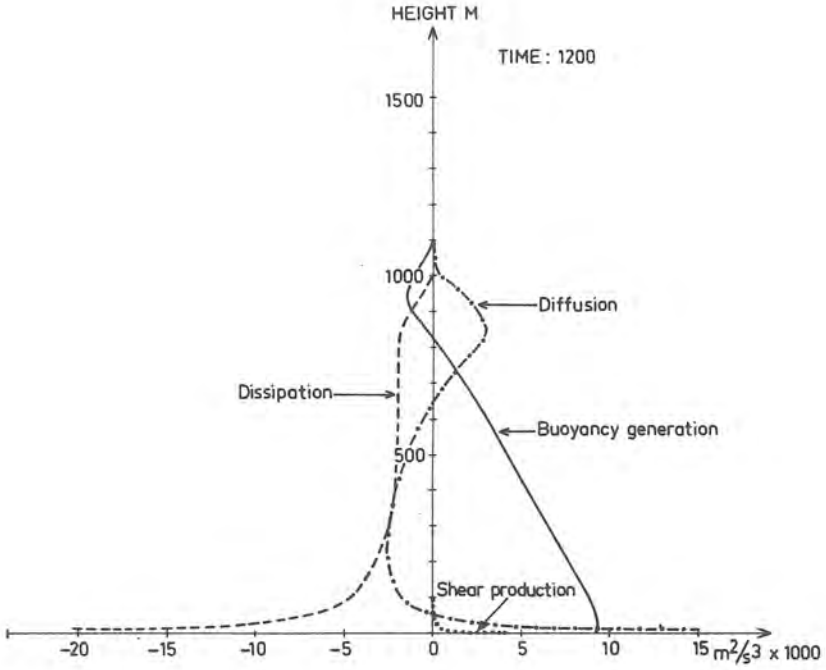

b)

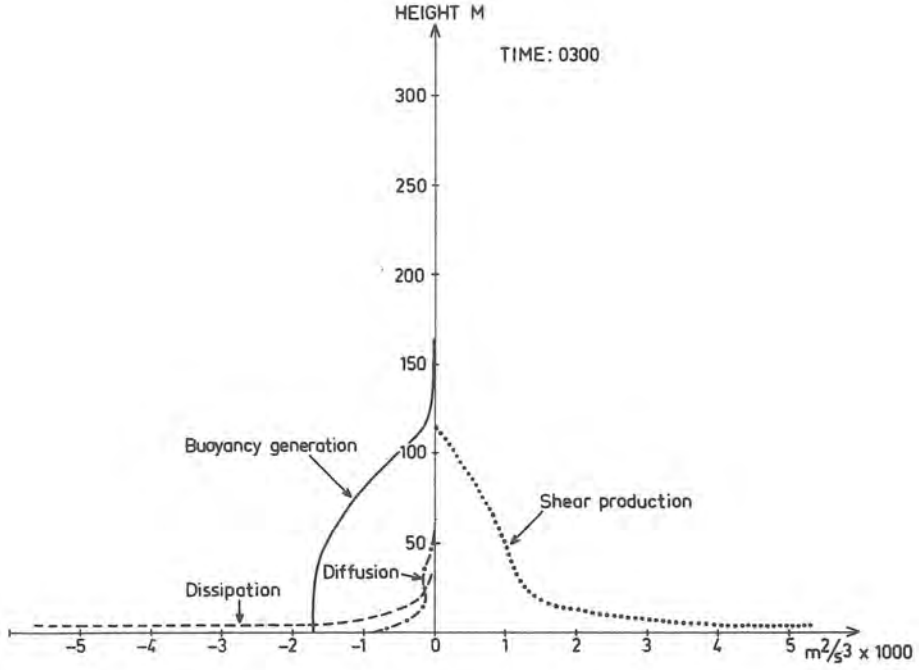

Fig. 23

a) Predicted vertical profiles of the terms in the turbulent energy equation at 1200 o'clock, day 33. Values multiplied by 1000. Full Gutman model.

b) Same as fig. 23a but at 0300 o'clock, day 34.

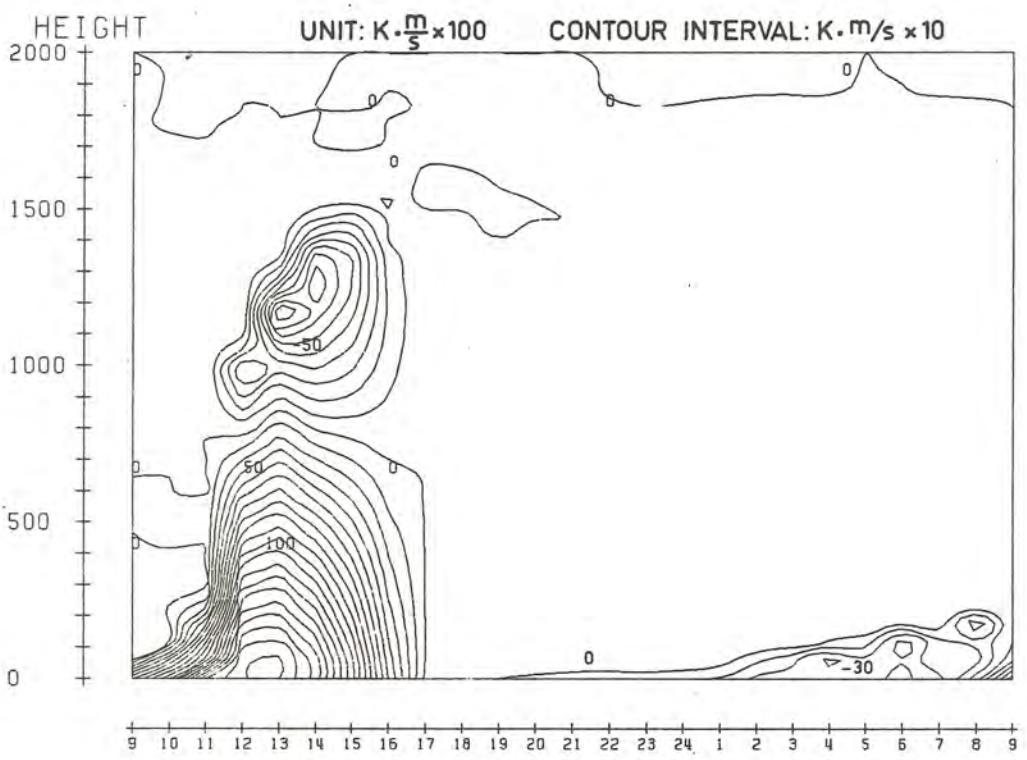

Fig. 24

Predicted time-height cross-section of kinematic heat flux by the full Gutman model. Day 33 and 34. Values multiplied by 100.

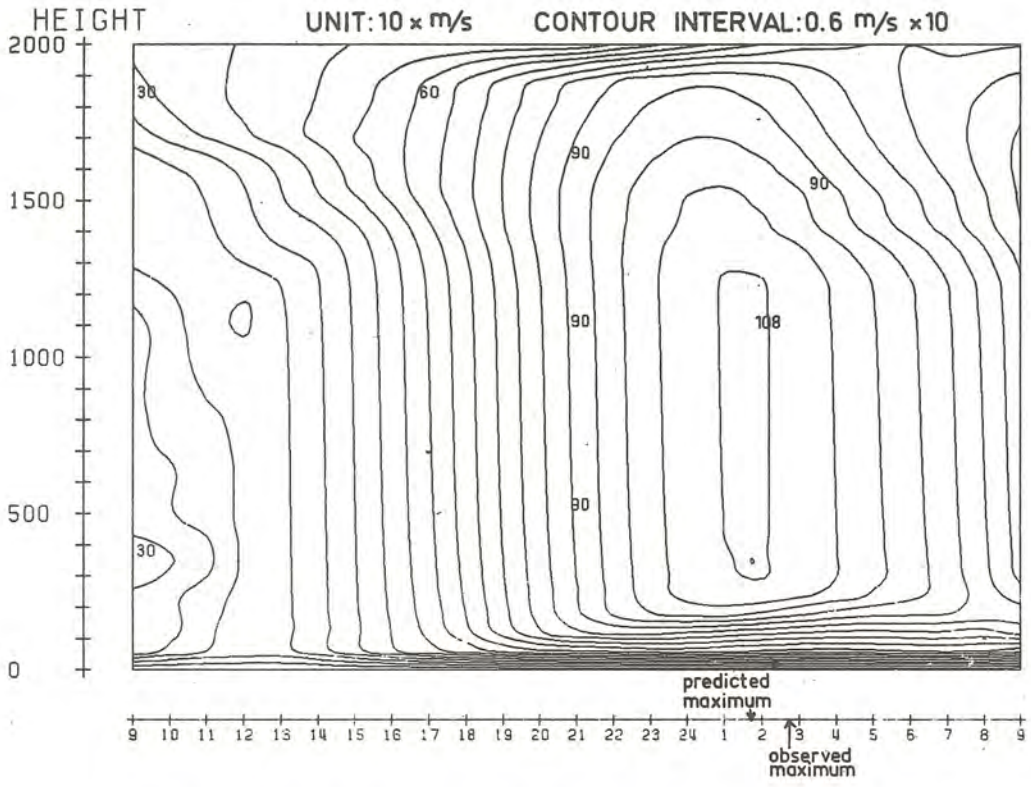

Fig. 25

Predicted time-height cross-section of wind speed by the Ekman-version of the model. No vertical shear in the geostrophic wind. Day 33 and 34 of the Wangara data.

a)

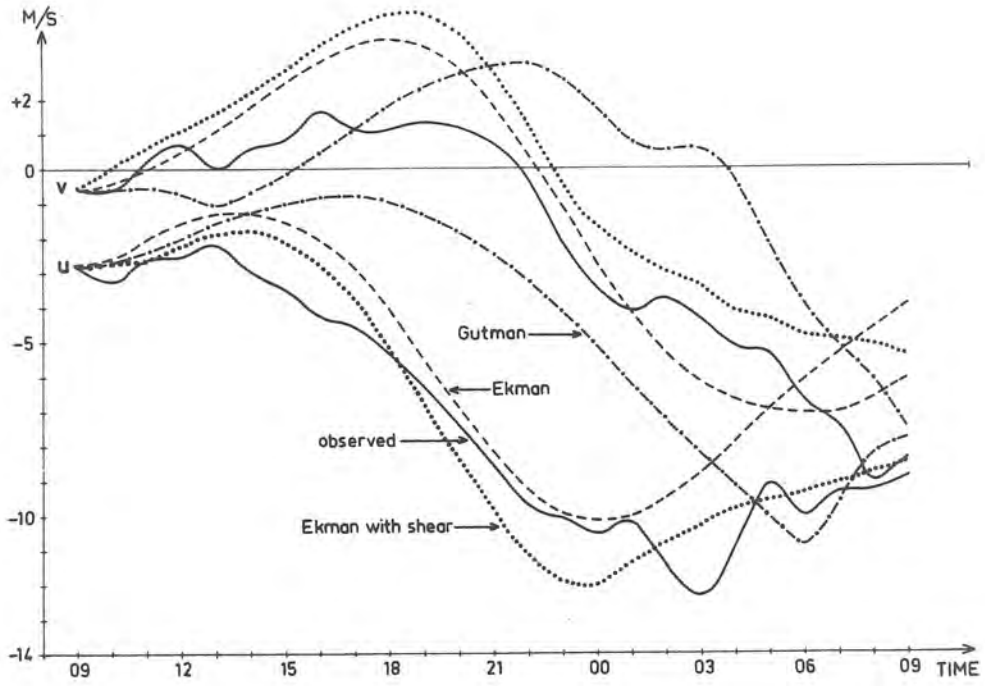

b)

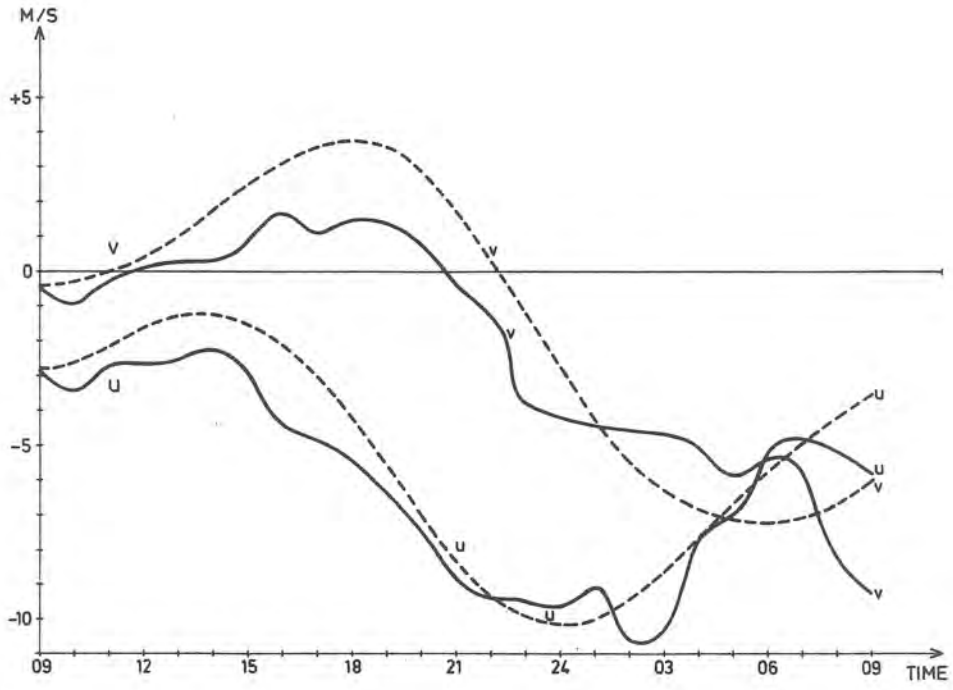

Fig. 26

a) Observed and predicted u- and v-components at 250 m. The dotted curves refer to an Ekman-version in which a geostrophic wind with constant shear between the surface and 2000 m has been used. Day 33 and 34 of the Wangara data.

b) Same as fig. 26a but at 450 m. Only observations and Ekman-version without shear are shown.

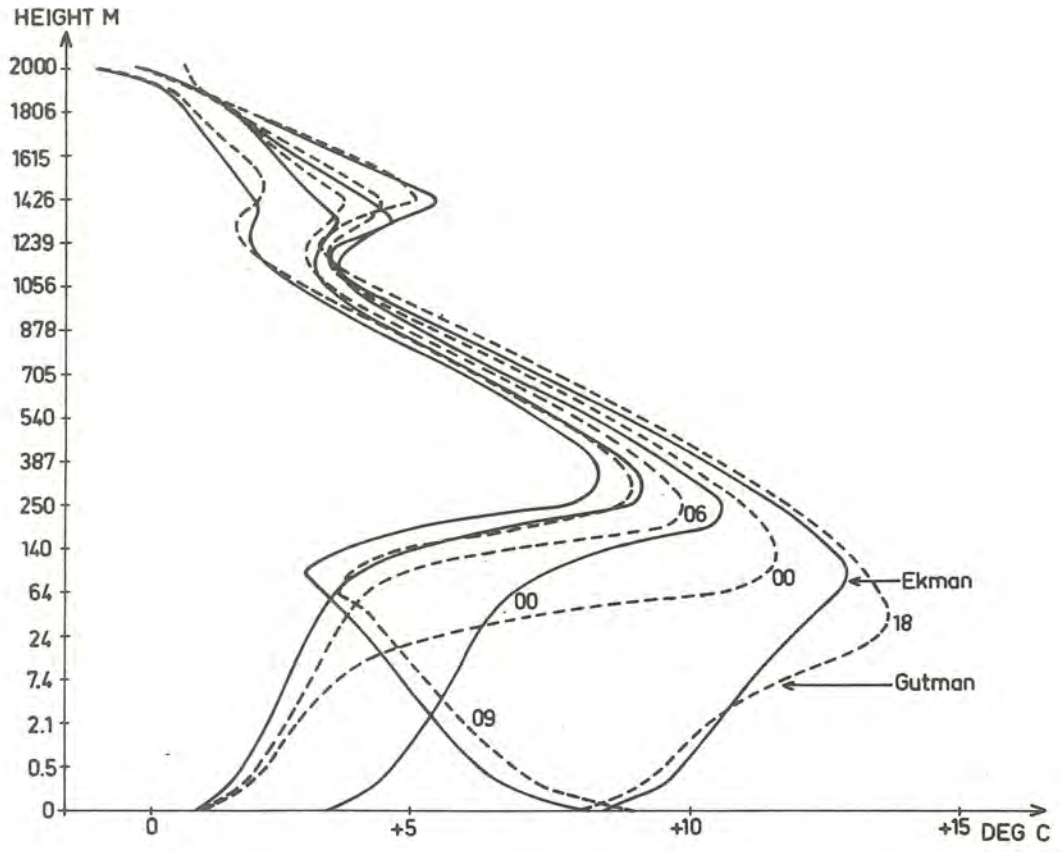

Fig. 27

Vertical profiles of temperature predicted by the Ekman-version of the model. For comparison also the Gutman-version predictions are shown. (Dashed curves). Day 33 and 34 of the Wangara data.

a)

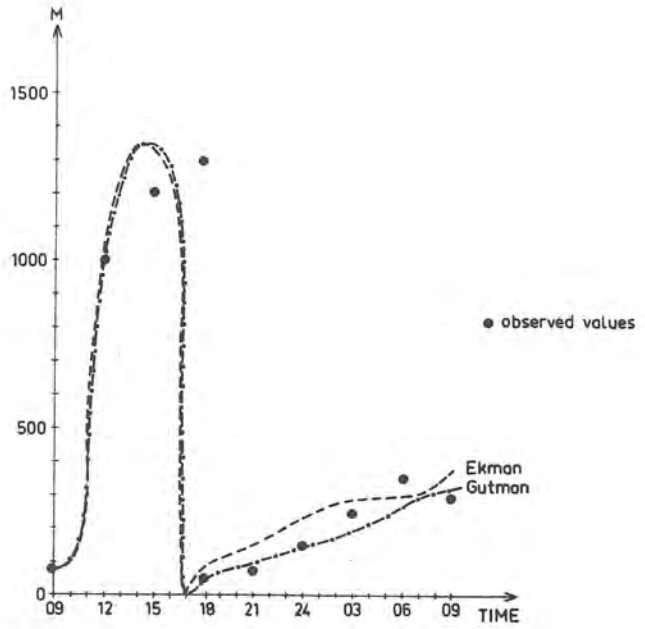

b)

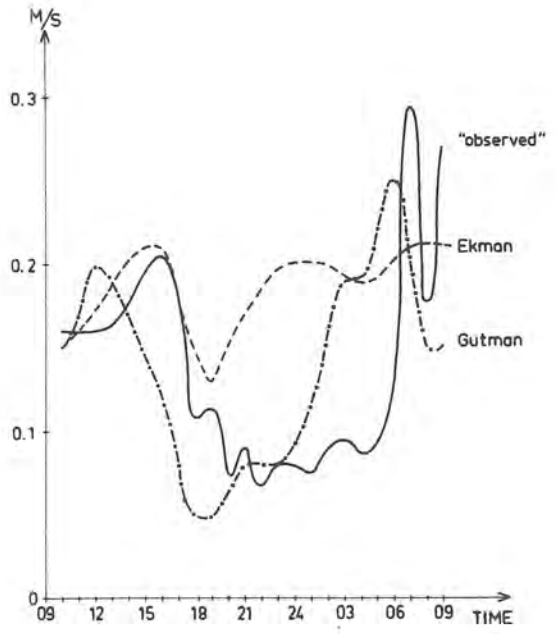

Fig. 28

a) Observed and predicted boundary layer height as a function of time. During the night the boundary layer height is picked out from the top of the surface inversion. Day 33 and 34.

b) "Observed" and predicted u_* as a function of time. "Observed" values are actually computed by means of Monin-Obukhov's similarity theory in connection with the surface temperature calculation. Day 33 and 34.

a)

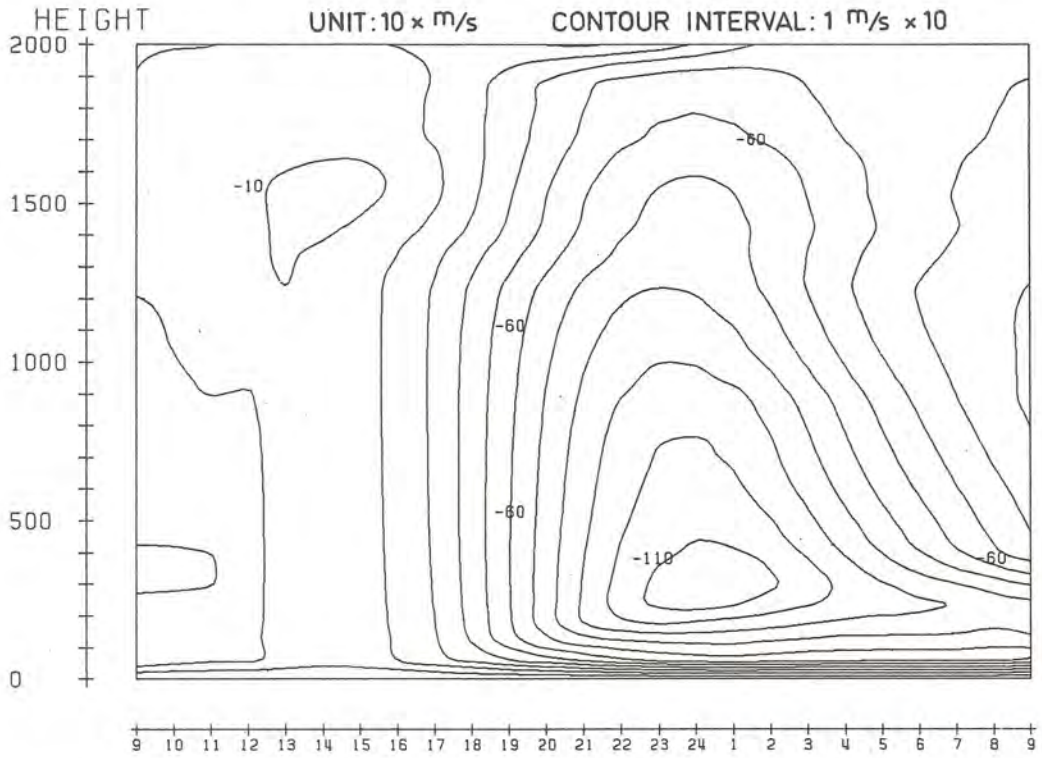

b)

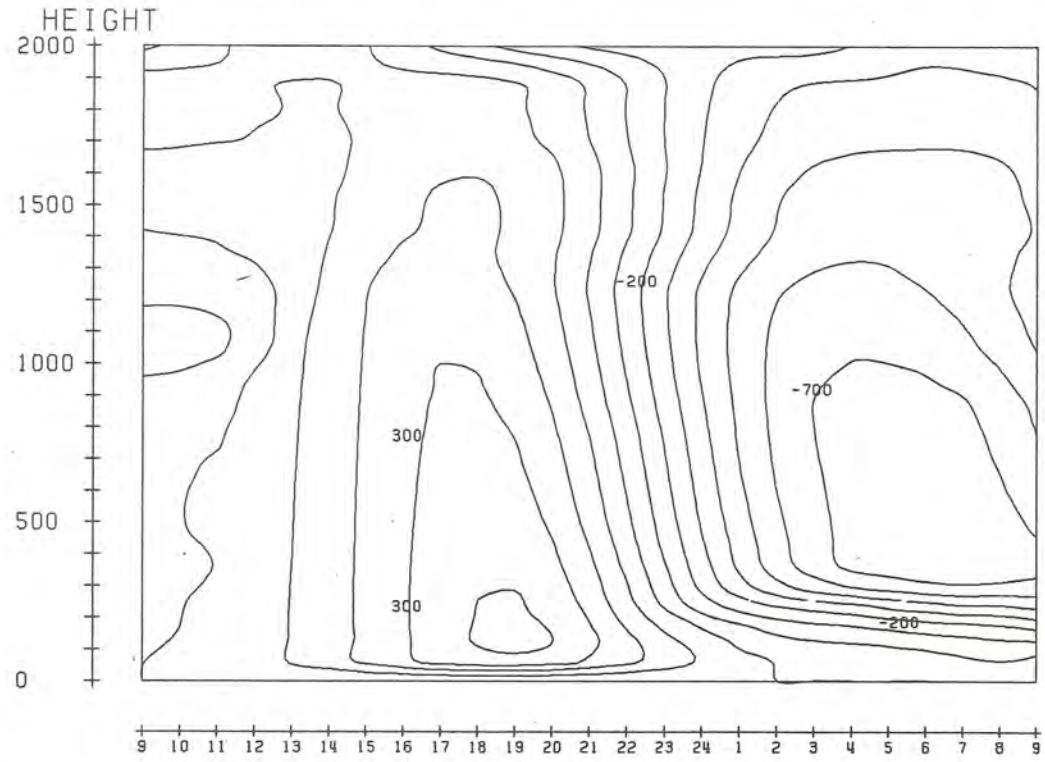

Fig. 29

a) Predicted time-height cross-section of the u-component of the wind by the Ekman-version of the model using the same geostrophic wind as Yamada & Mellor (1975). Day 33 and 34 of the Wangara data.

b) Same as fig. 29a but for the v-component.

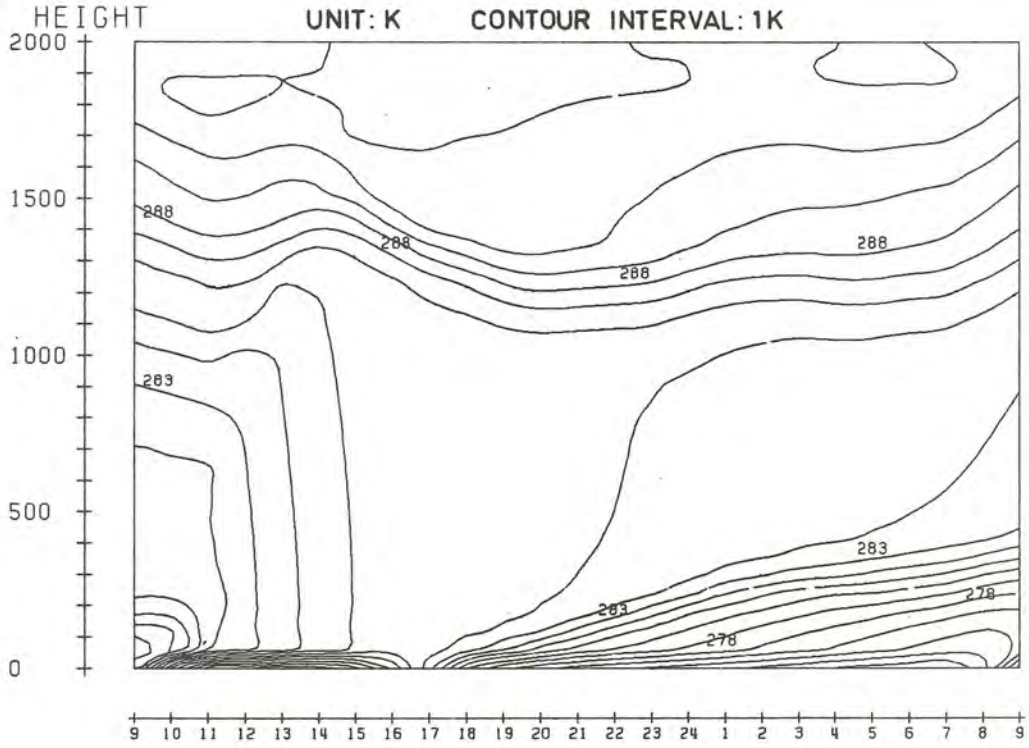

Fig. 30
Same as fig. 29 but for potential temperature.

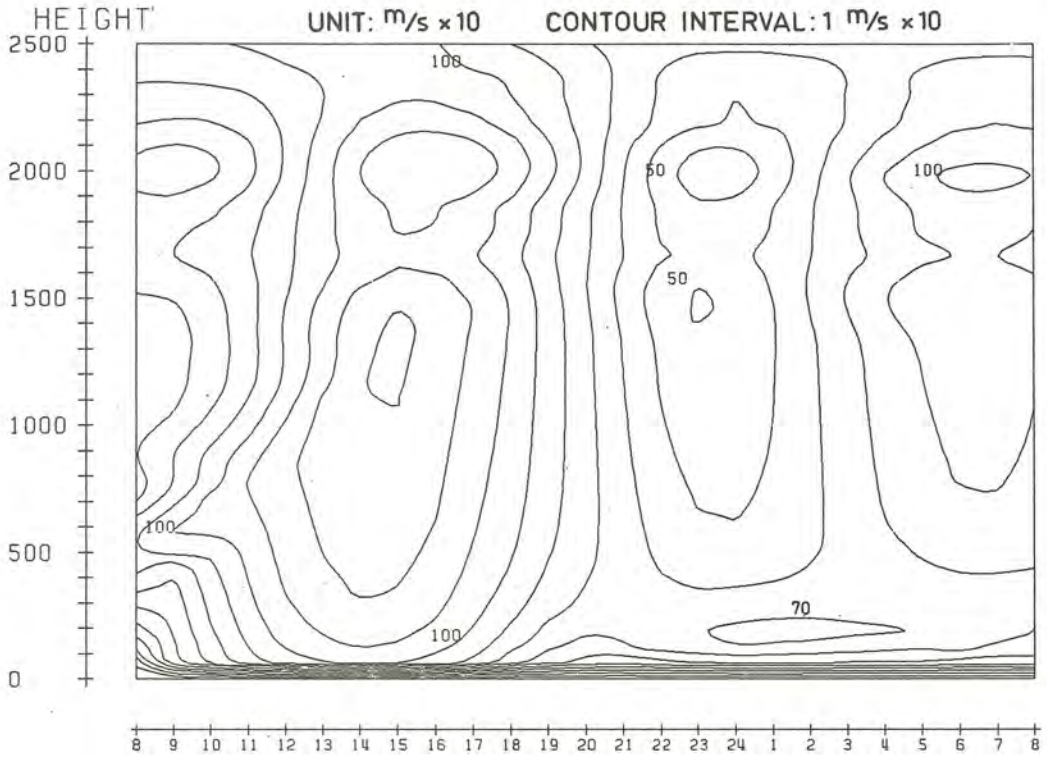

Fig. 31

Predicted time-height cross-section of wind speed using the Gutman-version. Data are from Hyrylä in Finland, 5 and 6 June 1972. Local time.

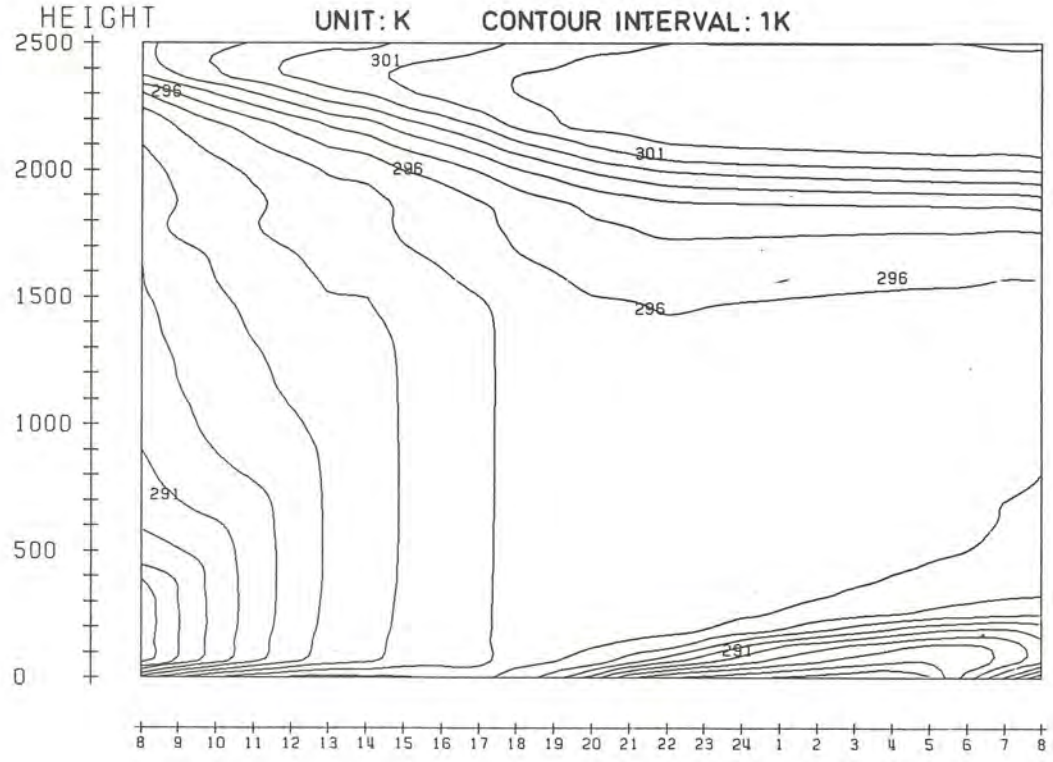

Fig. 32

Same as fig. 31 but for potential temperature.

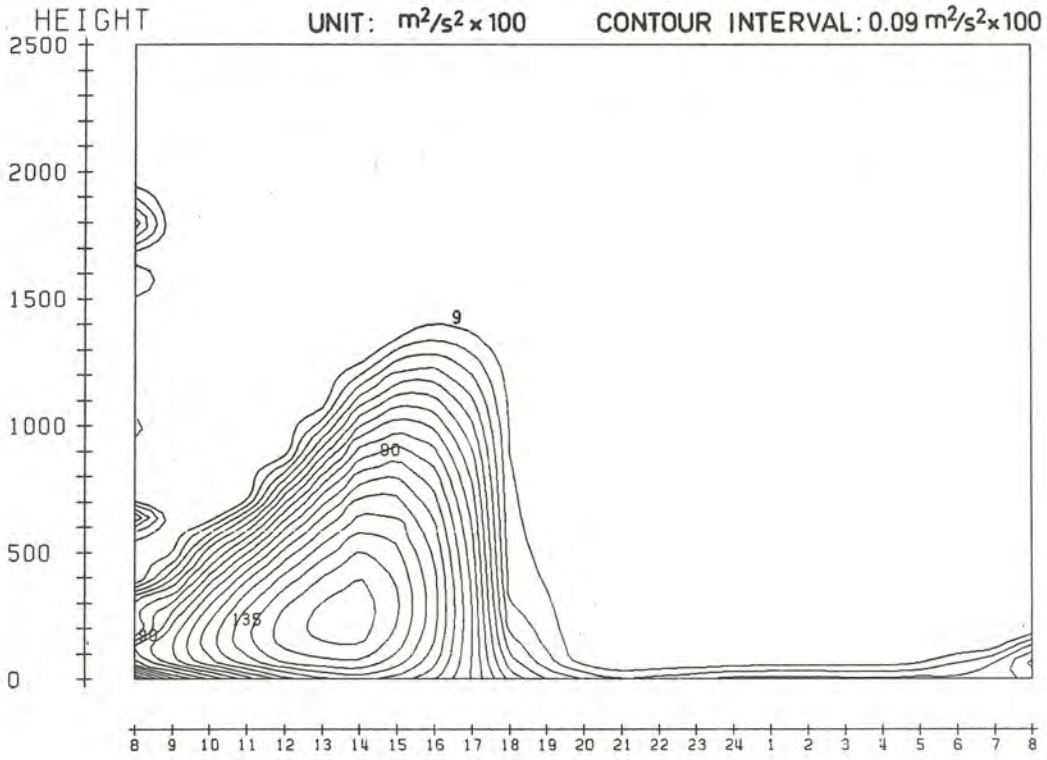

Fig. 33

Same as fig. 31 but for turbulent energy. Values multiplied by 100.

a)

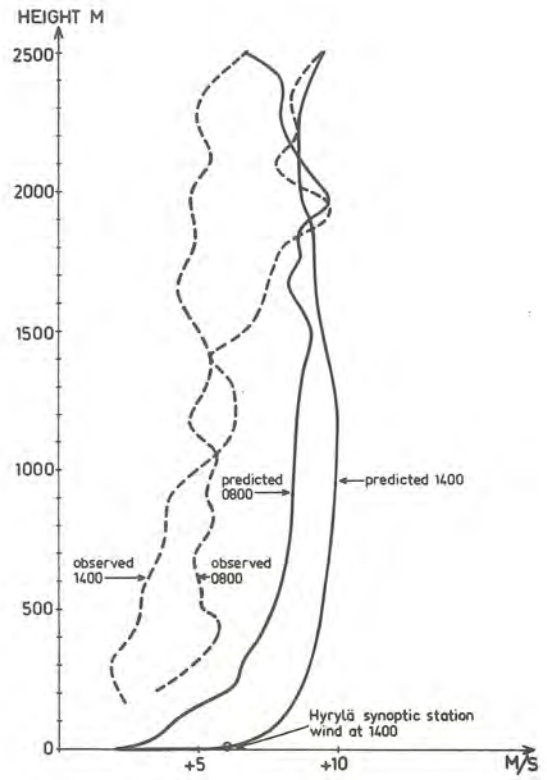

b)

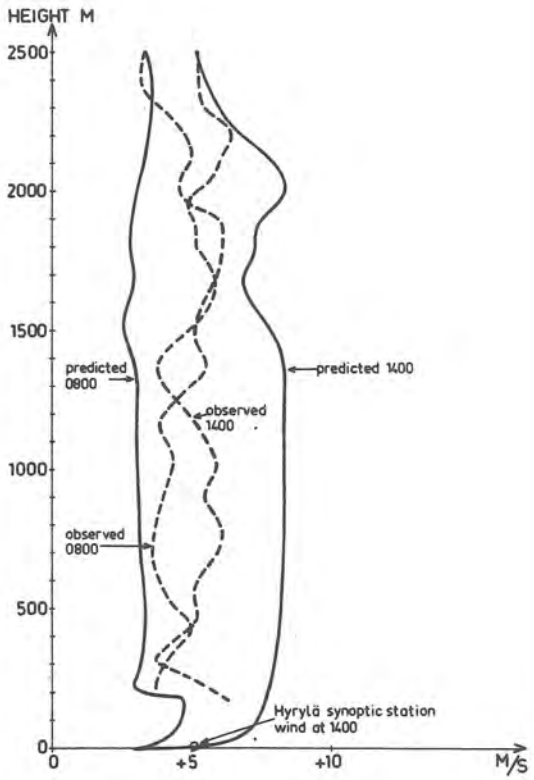

Fig. 34

a) Observed and predicted profiles of the u- (a) and v-component (b). Hyrylä data.

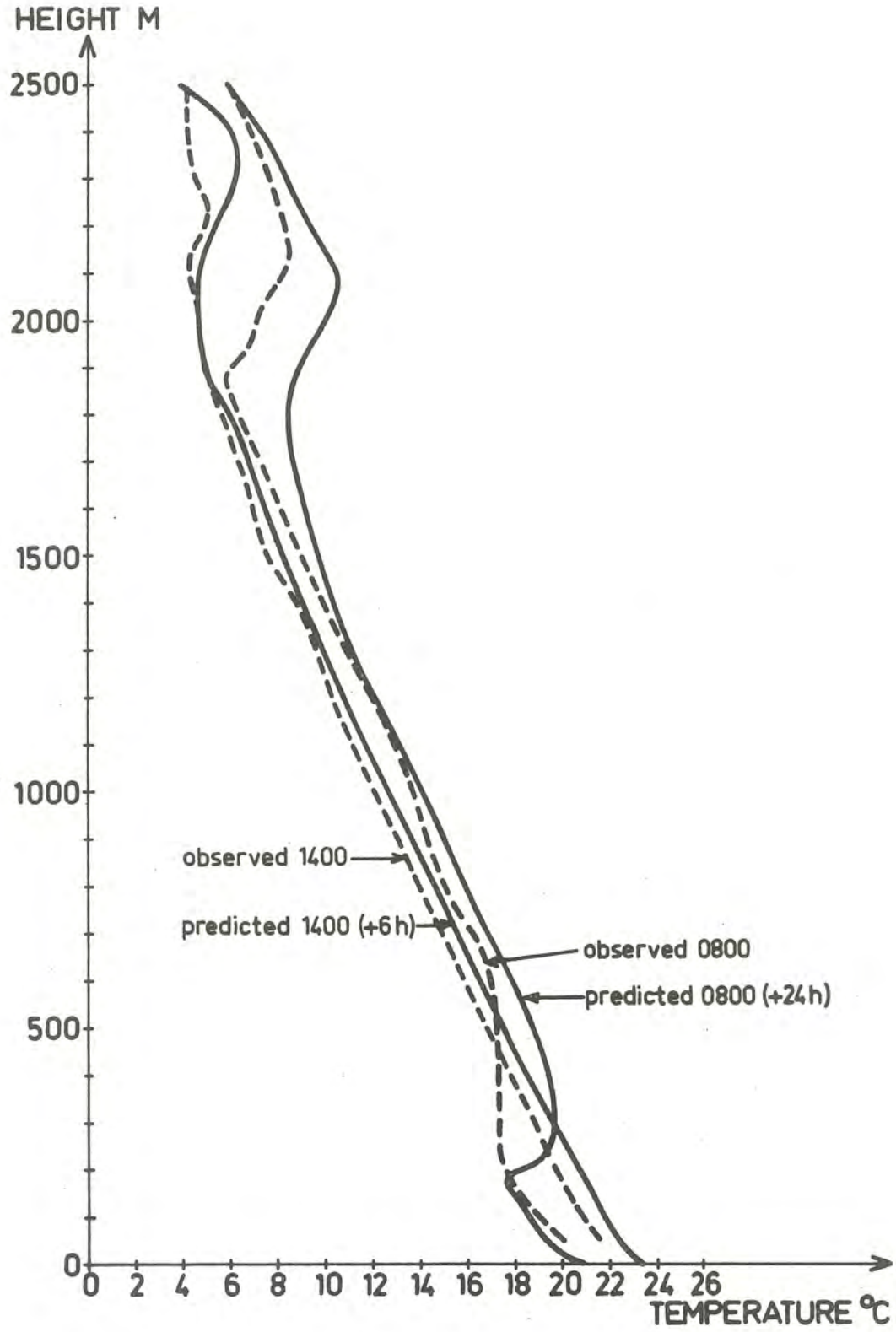

Fig. 35

Observed and predicted profiles of temperature. Hyrylä data.

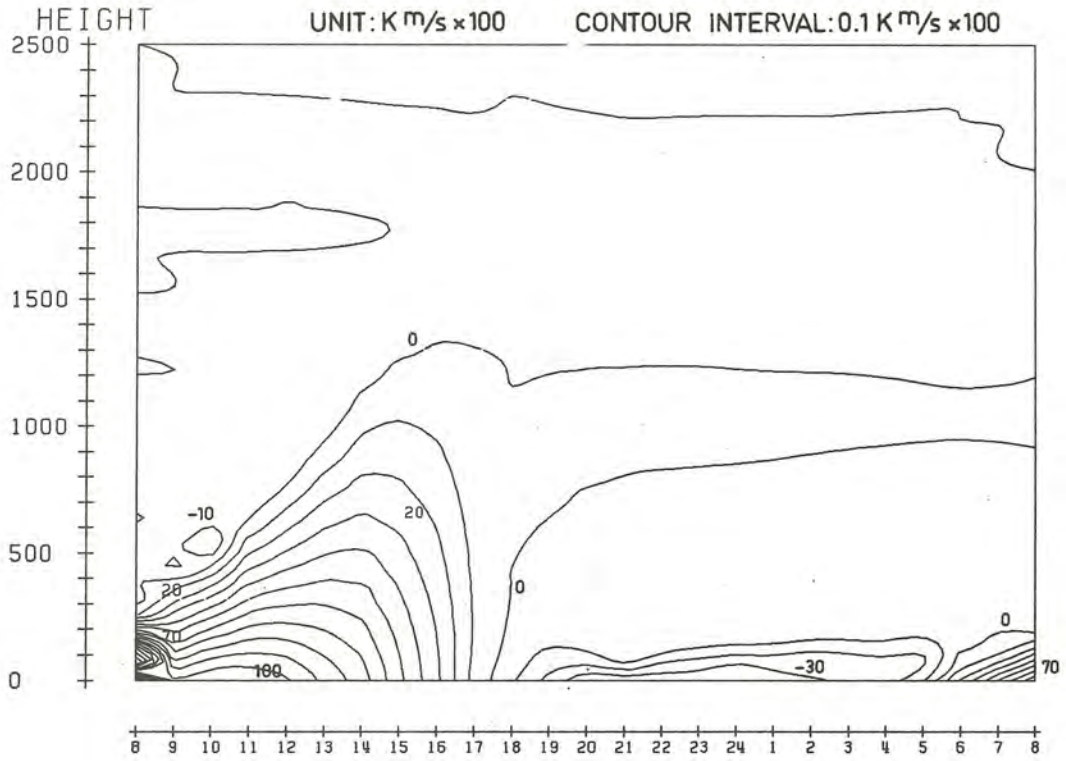

Fig. 36

Same as fig. 31 but for kinematic heat flux. Values multiplied by 100.

SMHI Rapporter, METEOROLOGI OCH KLIMATOLOGI

Nr 1 T h o m p s o n, T, U d i n, I och O m s t e d t, A: Sea surface temperatures in water surrounding Sweden (1974)

Nr 2 B o d i n, S: Development on an unsteady atmospheric boundary layer model (1974)

Nr 3 M o e n, L: A multilevel quasi-geostrophic model for short range weather predictions (1975)

Nr 4 H o l m s t r ö m, I: Optimization of atmospheric models (1976)

Nr 5 C o l l i n s, W G: A parameterization model for calculation of vertical fluxes of momentum due to terrain induced gravity waves (1976)

Nr 6 N y b e r g, A: On transport of sulphur over the North Atlantic (1976)

Nr 7 L u n d q v i s t, J-E och U d i n, I: Ice accretion on ships with special emphasis on Baltic conditions (1977)

Nr 8 E r i k s s o n, B: Den dagliga och årliga variationen av temperatur, fuktighet och vindhastighet vid några orter i Sverige (1977)

Nr 9 H o l m s t r ö m, I och S t o k e s, J: Statistical forecasting of sea level changes in the Baltic (1978)

Nr 10 O m s t e d t, A och S a h l b e r g, J: Some results from a joint Swedish-Finnish Sea Ice Experiment, March, 1977 (1978)

Nr 11 H a a g, T: Byggnadsindustrins väderberoende, seminarieuppsats i företagsekonomi, B-nivå (1978)

Nr 12 E r i k s s o n, B: Vegetationsperioden i Sverige beräknad från temperaturobservationer (1978)

Nr 13 A predictive numerical model of the Atmospheric Boundary Layer based on the Turbulent Energy Equation (1979)